



저작자표시-비영리-변경금지 2.0 대한민국

이용자는 아래의 조건을 따르는 경우에 한하여 자유롭게

- 이 저작물을 복제, 배포, 전송, 전시, 공연 및 방송할 수 있습니다.

다음과 같은 조건을 따라야 합니다:



저작자표시. 귀하는 원저작자를 표시하여야 합니다.



비영리. 귀하는 이 저작물을 영리 목적으로 이용할 수 없습니다.



변경금지. 귀하는 이 저작물을 개작, 변형 또는 가공할 수 없습니다.

- 귀하는, 이 저작물의 재이용이나 배포의 경우, 이 저작물에 적용된 이용허락조건을 명확하게 나타내어야 합니다.
- 저작권자로부터 별도의 허가를 받으면 이러한 조건들은 적용되지 않습니다.

저작권법에 따른 이용자의 권리는 위의 내용에 의하여 영향을 받지 않습니다.

이것은 [이용허락규약\(Legal Code\)](#)을 이해하기 쉽게 요약한 것입니다.

[Disclaimer](#)

공학박사 학위논문

**Application of Nematic Liquid
Crystal to Tunable Optofluidic
Birefringent Lens and Thermo-
sensitive Smart Film**

가변형 광유체 복굴절 렌즈와
열감응형 스마트 필름에 대한
네마틱 액정의 응용

2016년 2월

서울대학교 대학원
재료공학부
위 동 호

**Application of Nematic Liquid Crystal to
Tunable Optofluidic Birefringent Lens and
Thermo-sensitive Smart Film**

**가변형 광유체 복굴절 렌즈와
열감응형 스마트 필름에 대한
네마틱 액정의 응용**

지도 교수 윤 재 루

이 논문을 공학박사 학위논문으로 제출함
2015년 10월

서울대학교 대학원
재료공학부
위 동 호

위 동 호의 공학박사 학위논문을 인준함
2015년 12월

위 원 장 _____ (인)
부위원장 _____ (인)
위 원 _____ (인)
위 원 _____ (인)
위 원 _____ (인)

Application of Nematic Liquid Crystal to Tunable Optofluidic Birefringent Lens and Thermo- sensitive Smart Film

Advisor : Jae Ryoun Youn

by
Dongho Wee

2016

Department of Materials Science and Engineering
Graduate School
Seoul National University

Abstract

Applications of liquid crystals (LCs) have been focused on displays using orientation of them under an electric field, optical films such as retardation films and reflective polarizers using cholesteric LCs for liquid crystal displays (LCDs), and polymer-dispersed liquid crystal (PDLC) films. Among outstanding features of LCs, we note hydrodynamic properties in a microchannel and phase changes over transition temperature.

In Chapter II, a tunable birefringent lens using interfaces between an isotropic and nematic liquid crystal (NLC) stream in a microchannel, referred to as L^2 interfaces here, is demonstrated. When the NLC is subjected to an electric field and flows along the direction orthogonal to the field, the alignment of NLC molecules is determined according to a balance between the flow-induced orientation by a viscous torque and the field-induced orientation by the electric field. In this study, we propose electric and hydrodynamic conditions for NLC molecules to be aligned perpendicular to the direction of flow under a strong electric field using a two-dimensional finite element method based on Ericksen-Leslie (E-L) dynamic theory for NLC and a dimensionless analysis. In addition, we observe the orientation of NLC, the L^2 interfaces, and birefringent characteristics of the device at the proposed conditions experimentally. At this time, the flow rates of the NLC stream are controlled by a N_2 gas pressure pump instead of a conventional syringe pump to supply a sufficiently small amount of fluid in a stable manner, and the exact flow rate at each applied pressure is confirmed by measuring the inflow volume of the NLC. If the NLC molecules are uniformly aligned under the strong electric field, simplified E-L equations can be derived and coupled with Navier-Stokes equation for the isotropic fluid by the volume of fluid (VOF) method. Thus, we can describe the L^2 interfaces numerically, and calculate focal lengths using a ray-tracing.

In Chapter III, a thermal-induced PDLC film using the phase transition of LCs is investigated. A conventional PDLC film, which consists of a continuous polymer matrix and a number of LC droplets, is positioned between two transparent electrodes, and shows a transparency due to refractive index matching between the LC droplets and the polymer matrix when an electric field is applied to the film. On

the contrary, the LC droplets act as scattering particles in the absence of the electric field, so that the film turns to be opaque. Since the conventional PDLC film utilizes the field-induced orientation of LCs, it necessarily requires two transparent electrodes and a thin thickness of the film for low driving voltage. In general, ITO (Indium-tin oxide) coated glasses, which are fabricated by an electro-deposition process, are used as the transparent electrodes for the conventional PDLC film, but it costs high for a large-area production. In order to overcome the mentioned problems, we propose a novel PDLC thermo-sensitive smart film (TSF), which controls the optical transmittance through not the field-induced orientation of LCs but the thermal-induced phase transition of PDLCs. The TSF is fabricated by coating the PDLC layer on silver nanowire (AgNW) networks coated on a film-substrate. Also, the operation mechanism is investigated from measurements of thermo-optical properties and phase transition characteristics of the TSF. Based on these results, numerical analyses are carried out to predict thermal performances and temperature dependent transmittances using anomalous diffraction approach (ADA) as a scattering model. Furthermore, an effective operation method of the TSF is introduced by adopting a dynamic power control to reduce response time and consumed energy.

Keywords: polymer dispersed liquid crystal film, phase transition, transmittance, anomalous diffraction approach, Joule heating, silver nanowire, nematic liquid crystal, optofluidics, tunable birefringent lens, liquid lens, Ericksen-Leslie theory

Student Number: 2012-30164

Contents

Abstract	i
List of Figures	v
List of Tables	x
I. Overview	1
1.1. What is liquid crystal?	1
1.1.1. Nematic liquid crystals	4
1.1.2. Cholesteric liquid crystals	4
1.1.3. Smectic liquid crystals	8
1.2. Properties of nematic liquid crystals	10
1.2.1. Anisotropic permittivity	10
1.2.2. Hydrodynamics of nematic liquid crystals	14
1.2.3. Phase transition in heterogeneous mixture	18
1.3. Applications of liquid crystals	26
1.3.1. Liquid crystal display and its related films	26
1.3.2. Polymer dispersed liquid crystal	28
1.3.3. Microfluidic applications	30
1.4. Objectives of present work	31
1.5. References	34
II. Optofluidic Birefringent Lens	36
2.1. Introduction	36
2.2. Experimental	40
2.2.1. Design of optofluidic chip	40
2.2.2. Fabrication of optofluidic chip	40
2.2.3. Materials	44
2.2.4. Experimental set-up for observation	44
2.3. Numerical analyses	47
2.3.1. Orientation of directors in Poiseuille flow under strong electric field	47

2.3.2. Simulation of two-phase interfaces	51
2.4. Results and discussion	54
2.4.1. Dimensionless analysis for electric field dominant conditions	54
2.4.2. Validation of experimental conditions	60
2.4.3. NLC orientation and L^2 interface	64
2.4.4. Ray path	64
2.4.5. Comparison between numerical and experimental results	67
2.5. Summary	79
2.6. References	80
III. Thermo-sensitive Smart Film	82
3.1. Introduction	82
3.2. Experimental	84
3.2.1. Preparation of silver nanowire coated film	84
3.2.2. Fabrication of TSFs	84
3.2.3. Characterization and measurement	90
3.2.4. Effective electrical power	90
3.3. Numerical analyses	93
3.3.1. Temperature on film surface	93
3.3.2. Transmittance of TSF	94
3.4. Results and discussion	109
3.4.1. Performance of AgNW coated film	109
3.4.2. Thermo-optical behaviors of TSFs	109
3.4.3. Phase transition of TSFs	124
3.4.4. Dynamic power control	130
3.5. Summary	134
3.6. References	135
IV. Concluding Remarks	137
Korean Abstract	140

List of Figures

- Figure 1.1** A schematic representation of phase transition of thermotropic LC.
- Figure 1.2** Typical chemical structures of (a) calamitic and (b) discotic LC.
- Figure 1.3** A schematic representation of NLC.
- Figure 1.4** Chemical structures of (a) PAA, (b) MBBA, and (c) 5CB.
- Figure 1.5** Helical structure of CLC. The directors rotate around the helical axis counter-clockwise.
- Figure 1.6** Schematic illustrations of (a) smectic A, and (b) smectic C.
- Figure 1.7** (a) Index ellipsoid, and (b) unpolarized light propagation at ϕ relative to the optic axis in a positive uniaxial LC. The red arrow line represents the propagation of incident light.
- Figure 1.8** Three types of orientation modes in NLC: ‘Splay’, ‘Twist’, and ‘Bend’. K_1 , K_2 , and K_3 denote the elastic constant for each mode.
- Figure 1.9** Three possible configurations between the director orientations (\tilde{n}) and the flow directions. The flow direction is parallel to x -axis. The planes including the blue arrows mean the shear planes. (a) \tilde{n} is parallel to \tilde{v} (velocity field), (b) \tilde{n} is parallel to $\nabla\tilde{v}$, and (c) \tilde{n} is perpendicular to \tilde{v} and $\nabla\tilde{v}$.
- Figure 1.10** Theoretical phase diagram for a mixture of the NLC and the cross-linked polymer. This graph was redrawn from the result of Ref. 21.
- Figure 1.11** A schematic structure of LCD: (a) polarizers, (b) glass substrates, (c) spacers, (d) alignment layers, (e) color filter array, (f) LCs, (g) optical film, (h) light sources, and (i) light-guide plate.
- Figure 1.12** A schematic diagram for the PDLC film at (a) off-state and (b) on-state. Black arrows represent a mean direction of the directors in a droplet.
- Figure 2.1** Concept of the birefringent L^2 lens for (a) p-polarized and (b) s-polarized incident light. The red arrows represent the polarization direction of light.
- Figure 2.2** Index ellipsoids for (a) p-polarized and (b) s-polarized light. The red arrows represent the polarization direction of light.
- Figure 2.3** Configuration of the optofluidic chip used in this study.

Figure 2.4 Dimension of the optofluidic chip. The inclination angle of chamber wall (α) is 60° , the angle between the main channel and the sub-channel (β) is 40° , the channel width (w_c) is $200 \mu\text{m}$, the width of the expansion chamber (w_L) and the aperture (w_A) are $1,800 \mu\text{m}$ and $662.5 \mu\text{m}$ respectively, the height of expansion chamber (h_L) is $700 \mu\text{m}$, d_{LA} is $1,000 \mu\text{m}$, and d_{LR} is $500 \mu\text{m}$. The radius of curvature of the expansion chamber (R_c) is $300 \mu\text{m}$.

Figure 2.5 Schematic fabrication procedure of the optofluidic chip.

Figure 2.6 Experimental set-up for optical observation.

Figure 2.7 Geometry for the simulation of the flow-induced orientation of the director under a strong electric field.

Figure 2.8 Microscopic images of the microchannels filled with 5CB at static state. The microchannels were positioned between the crossed polarizers with a rotation angle of (a) 0° and (b) 45° . The white arrows represent the transmission axes of the crossed polarizers.

Figure 2.9 Orientation angles of the directors at $U =$ (a) 604, (b) 60.4, (c) 6.04, (d) 1.21, (e) 0.604, and (f) $0.121 \mu\text{m s}^{-1}$, respectively. The applied voltage was fixed at 5 V. The flow direction of NLC was from left to right.

Figure 2.10 Orientation angles of the directors at various average velocities and the fixed voltage ($V = 5 \text{ V}$) plotted in the range of (a) 10 - 90 degrees and (b) 85 - 90 degrees. The values of Ev are denoted at each corresponding line.

Figure 2.11 Orientation angles of the directors under $V =$ (a) 2.0, (b) 6.4, (c) 20.4, (d) 45.5, (e) 64.6, and (f) 143.9 V, respectively. The average velocity (U) was fixed at $100 \mu\text{m s}^{-1}$. The flow direction of NLC was from left to right.

Figure 2.12 Orientation angles of the directors at various applied voltages and constant velocity ($U = 100 \mu\text{m s}^{-1}$) plotted in the range of (a) 10 - 90 degrees and (b) 85 - 90 degrees. The values of Ev are denoted at each corresponding line.

Figure 2.13 Normalized refractive indices at various average velocities and the fixed voltage ($V = 5 \text{ V}$) plotted in the range of (a) 0.0 – 1.0 and (b) of 0.9980 – 1.0000.

Figure 2.14 Normalized refractive indices at various applied voltages and constant velocity ($U = 100 \mu\text{m s}^{-1}$) plotted in the range of (a) 0.0 – 1.0 and (b) 0.9980 – 1.0000.

Figure 2.15 (a) Average velocity and Ev , and (b) average velocity ratio of the main flow and sub-flow according to pressure for the main stream when the strong electric field (150 V, 50 kHz) was applied. The applied pressure for the sub-stream was fixed at 7 kPa.

Figure 2.16 Microscopic images of the expansion chambers (a) with and (b) without the electric field. The optofluidic chip was positioned between the crossed polarizers: (i) and (iv) with an angle of 0° and (ii) and (v) with an angle of 45° . (iii) and (iv) were unfiltered images. The white arrows represent the transmission axis of each polarizer. The denoted pressure values were applied for the main stream and the sub-stream (P_m and P_s , respectively).

Figure 2.17 Fluorescent images exhibiting ray paths in the ray-tracing chamber (a) without and (b) with the electric fields. The upper and lower rows indicate p- and s-mode which imply the incidence of the p-polarized and s-polarized light, respectively.

Figure 2.18 L^2 interfaces under the strong electric field observed by the light scattering.

Figure 2.19 Simulation results of the L^2 interfaces under the strong electric field at $f_c =$ (a) 0.5, (b) 0.6, and (c) 0.7.

Figure 2.20 Comparison of the L^2 interfaces between the simulation and the experimental results at $f_c =$ (a) 0.5, (b) 0.6, and (c) 0.7. Red lines represent the L^2 interfaces confirmed from the simulation results.

Figure 2.21 Illustration for the definition of the lens thickness (t_L) which indicates the thickness of the main stream at the edge of aperture.

Figure 2.22 Comparison between the experimental and the simulation results: (a) curvature and (b) lens thickness.

Figure 2.23 Focal length (F) calculated by using MATLAB at (a) $P_m = 11 \text{ kPa} / P_s = 7 \text{ kPa}$, (b) $P_m = 12 \text{ kPa} / P_s = 7 \text{ kPa}$, (c) $P_m = 13 \text{ kPa} / P_s = 7 \text{ kPa}$, and (d) $P_m = 14 \text{ kPa} / P_s = 7 \text{ kPa}$.

Figure 2.24 Comparison between the experimental and the simulation results for focal lengths in s-mode according to the applied pressure of the main stream (P_m).

Figure 3.1 Schematic procedure for the fabrication of the AgNW coated film.

Figure 3.2 The transparent AgNW coated film.

Figure 3.3 Chemical structure of 5PCH.

Figure 3.4 Fabrication procedures for the TSFs in the case of (a) N5P (NOA65/5PCH), and (b) P5P (PS/5PCH) as the PDLC layer.

Figure 3.5 Set-up for measurements of transmittances of the TSFs.

Figure 3.6 Schematic structure of the TSF for the heat transfer simulation.

Figure 3.7 Geometrical cross-section (σ_G) and sample cross-section (σ_s). This figure was redrawn from Ref. 29.

Figure 3.8 Reference frame for ADA.^[19] xz plane corresponds to the incidence plane. \tilde{S} is the unit vector along the direction of sample thickness, and \tilde{k} is the wave vector on the xz plane. $\tilde{E}_{opt}^{(O)}$ and $\tilde{E}_{opt}^{(E)}$ are the optical electric fields for the ordinary and the extraordinary beam, respectively. \tilde{N}_d represents the droplet director, which is inclined with respect to the external electric field at an angle of θ and with respect to the x -axis at an angle of φ .

Figure 3.9 Schematic illustrations of the director configurations in the oriented droplets. (a) bipolar, (b) radial, and (c) axial configuration.

Figure 3.10 Temperature dependent refractive indices of 5PCH. $(\Delta n)_o = 0.1719$, $T_M = 328$ K, $\beta = 0.1473$, $A = 1.6837$, and $B = 5.09 \times 10^{-4}$ K⁻¹ at the wavelength of 546 nm are used as the fitting parameters.^[34]

Figure 3.11 Temperature profiles obtained along the direction of thickness from the simulation results of the TSF with N5P operated at $P_{eff} = 0.258$ W.

Figure 3.12 SEM images of the surfaces of the AgNW coated film magnified with (a) 10,000 times and (b) 50,000 times.

Figure 3.13 Transmittance of the AgNW coated film measured using an UV-visible spectrometer.

Figure 3.14 Temperature evolutions of the AgNW coated film at various effective electrical powers (dots: experimental results, lines: simulation results).

Figure 3.15 Temperature contours of the AgNW coated film acquired from the simulation results at (a) $P_{eff} = 0.115$ W, (b) $P_{eff} = 0.258$ W, (c) $P_{eff} = 0.459$ W, and (d) $P_{eff} = 0.718$ W.

Figure 3.16 SEM image of the cross-section of PDLC layer in the TSF with N5P.

Figure 3.17 (a) Post-processed image to calculate the average diameter. (b) Droplet-size distribution.

Figure 3.18 Time dependent temperature profiles of the TSF with N5P at different effective electrical powers (dots: Experimental results, lines: simulation results).

Figure 3.19 Temperature contours of the TSF with N5P acquired from the simulation results at (a) $P_{eff} = 0.258$ W, (b) $P_{eff} = 0.323$ W, and (c) $P_{eff} = 0.387$ W.

Figure 3.20 Comparison of transmittance evolutions between experimental (black dots and lines) and simulation (red lines) results at effective electrical powers of (a) 0.258 W, (b) 0.323 W, and (c) 0.387 W.

Figure 3.21 Appearance of the TSF with N5P during the transmittance measurements at each time. The logos were located at 10 cm behind the TSF to identify opaque or clear state.

Figure 3.22 Transmittance profiles as a function of temperature at (a) 0.258 W, (b) 0.323 W, and (c) 0.387 W during heating and cooling.

Figure 3.23 DSC thermogram of the PDLC layer in the TSF with N5P.

Figure 3.24 (a) Time dependent temperature profile, and (b) transmittance evolution of the TSF with P5P during heating at $P_{eff} = 0.258$ W and cooling.

Figure 3.25 (a) Temperature profiles (black dots) of the TSF with N5P driven by the dynamic power control. The red line refers to the effective electrical powers. (b) Result of transmittance measurement in the dynamic power control test. The dashed lines correspond to the turning points of the applied effective electrical powers shown in (a).

Figure 3.26 Comparison of appearance of the TSF with N5P under the constant power control ($P_{eff} = 0.258$ W) and the dynamic power control ($P_{eff} = 0.387 \rightarrow 0.139$ W). d_{LA} is 1,000 μm , and d_{LR} is 500 μm . The radius of curvature of the expansion chamber (R_c) is 300 μm .

List of Tables

Table 2.1 Material properties of the main fluid (5CB) and the sub-fluid (the mixture of 2,2,2-trifluoroethanol and cyclohexanol).

Table 3.1 Material properties used for heat transfer simulation.

Table 3.2 Parameters for the calculation of the transmittances of the TSF with N5P.

Table 3.3 Resistances, effective voltages and powers of the AgNW coated film.

Table 3.4 Comparison of P_{eff} , Δt_h , Δt_c , and effective consumed energies (E_{eff}) of the TSF with N5P according to the operating method.

I. Overview

1.1. What is liquid crystal?

Generally, most matter exists in three states: solid, liquid, and gas. The phase of matter is decided by surrounding temperature or pressure. However, liquid crystals (LCs) exhibit properties of mesophase, which is a state of matter intermediate between liquid and solid.^[1] They flow like liquids, but possess some physical properties of solid.^[2] The LCs were discovered by the Austrian botanist Reinitzer in 1888.^[3] He observed two melting points during heating cholesteryl benzoate. At the first melting point of 145.5 °C, the cholesteryl benzoate became a cloudy liquid, and that turned into a clear liquid over 178.5 °C.^[1] This material is now known as a cholesteric liquid crystal or a chiral nematic liquid crystal. Although Reinitzer firstly found the LCs, the terminology of LC was established by German physicist Lehmann in 1900.^[1]

LC phases can be induced by changing concentration in a solvent or temperature. The former is called a lyotropic LC while the latter is referred to as a thermotropic LC. Recently, it has been reported that nano-sized particles such as the carbon nanotube (CNT), the graphene, and the nano-whisker dispersed in a solvent exhibit characteristics of the lyotropic liquid crystals over an adequate concentration.^[4-8] Fig. 1.1 schematically represents phase transitions of the thermotropic LCs according to temperature. They exist as solid crystals at a low temperature, but form LCs between melting and clearing temperature. Over clearing temperature, molecules of LCs are totally disordered due to increase of thermal energy, and changed to be isotropic liquids. LCs can be classified with calamitic (rod shaped molecules as shown in Fig. 1.2a) and discotic (disk-like molecules as shown in Fig. 1.2b) LCs according to molecular structures of LCs. Also, LCs can be classified into three types (nematic, cholesteric, and smectic LCs) according to their ordered structures. Each of them is explained as follows.

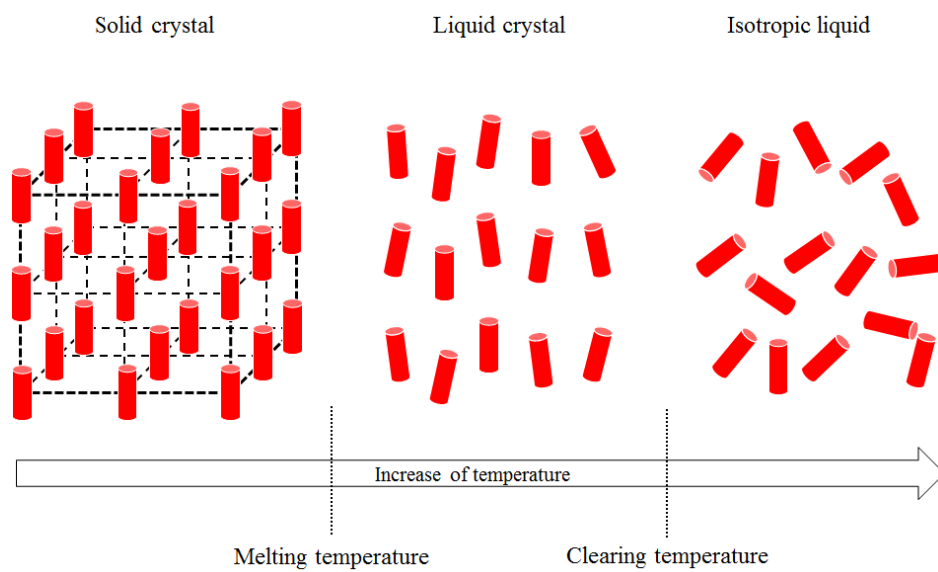


Figure 1.1 A schematic representation of phase transition of thermotropic LC.^[1]

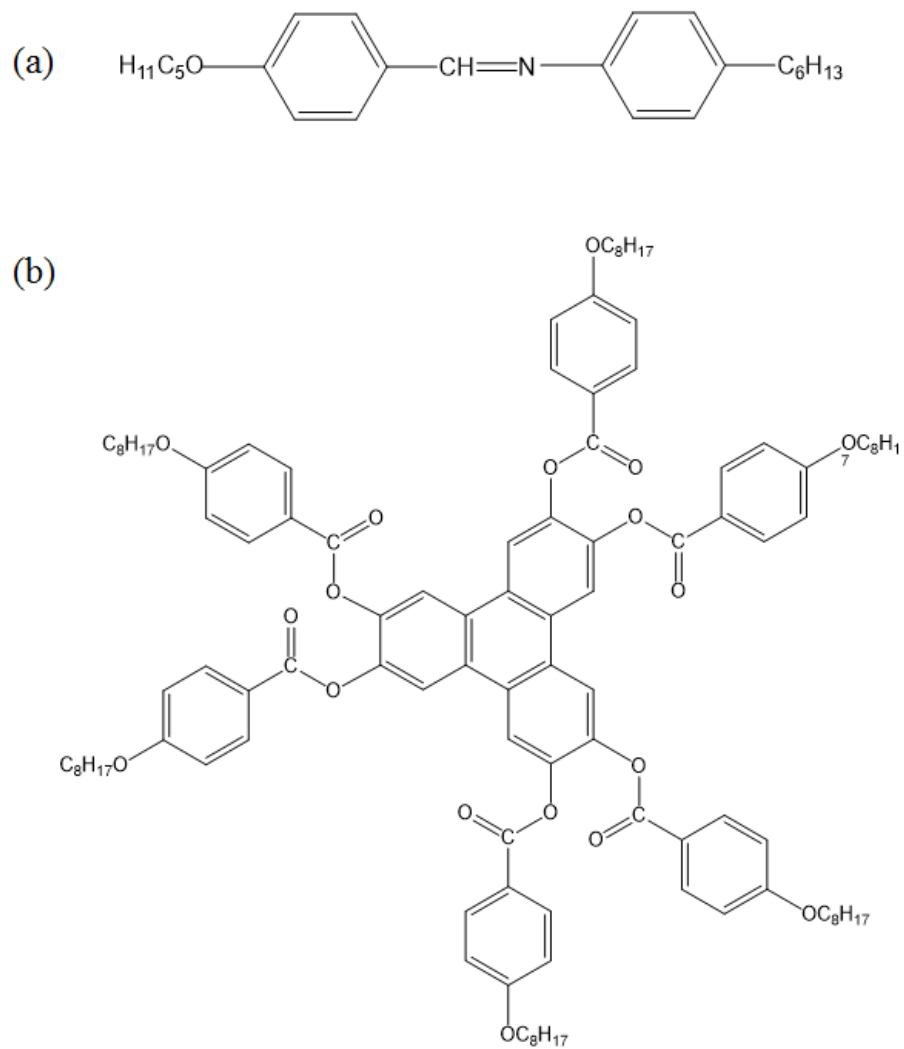


Figure 1.2 Typical chemical structures of (a) calamitic and (b) discotic LC.^[16]

1.1.1. Nematic liquid crystals

In the nematic LCs (NLCs), molecules are self-organized to have long-range directional order along their long axes roughly parallel, but no positional order as shown in Fig. 1.3.^[9] This preferred direction is referred to as the anisotropic axis or the director (\tilde{n}) to describe the local direction of average molecular orientation in LCs.^[1] The nematic phase has a rotational symmetry around the anisotropic axis, and no polarity on a large scale although each molecule has a polar functional group.^[1] This means that \tilde{n} and $-\tilde{n}$ are equivalent, that is, the sign of \tilde{n} has no physical meaning.^[10]

p-azoxyanisole (PAA), the first NLC, was synthesized by Gattermann and Ritschke in 1890.^[11] 4-methoxybenzylidene-4'-butylaniline (MBBA) was the first stable NLC at room temperature, which was synthesized by Kelker and Scheurle in 1969.^[12] 4-cyano-4'-pentyl-1,1'-biphenyl (5CB) is the representative NLC designed for the LCDs. 5CB was synthesized by Gray *et al.* in 1973.^[13] The chemical structures for PAA, MBBA, and 5CB are given in Fig. 1.4.

1.1.2. Cholesteric liquid crystals

The cholesteric LCs (CLCs) are mixtures of the NLC and a chiral dopant which induces a helical configuration of LC molecules as shown in Fig. 1.5. The directors rotate around the helical axis clockwise or counter-clockwise, so that this helical structure arises from the chiral properties. Therefore, the cholesteric LCs are sometimes called the chiral NLCs. The CLCs are characterized by the pitch (P in Fig. 1.5) representing the distance from one layer to other layer where the director makes a one rotation (2π radians). The periodicity is a half of P because \tilde{n} and $-\tilde{n}$ are indistinguishable as the above-mentioned.^[1] The CLCs show a selective reflection for an incident light. They reflect a circularly polarized light with the same rotation direction of the helical structure. When an unpolarized light is incident into a medium of the CLC, it is decomposed into clockwise and counter-clockwise circularly polarized light. One component is reflected and the other

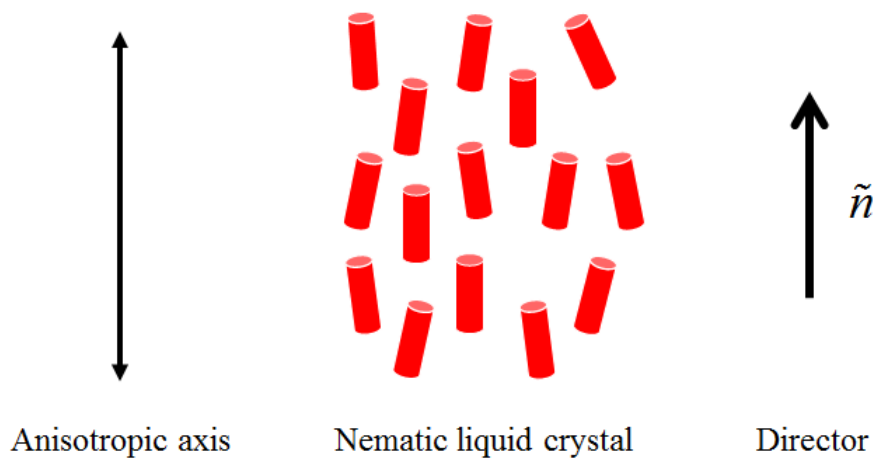


Figure 1.3 A schematic representation of NLC.^[1]

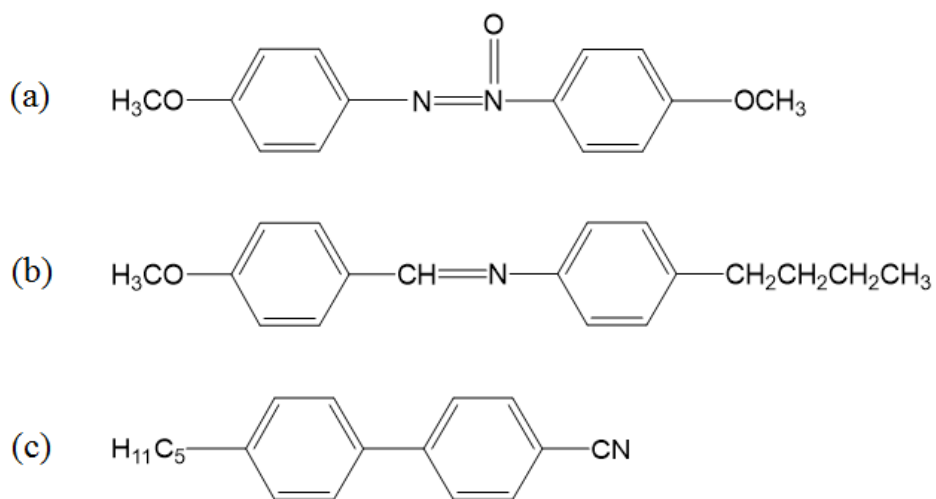


Figure 1.4 Chemical structures of (a) PAA, (b) MBBA, and (c) 5CB.

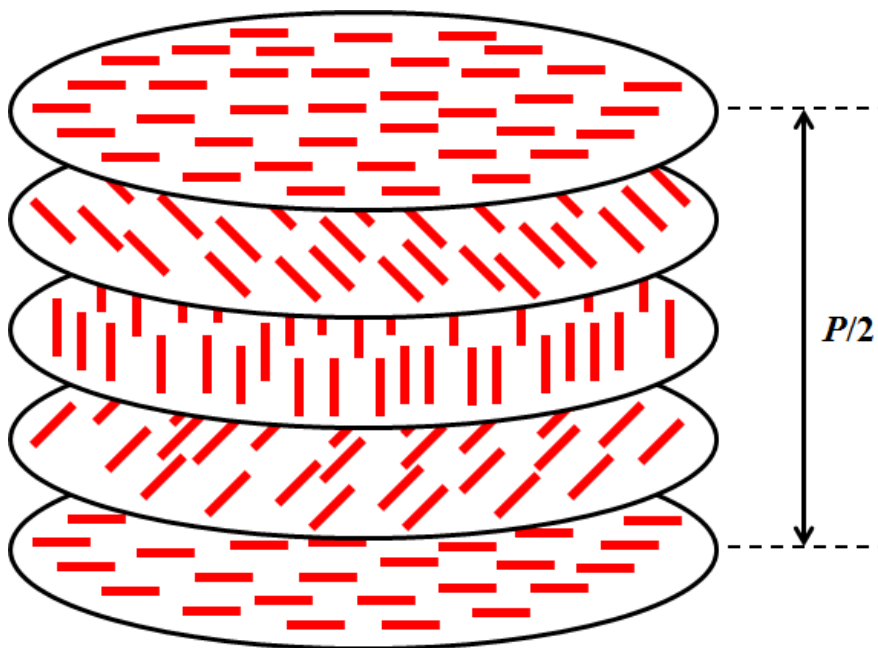


Figure 1.5 Helical structure of CLC. The directors rotate around the helical axis counter-clockwise.^[14]

component is transmitted. Using these properties, the CLCs can be used for a reflective polarizer.^[15]

1.1.3. Smectic liquid crystals

The word of smectic means soap in Greek. The smectic LCs have the positional order as well as the directional order as shown in Fig. 1.6. All smectic LCs are layered structures having a well-defined interlayer distance.^[1] In general, the smectic phases can be observed at below temperature at which the same material exhibits the nematic phases. There are two representative types of smectic LCs, smectic A, and smectic C. In the smectic A phase, the directors are aligned perpendicular to the layers as shown in Fig. 1.6a. On the other hand, the directors in the smectic C phase are inclined with an angle θ (referred to as smectic cone angle or smectic C tilt angle) to the layer normal as shown in Fig. 1.6b. Generally, θ is dependent on temperature.

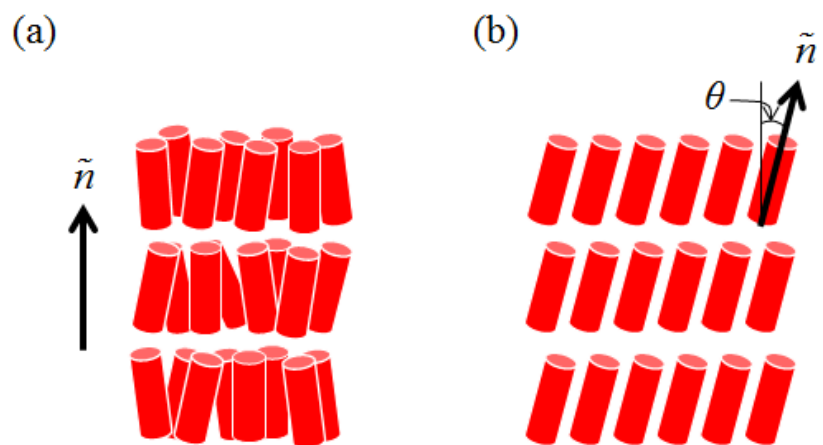


Figure 1.6 Schematic illustrations of (a) smectic A, and (b) smectic C.

1.2. Properties of nematic liquid crystals

The ordered structures of NLCs induce anisotropic physical properties such as elastic modulus, dielectric constant, magnetic susceptibility, and refractive index, so that they give different results depending on the direction along which they are measured.^[16] In addition, NLCs exhibit different viscosities due to their rod-like shape according to flow and orientation direction. Moreover, they show unique phase transition behavior in a mixture with polymer. These inherent properties of NLCs originate from molecular structures and interactions of NLCs. In this chapter, the above-mentioned properties of NLCs will be considered.

1.2.1. Anisotropic permittivity

Because light is an electromagnetic wave, we consider a response to an electric field during a propagation of light in a NLC medium. When an electric field (\tilde{E}) is applied to the medium, a charge separation occurs on LC molecules, and induces weak dipole moments. These dipole moments are the polarization (\tilde{P}) of the medium. The relation between \tilde{P} and \tilde{E} is given by

$$\tilde{P} = \varepsilon_o \tilde{\chi}_e \tilde{E}, \quad (1-1)$$

$$\tilde{\chi}_e = \begin{bmatrix} \chi_{e,xx} & 0 & 0 \\ 0 & \chi_{e,yy} & 0 \\ 0 & 0 & \chi_{e,zz} \end{bmatrix}, \quad (1-2)$$

where ε_o is the permittivity of free space, and $\tilde{\chi}_e$ is the electric susceptibility tensor. The electric displacement \tilde{D} induced by \tilde{P} and \tilde{E} is defined by

$$\tilde{D} = \varepsilon_o \tilde{E} + \tilde{P} = \varepsilon_o \tilde{\varepsilon} \tilde{E}, \quad \tilde{\varepsilon} = \tilde{I} + \tilde{\chi}_e, \quad (1-3)$$

where \tilde{I} is the identity tensor, and $\tilde{\varepsilon}$ is the relative permittivity tensor which is

written as

$$\tilde{\varepsilon} = \begin{bmatrix} \varepsilon_{xx} & 0 & 0 \\ 0 & \varepsilon_{yy} & 0 \\ 0 & 0 & \varepsilon_{zz} \end{bmatrix} = \begin{bmatrix} 1 + \chi_{e,xx} & 0 & 0 \\ 0 & 1 + \chi_{e,yy} & 0 \\ 0 & 0 & 1 + \chi_{e,zz} \end{bmatrix}, \quad (1-4)$$

where ε_{xx} , ε_{yy} , and ε_{zz} are the dielectric permittivities (or dielectric constants) for each direction. Therefore, the refractive index tensor (\tilde{n}) can be defined as

$$\begin{aligned} \tilde{n} = \sqrt{\tilde{\varepsilon}} &= \begin{bmatrix} \sqrt{\varepsilon_{xx}} & 0 & 0 \\ 0 & \sqrt{\varepsilon_{yy}} & 0 \\ 0 & 0 & \sqrt{\varepsilon_{zz}} \end{bmatrix} = \begin{bmatrix} \sqrt{1 + \chi_{e,xx}} & 0 & 0 \\ 0 & \sqrt{1 + \chi_{e,yy}} & 0 \\ 0 & 0 & \sqrt{1 + \chi_{e,zz}} \end{bmatrix} \\ &= \begin{bmatrix} n_{xx} & 0 & 0 \\ 0 & n_{yy} & 0 \\ 0 & 0 & n_{zz} \end{bmatrix}. \end{aligned} \quad (1-5)$$

The LCs reveal anisotropic dielectric permittivities due to their molecular structures and ordering. If $n_{xx} = n_{yy} \neq n_{zz}$, this material is called a uniaxial LC. The uniaxial LC can be classified into a positive ($n_{zz} > n_{xx} = n_{yy}$) and a negative ($n_{zz} < n_{xx} = n_{yy}$) uniaxial LC. If n_{xx} , n_{yy} , and n_{zz} are different values for each other, this is called a biaxial LC. Most of the rod-shaped NLCs exhibit the positive uniaxial characteristics. In the positive uniaxial LCs, n_{xx} and n_{yy} are denoted as n_{\perp} , and n_{zz} is written as n_{\parallel} . The relative magnitude of refractive indices in the positive uniaxial crystal is spatially described as an ellipsoidal shape as shown in Fig. 1.7a, which is called the index ellipsoid or the indicatrix. In the index ellipsoid of the positive uniaxial LC, the long axis of ellipsoid corresponds to the magnitude of n_{\parallel} , which is also accordant to the optic axis, and the short axis corresponds to the magnitude of n_{\perp} . When an unpolarized light is propagated in the positive uniaxial medium with the angle ϕ relative to the optic axis as shown in Fig. 1.7b, the light is decomposed into two rays. One ray is propagated with n_e (referred to as the extraordinary refractive index), which is decided from the long axis of the ellipse on the intersection plane between the plane orthogonal to the propagated light and

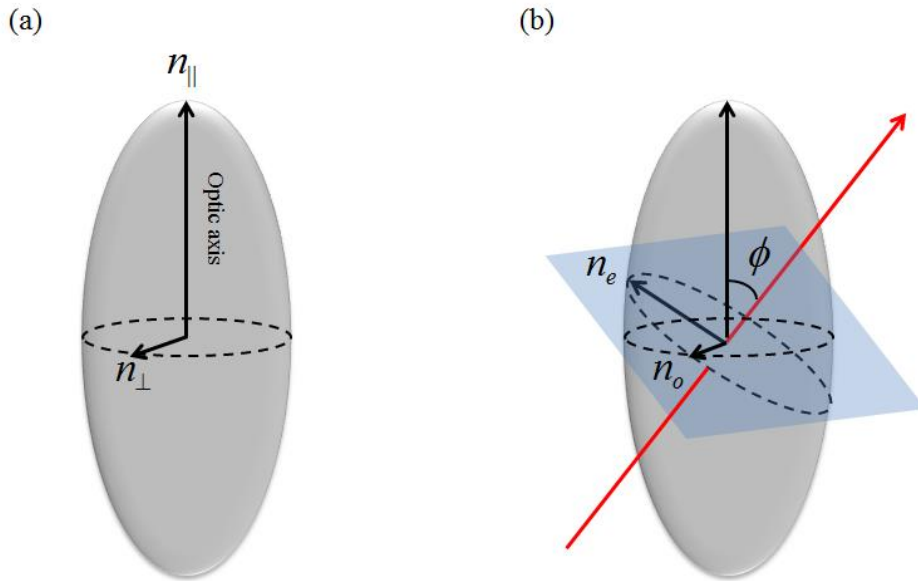


Figure 1.7 (a) Index ellipsoid, and (b) unpolarized light propagation at ϕ relative to the optic axis in a positive uniaxial LC.^[10] The red arrow line represents the propagation of incident light.

the ellipsoid. The other ray is propagated with n_o (referred to as the ordinary refractive index), which is equal to the short axis of the ellipse on the intersection plane. n_o is equivalent to n_{\perp} in the positive uniaxial LC. n_e and n_o can be calculated as the following equations.^[10]

$$n_e = \frac{n_{\perp}n_{\parallel}}{\sqrt{n_{\parallel}^2 \cos^2 \phi + n_{\perp}^2 \sin^2 \phi}}, \quad n_o = n_{\perp} \quad (1-6)$$

As a result, the ordinary and the extraordinary rays induce a phase difference (δ) during the propagation into the medium with a thickness d . δ is calculated by

$$\delta = \frac{2\pi}{\lambda} \Delta n d, \quad (1-7)$$

where λ is the wavelength of light. Δn is called the optical birefringence which is equal to $n_e - n_o$.

The anisotropic permittivity of NLCs induces the field-induced orientation as well as the birefringence. The directors keep their initial orientations at static state according to a surface anchoring condition and an elastic energy of the directors. If a strong field such as an electric or a magnetic field is applied to the directors, they are rearranged. For the application of magnetic field, most LCs are oriented parallel to the magnetic field. The rearrangement by an external field is called Fredericksz transition. In the positive uniaxial NLCs, ε_{xx} and ε_{yy} can be denoted as ε_{\perp} , and ε_{zz} can be written as ε_{\parallel} in accordance with n_{\perp} and n_{\parallel} . At this time, the dielectric anisotropy (ε_a) is defined as $\varepsilon_{\parallel} - \varepsilon_{\perp}$, and is a positive value in the positive uniaxial LCs. In this case, the directors are aligned parallel to the electric field. On the contrary, the directors of the negative uniaxial NLCs are aligned perpendicular to the electric field. The Fredericksz transitions only occur when the applied field is over a critical value, which is called the Fredericksz threshold or the critical field strength. When the electric field is applied, the Fredericksz threshold (E_c) is calculated by the following equations.^[1]

$$E_c = \frac{\pi}{d} \sqrt{\frac{K}{\varepsilon_o \varepsilon_a}}, \quad (1-8)$$

where d is the total thickness of the LC medium along the electric field, and K is the elastic constant. There are three types of orientation modes in the NLCs as shown in Fig. 1.8. K in Eq. (1-8) is selected as K_1 , K_2 , or K_3 according to the initial orientation.

1.2.2. Hydrodynamics of nematic liquid crystals

A dynamic theory for NLCs was developed by Ericksen in 1961 using balance laws based on continuum mechanics, and completed in 1968 by Leslie who derived suitable constitutive equations.^[1,17,18] Accordingly, the dynamic theory for NLCs is often referred to as Ericksen-Leslie (E-L) dynamic theory. In the E-L dynamic theory, it is assumed that the NLC is incompressible and isothermal. The E-L dynamic equations comprise two constraints and two governing equations as follows.

$$n_i n_i = 1, \quad i = 1, 2, 3, \quad (1-9)$$

$$u_{i,i} = 0, \quad (1-10)$$

$$\rho \dot{u}_i = \rho F_i - (p + w_F)_{,i} + \tilde{g}_j n_{j,i} + G_j n_{j,i} + \tilde{t}_{ij,j}, \quad (1-11)$$

$$\left(\frac{\partial w_F}{\partial n_{i,j}} \right)_{,j} - \frac{\partial w_F}{\partial n_i} + \tilde{g}_i + G_i = \lambda n_i. \quad (1-12)$$

Eq. (1-9) is a constraint for magnitude of the director (n_i), and Eq. (1-10) represents the continuity equation for the incompressible fluid. Eq. (1-11) and (1-12) are the linear momentum equation and the angular momentum equation, respectively. u_i means the velocity field, ρ is the density of NLC, F_i is the external body force per unit mass, p is the pressure, and w_F is the elastic free energy density as given by

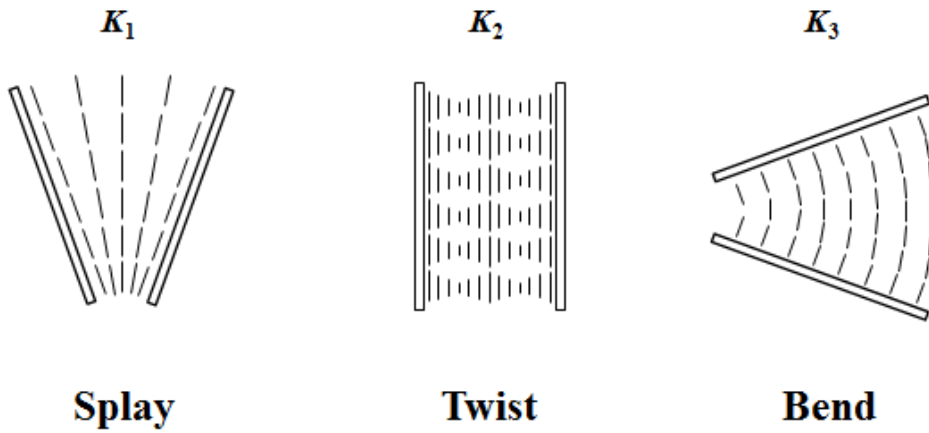


Figure 1.8 Three types of orientation modes in NLC: ‘Splay’, ‘Twist’, and ‘Bend’. K_1 , K_2 , and K_3 denote the elastic constant for each mode.^[1]

$$w_F = \frac{1}{2} K_1 (\nabla \cdot \tilde{n})^2 + \frac{1}{2} K_2 (\tilde{n} \cdot \nabla \times \tilde{n})^2 + \frac{1}{2} K_3 (\tilde{n} \times \nabla \times \tilde{n}) + \frac{1}{2} (K_2 + K_4) \nabla \cdot [(\tilde{n} \cdot \nabla) \tilde{n} - (\nabla \cdot \tilde{n}) \tilde{n}] \quad (1-13)$$

where K_1 , K_2 , K_3 , and K_4 are called Frank elastic constants, and are equal to k_{11} , k_{22} , k_{33} , and k_{24} , respectively. Eq. (1-13) is called Frank-Oseen elastic free energy density for NLCs. In many cases, the one-constant approximation is applied in Eq. (1-13) using the following condition.

$$K \equiv K_1 = K_2 = K_3, \quad K_4 = 0. \quad (1-14)$$

Thus, we obtain a more simplified form of the elastic free energy density as follows.

$$w_F = \frac{1}{2} K \|\nabla \tilde{n}\|^2 = \frac{1}{2} K n_{i,j} n_{i,j}, \quad (1-15)$$

In Eq. (1-12), G_i is the generalized body force, λ is a Lagrange multiplier, and \dot{u}_i represents the material time derivative of velocity field as follows.

$$\dot{u}_i = \frac{\partial u_i}{\partial t} + u_j u_{i,j}. \quad (1-16)$$

ρF_i and G_i are calculated from

$$\rho F_i = \frac{\partial \Psi}{\partial x_i}, \quad G_i = \frac{\partial \Psi}{\partial n_i}, \quad (1-17)$$

$$\Psi = -\rho \Psi_g + \Psi_e, \quad (1-18)$$

where Ψ_g is the gravitational potential, and Ψ_e is the electric energy density, which is given by

$$\Psi_e = \frac{1}{2} \varepsilon_o \varepsilon_a (n_i E_i)^2, \quad (1-19)$$

where ε_o and ε_a are the permittivity of the free space and the dielectric anisotropy of the NLC, respectively, and E_i is an external electric field. The constitutive equation for the viscous stress (\tilde{t}_{ij}) and other variables are given by

$$\tilde{t}_{ij} = \alpha_1 n_k A_{kp} n_p n_i n_j + \alpha_2 N_i n_j + \alpha_3 n_i N_j + \alpha_4 A_{ij} + \alpha_5 n_j A_{ik} n_k + \alpha_6 n_i A_{jk} n_k, \quad (1-20)$$

$$\tilde{g}_i = -\gamma_1 N_i - \gamma_2 A_{ip} n_p, \quad (1-21)$$

$$N_i = \dot{n}_i - W_{ij} n_j, \quad (1-22)$$

$$\gamma_1 = \alpha_3 - \alpha_2, \quad \gamma_2 = \alpha_3 + \alpha_2, \quad (1-23)$$

$$A_{ij} = \frac{1}{2} (u_{i,j} + u_{j,i}), \quad (1-24)$$

$$W_{ij} = \frac{1}{2} (u_{i,j} - u_{j,i}), \quad (1-25)$$

where $\alpha_1, \alpha_2, \dots, \alpha_6$ are the Leslie viscosities, N_i is the co-rotational time flux of the director, and A_{ij} and W_{ij} are the strain rate tensor and the vorticity tensor, respectively.

In Poiseuille flow of the NLCs not involving any external forces such as the magnetic or the electric field, the orientation of directors is determined from the balance of inertial, viscous, and the elastic forces.^[10] If $\alpha_2 \alpha_3$ is positive, the directors rotate toward the direction of flow due to the viscous torque induced by the flow.^[1,19] To estimate a contribution of viscous force and elastic force, the following dimensionless number is introduced.^[1]

$$Er = \frac{\mu u L}{K}, \quad (1-26)$$

where μ is the viscosity of NLC, u is the typical flow velocity, L is the characteristic length, and K is the elastic constant. In Eq. (1-26), Er is called Ericksen number. The numerator and the denominator on the right side of Eq. (1-

26) correspond to the viscous force and the elastic force, respectively. At high Er , the rotation angle is similar to Leslie angle (θ_o) or the flow alignment angle as given by^[1,18]

$$\theta_o = \frac{1}{2} \cos^{-1} \left(-\frac{\gamma_1}{\gamma_2} \right). \quad (1-27)$$

It is straightforward to expect that a viscosity of NLC varies with its orientation relative to the flow direction. Fig. 1.9 shows the configurations between the director orientations and the flow directions. Viscosities at these configurations were firstly measured by Miesowicz in 1946.^[20] He used a strong magnetic field to align NLCs and measured viscosities using an oscillating plate viscometer.^[1] In Fig. 1.9a, the director (\tilde{n}) is parallel to the flow velocity (\tilde{v}). In Fig. 1.9b, \tilde{n} is parallel to the gradient of velocity ($\nabla\tilde{v}$). Fig. 1.9c shows the configuration that \tilde{n} is perpendicular to \tilde{v} and $\nabla\tilde{v}$. At each configuration, the viscosities are denoted with η_1 , η_2 , and η_3 , respectively, and called Miesowicz viscosities. By a hydrodynamic theory based on the continuum theory, the Miesowicz viscosities are calculated as follows.^[1]

$$\eta_1 = \frac{1}{2} (\alpha_3 + \alpha_4 + \alpha_6) = \frac{1}{2} (\alpha_2 + 2\alpha_3 + \alpha_4 + \alpha_5), \quad (1-28)$$

$$\eta_2 = \frac{1}{2} (-\alpha_2 + \alpha_4 + \alpha_5), \quad (1-29)$$

$$\eta_3 = \frac{1}{2} \alpha_4, \quad (1-30)$$

Typically, the order of Miesowicz viscosities is given as $\eta_2 > \eta_3 > \eta_1$.

1.2.3. Phase transition in heterogeneous mixture

A low molar mass LC acts as a solvent in a heterogeneous mixture composed of monomer and LC. In particular, such characteristic is important for phase behavior, morphological characterization, polymerization kinetics, phase separation

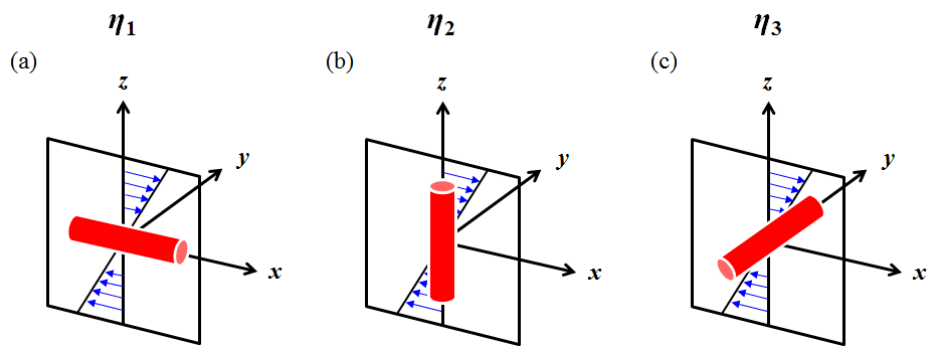


Figure 1.9 Three possible configurations between the director orientations (\tilde{n}) and the flow directions. The flow direction is parallel to x -axis. The planes including the blue arrows mean the shear planes. (a) \tilde{n} is parallel to \tilde{v} (velocity field), (b) \tilde{n} is parallel to $\nabla\tilde{v}$, and (c) \tilde{n} is perpendicular to \tilde{v} and $\nabla\tilde{v}$.^[1]

dynamics, electro-optical characterization, and optimization of device performance related with LC/polymer composites commonly referred to as polymer dispersed liquid crystal (PDLC) film.^[21]

In a mixture of LC and polymer, the LC exists as separated phases or coexists with the swollen polymer according to the volume fraction of LC and temperature. In this section, schemes and notations for calculation of a phase diagram are referred from works of Kyu *et al.*^[21,22] Also, it is assumed that the PDLC comprises NLCs and UV curable polymers (*i.e.*, cross-linked polymers). The total free energy density of binary system (g) can be expressed as the summation of free energy density of isotropic mixing (g^i), free energy density of nematic ordering (g^n), and free energy density caused by cross-linked network elasticity (g^e) as follows.

$$g = g^i + g^n + g^e . \quad (1-31)$$

According to Flory-Huggins (F-H) lattice model,^[23] g^i is written as

$$g^i = \frac{\Delta G^i}{Nk_B T} = \frac{\phi_L \ln \phi_L}{R_L} + \frac{\phi_P \ln \phi_P}{R_P} + \chi \phi_L \phi_P , \quad (1-32)$$

where ΔG^i is the free energy of isotropic mixing, k_B is the Boltzmann constant, T is the absolute temperature, ϕ_L and ϕ_P are the volume fraction of NLC phase and the polymer phase respectively, and χ is the F-H isotropic mixing interaction parameter. N is the total number of molecules given as

$$N = N_L R_L + N_P , \quad (1-33)$$

where N_L is the number of NLC molecules occupying R_L sites. The cross-linked polymer network is regarded as one giant molecule composed of N_P monomers.^[21] Then, ϕ_L and ϕ_P are calculated by

$$\phi_L = \frac{N_L R_L}{N} , \quad \phi_P = \frac{N_P}{N} = 1 - \phi_L . \quad (1-34)$$

In Eq. (1-32), the term of $(\phi_P \ln \phi_P)/R_P$ can be neglect because the polymer network has infinite molecular weight ($R_P = \infty$). Therefore, Eq. (1-32) can be written by

$$g^i = \frac{\Delta G^i}{Nk_B T} = \frac{\phi_L \ln \phi_L}{R_L} + \chi \phi_L \phi_P. \quad (1-35)$$

χ can be represented by

$$\chi = A + \frac{B}{T}, \quad (1-36)$$

where A and B are constants.

The nematic ordering free energy density (g^n) is expressed by the Maier-Saupe theory as follow.^[24]

$$g^n = \frac{\Delta G^n}{Nk_B T} = \frac{1}{R_L} \left[-\phi_L \ln z + \frac{1}{2} v \phi_L^2 s^2 \right], \quad (1-37)$$

where ΔG^n is the free energy of nematic ordering. z and s are the normalized partition function and the nematic order parameter, respectively, which are calculated as follows.

$$z = \int_0^1 \exp\left(\frac{3}{2} m x^2 - \frac{1}{2} m\right) dx, \quad (1-38)$$

$$s = \frac{3}{2z} \int_0^1 x^2 \exp\left(\frac{3}{2} m x^2 - \frac{1}{2} m\right) dx - \frac{1}{2}, \quad (1-39)$$

where m is a mean field parameter representing the strength of the orientational potential field of the NLC directors,^[21] which is proportional to v , ϕ_L , and s as follows.

$$m = v \phi_L s, \quad (1-40)$$

where v is the Maier-Saupe interaction parameter which is defined as

$$\nu = 4.541 \frac{T_{NI}}{T}, \quad (1-41)$$

where T_{NI} is the nematic-to-isotropic temperature of the NLC. The constant 4.541 in Eq. (1-41) is given as the value for E7 (commercially available mixture of NLCs from Merck), which is selected only as an example for a numerical analysis of an imaginary PDLC system.^[25]

The elastic free energy density (g^e) is given by Dusek *et al.* as follows.^[26-28]

$$g^e = \frac{\Delta G^e}{Nk_B T} = \left(\frac{3\alpha_e}{2R_c} \right) \Phi_o^{2/3} (\phi_P^{1/3} - \phi_P) + \left(\frac{\beta_e}{R_c} \right) \phi_P \ln \phi_P, \quad (1-42)$$

where ΔG^e is the elastic free energy, R_c is the segment length between cross-links. Φ_o is the volume fraction of the network in an unswollen state. Here it is regarded as $\Phi_o = \phi_p$.^[21] The network parameters, α_e and β_e , can be expressed as^[29]

$$\alpha_e = 1, \quad \beta_e = \frac{2}{f}, \quad (1-43)$$

where f is the network functionality with the range from 3 to infinity.

Equilibrium between two coexisting phases is positioned at points where the chemical potential of each component is equivalent. The phases of swollen network and the pure NLC are denoted as phase I and II for the mixture of NLC and the cross-linked polymer, respectively. The balance of chemical potentials between the phase I and II is written by

$$\left(\frac{\Delta \mu_L}{k_B T} \right)^I = \left(\frac{\Delta \mu_L}{k_B T} \right)^{II} \quad (1-44)$$

For each phase, the following conditions are satisfied.

$$\phi_L^I + \phi_p^I = 1, \quad (1-45)$$

$$\phi_L^H = 1, \quad \phi_P^H = 0, \quad (1-46)$$

where $\phi_P^H = 0$ means that the polymer network is not dissolved in the NLC phase.

Similarly with Eq. (1-31), the chemical potential normalized with $k_B T$ is calculated as follows.

$$\frac{\Delta\mu_L}{k_B T} = \frac{\Delta\mu_L^i}{k_B T} + \frac{\Delta\mu_L^n}{k_B T} + \frac{\Delta\mu_L^e}{k_B T}. \quad (1-47)$$

The normalized chemical potential for the isotropic mixing of NLC solvent is given as

$$\frac{\Delta\mu_L^i}{k_B T} = \frac{\partial(\Delta G^i / k_B T)}{\partial N_L} = \ln \phi_L + \phi_P + \chi \phi_P^2. \quad (1-48)$$

The normalized chemical potential for the nematic ordering of NLC solvent is represented by

$$\frac{\Delta\mu_L^n}{k_B T} = \frac{\partial(\Delta G^n / k_B T)}{\partial N_L} = -\ln z + \frac{1}{2} v \phi_L^2 s^2. \quad (1-49)$$

If α_e and β_e are independent of ϕ_P , the elastic chemical potential is written by^[21]

$$\frac{\Delta\mu_L^e}{k_B T} = \frac{\partial(\Delta G^e / k_B T)}{\partial N_L} = \frac{1}{R_c} [\alpha_e \phi_P - \beta_e (1 + \ln \phi_P)]. \quad (1-50)$$

Now, we can obtain the following equation representing the equilibrium condition by substituting Eqs. (1-48), (1-49) and (1-50) into Eq. (1-47).

$$\left[\ln \phi_L + (1 - \phi_L) + \chi(1 - \phi_L^2) - \ln z + \frac{1}{2} v \phi_L^2 s^2 + \frac{1 - \phi_L}{R_c} (\alpha_e - \beta_e) \right]^I = \left[-\ln z + \frac{1}{2} v s^2 \right]^{II} \quad (1-51)$$

Using Eq. (1-51), Kyu *et al.* calculated and plotted the theoretical phase diagram for a mixture of the NLC and the cross-linked polymer as shown in Fig. 1.10. The parameters for the plotting were assumed to be $T_{NI} = 42$ °C, $f = 3$, $R_L = 1$, and $R_c = 10$.^[21] The curve shows an upper critical solution temperature (UCST). Below the UCST curve, NLCs exist as separated phases from the cross-linked polymer phases. In regime of I + N, the NLCs exist as the nematic phases (N) in the isotropic polymer phases (I) because of $T < T_{NI}$. However, the NLCs exist as the isotropic phases (I) in the isotropic polymer phases (I) in regime of I + I over at $T = T_{NI}$. Above the curve, the cross-linked polymer phases are swollen by the NLC solvent, so that the overall phases exist as the isotropic single phases.

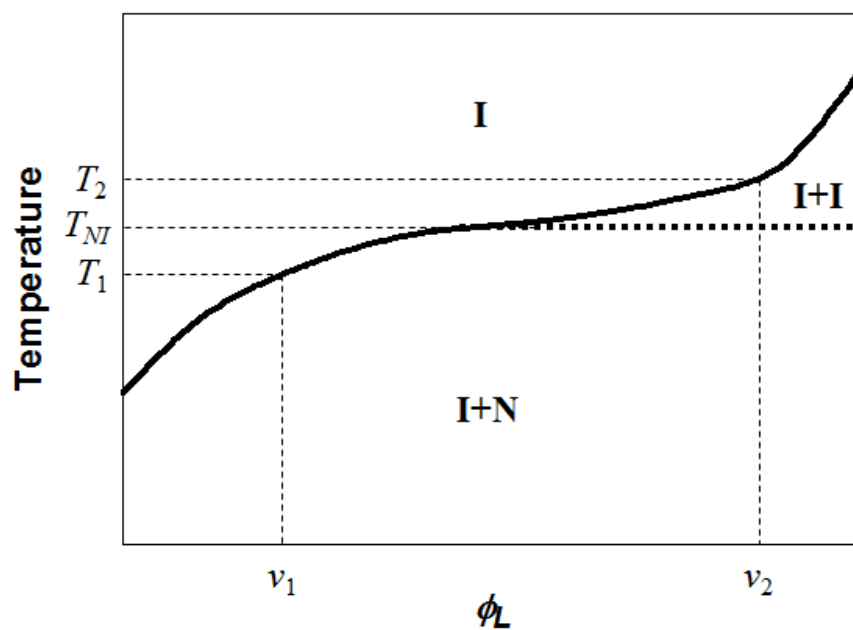


Figure 1.10 Theoretical phase diagram for a mixture of the NLC and the cross-linked polymer. This graph was redrawn from the result of Ref. 21.

1.3. Applications of liquid crystals

1.3.1. Liquid crystal display and its related optical films

The most fascinating application of LCs is liquid crystal displays (LCDs). The LCDs have been used in many products such as notebook computers, mobile phones, televisions due to their competitive performances and low product cost compared with other displays, for example, cathode ray tube (CRT) displays, plasma display panels (PDPs), and organic light emitting displays (OLEDs).

Fig. 1.11 shows a schematic structure of the LCD. The LCD consists of the panel part and the backlight unit part. Light emitted from light sources such as light emitting diodes (LEDs) or cold cathode fluorescent lamps (CCFLs) is incident into the light-guide plate made of poly(methyl methacrylate) (PMMA), and is converted into a surface light source passing through optical films such as a prism film and a light diffusing film. Crossed-polarizers are attached on both sides of the panel. Therefore, the unpolarized light can't pass through the panel at off-state. However, a light transmission can be adjusted by changing the phase difference of propagated light in the medium of LCs via the field-induced orientation. Accordingly, LCs in the LCD act as an optical shutter. In order to control the electric field, thin film transistor (TFT) arrays exist at each pixel. The alignment layers, which are made by coating a polyimide and rubbing, are coated on the both substrates to fix an initial orientation of LCs.

LCs are also used in many optical films for the LCDs. Because the LCDs use dichroic polarizers, a half of light emitted from the backlight unit is absorbed by the polarizer on the bottom glass substrate. Therefore, a reflective polarizer film is sometimes positioned between the panel and the light-guide plate to enhance a light utilizing efficiency. As mentioned in the section 1.1.2, the CLC film can be used as the reflective polarizer. The unpolarized light emitted from the backlight unit is decomposed into the clockwise and the counter-clockwise circularly polarized light in the medium of CLC, and then one component of the decomposed light is transmitted, and the other component is reflected. The reflected light can be recycled by polarization conversion through a multi-reflection in the backlight unit.

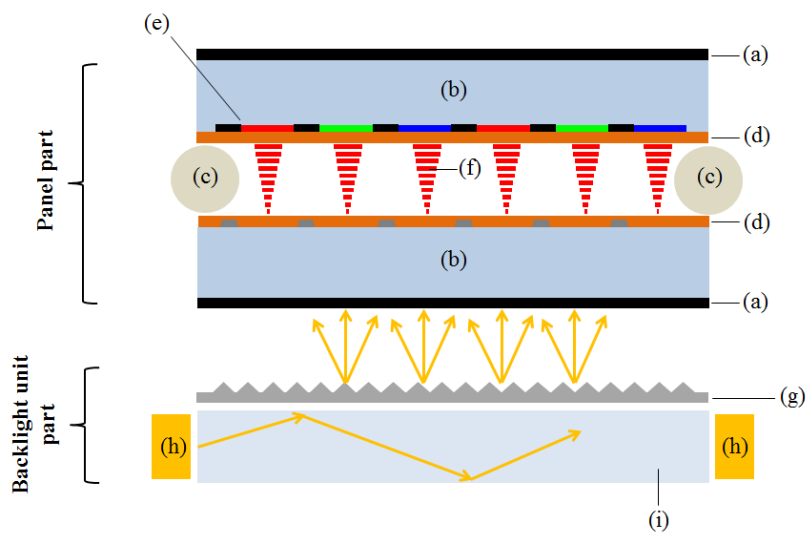


Figure 1.11 A schematic structure of LCD: (a) polarizers, (b) glass substrates, (c) spacers, (d) alignment layers, (e) color filter array, (f) LCs, (g) optical film, (h) light sources, and (i) light-guide plate.

Generally, a retarder film (as commonly referred to as the $\lambda/4$ film) is coated on the CLC film in order to convert the transmitted circularly polarized light into the linearly polarized light. If the transmission axis of the CLC film corresponds with that of the linear polarizer on the bottom glass substrate, the light utilizing efficiency of the LCD can be improved. Here, the LCs used in the CLC films include reactive mesogen unit, so that their orientations can be permanently fixed by curing via an exposure of ultraviolet (UV) light.

1.3.2. Polymer dispersed liquid crystal

Polymer dispersed liquid crystals (PDLCs), was firstly reported in 1985,^[30] are thin films with electrically controllable scattering obtained by phase separation between micrometer-sized droplets of LC phases and a continuous polymer matrix.^[31] Fig. 1.12 illustrates a schematic structure of the PDLC film. The PDLC layer is inserted into two transparent electrodes such as ITO coated glasses. In the PDLC, n_o of LC should be matched with the refractive index of the polymer matrix (n_p). At off-state, the refractive indices of droplets (n_{eff}) are some values between n_o and n_e because average directions of the directors in droplets are randomly oriented as shown in Fig. 1.12a. Therefore, the transmitted light is scattered due to an index mismatching between n_{eff} and n_p at off-state. However, the light is transmitted without the scattering at on-state because the directors are aligned along the direction of electric field corresponding to the thickness direction in Fig. 1.12b, so that the incident light can't recognize the boundaries between the LC phase and the polymer matrix due to the index matching ($n_o = n_p$) for the normally incident light as shown in Fig. 1.12b.

The PDLC films can be adopted in smart windows due to their transmittance tunability,^[32] and have many advantages compared with the LCD since they don't need the polarizers and the alignment layers.^[16]

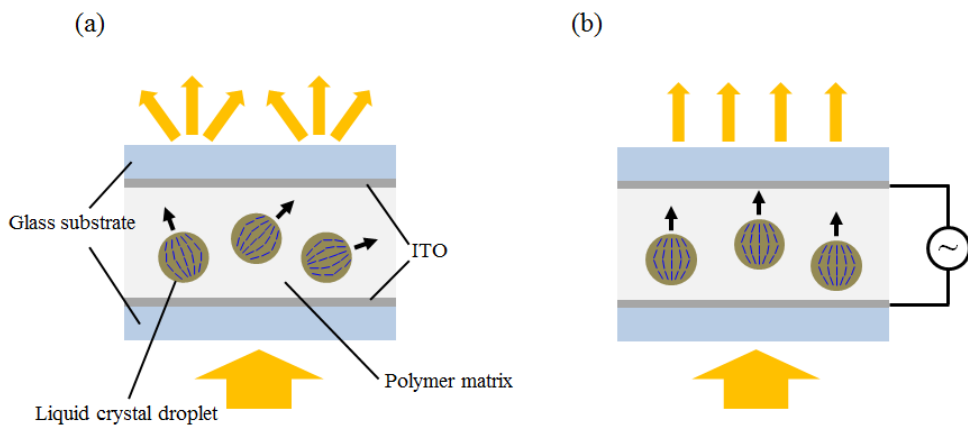


Figure 1.12 A schematic diagram for the PDLC film at (a) off-state and (b) on-state. Black arrows represent a mean direction of the directors in a droplet.

1.3.3. Microfluidic applications

Various researches for applications of LCs using microfluidic systems have been reported for the past few decades. Jewell *et al.*^[33] observed the orientation of 5CB in a microchannel, and calculated the tilt angle induced by flow using a simple one-dimensional model derived from the Ericksen-Leslie equations.^[18] They revealed that a transition from a near-vertical (V) state to a partially horizontal (H) state was induced in a homeotropically aligned NLC undergoing Poiseuille flow through a microchannel by driving it above a critical flow rate. Sengupta *et al.*^[34] demonstrated a velocity meter using a microchannel filled with 5CB. The flow-induced reorientation of 5CB in a diverging channel produced distinct birefringent domains, so that one could directly observe interference colors of 5CB, which were characteristic to the local flow velocity. Similarly, Cuennet and co-workers reported an application for a tunable color filter using a change of birefringence by the flow-induced reorientation of 5CB.^[35] Additionally, NLC in a microchannel can be used as a bio sensor. Khan *et al.* reported a pH-sensitive bio sensor for an urea detection.^[36] They utilized 5CB droplets with amphiphilic poly(acrylicacid-b-4-cyanobiphenyl-4-oxyundecylacrylate) (PAA-b-LCP). When the urea was immobilized on PAA chains, a configuration change of the directors in NLC droplets could be observed. As a result, they could detect urea of 3mM from polarized optical microscope (POM) images.

1.4. Objectives of present work

Most applications of NLCs have been focused on properties related to the anisotropic permittivity among outstanding features of NLCs. However, the properties regarding the fluidic anisotropy and the phase transition of NLCs are investigated in this study. In detail, we focus on an optical anisotropy under an application of electric field in dynamic state and the thermo-optical properties in static state and. These characteristics are used for microscopic and macroscopic applications.

In a point of view of the microscopic application, a birefringent lens system is considered in this study. Miniaturization of optical system including a microlens has been an important work in research fields of imaging, optical communication, photolithography and lab on chips (LOC) in the past few years.^[37] The microlens has been fabricated by various methods such as reflow of photoresists, patterning of ultraviolet (UV) curable resins using a micro-mold, and printing using inkjet printers.^[37] However, the above-mentioned methods are usually suitable for static optical systems based on solid materials. Regarding the birefringent lens, solid phase microlens can be made using reactive mesogens exhibiting a NLC phase.^[38] Also, a focal length variable microlens array can be fabricated by filling NLC into a micro-cavity composed of transparent electrodes of lens shape and being applied under an electric field.^[39] These birefringent lens systems generally provide focal points on an out-of-plane, so that they are not adequate for integrated microfluidic systems.

To achieve both of optically anisotropic characteristics and tunable focal point on the in-plane, we demonstrate an optofluidic birefringent lens in Part II using hydrodynamic liquid-liquid (L^2) interfaces in a microchannel. The birefringent L^2 lens can provide an intrinsically smooth interface due to using liquids as an optical medium, and easily change optical properties by replacing the liquid flowing in the microchannel. The birefringent L^2 lens presented in this study comprises a NLC phase as the main stream and an optically isotropic phase for the sub stream. In this microfluidic device, L^2 interfaces which are adjusted by changing a flow rate act as plano-convex lens. Also, orientations of the NLC under an application of a strong electric field assign an optically anisotropic characteristic to this system.

Furthermore, a concept of the system and experimental observations are supported by numerical analyses using the Ericksen-Leslie equation based on the continuum theory.

In an aspect of the macroscopic application, a thermal-induced PDLC film is also proposed in this study. As previously mentioned, the conventional PDLC films are operated by applying an electric field for the field-induced orientations of NLC droplets. However, the conventional PDLC films have some disadvantages. Firstly, they require a high electric field of several ten or hundred voltage. Such high driving voltage depends on not a size but a thickness of PDLC film. Therefore, the conventional PDLC film is unfavorable for small-sized applications. Also, it is restrictive to improve the contrast which is defined as transmittance difference at on- and off-state. To improve the contrast, a number of LC droplets had to be included in the PDLC film, so that it should be thicker at same volume fraction of LC to increase the contrast. But this work leads to a high driving voltage. In addition, electrically high conductive and transparent electrodes are essential to the conventional PDLC film. Thereby, indium tin oxide (ITO) coated glasses are usually used for the transparent electrodes, but an expensive process such as the deposition is involved for the fabrication of ITO glasses. Furthermore, ITO glasses (or film) are not adequate for applications such as flexible devices due to a brittle property of ITO. Finally, the conventional PDLC film at on-state shows angular dependent transmittance because it brings about the index mismatching between the LC droplets and polymer matrix when it is observed at off-angle. As a result, the conventional PDLC film exhibits a lower transmittance at off-angle compared to when observed at normal direction.

To solve such problems of the conventional PDLC film, a novel thermo-sensitive smart film (TSF) is demonstrated in Part III. The TSF consists of the PDLC layer exhibiting the phase transition behavior and a silver nanowire (AgNW) coated film to provide thermal energy via Joule heating. The TSF changes from an opaque to a transparent state at the transition temperature as a result of the phase transition of the liquid crystal. The AgNW, a promising material for replacing ITO, shows not only low sheet resistance and high transmittance with a low processing cost but also good flexibility. In addition, it is more advantageous to enhance the contrast of the TSF because a limitation for the thickness is

relatively weak due to being driven by not electric-field but thermal energy compared to the conventional PDLC film. Also, the TSF shows a uniform transmittance at wide-viewing-angle because it has no angular dependency due to driven by not the field induced orientation but the phase transition. However, the TSF has some drawbacks such as slow response and low energy efficiency due to use of the phase transition. To overcome these problems, a dynamic power control as an operation method of the TSF is presented in this study. Additionally, thermo-optical properties of the TSF are investigated by carrying out experimental and numerical analyses. From these results, we aim to predict temperature-dependent transmittance of the TSF by combining anomalous diffraction approach (ADA) as a light scattering theory and the phase transition of PDLC.

1.5. References

- [1] I. W. Stewart, *The static and dynamic continuum theory of liquid crystals: a mathematical introduction*, Crc Press, 2004.
- [2] I.-C. Khoo, *Liquid crystals: physical properties and nonlinear optical phenomena*, John Wiley & Sons, 2007.
- [3] F. Reinitzer, *Liq. Cryst.*, 1989, 5, 7-18.
- [4] N. Puech, C. Blanc, E. Grelet, C. Zamora-Ledezma, M. Maugey, C. Zakri, E. Anglaret, P. Poulin, *J. Phys. Chem. C*, 2011, 115, 3272-3278.
- [5] Z. Xu, C. Gao, *ACS Nano*, 2011, 5, 2908-2915.
- [6] J. Y. Kim, S. O. Kim, *Nat. Mater.*, 2014, 13, 325.
- [7] J. E. Kim, T. H. Han, S. H. Lee, J. Y. Kim, C. W. Ahn, J. M. Yun, S. O. Kim, *Angew. Chem. Int. Edit.*, 2011, 50, 3043-3047.
- [8] S. J. Eichhorn, *Soft Matter*, 2011, 7, 303-315.
- [9] J. A. Rego, J. A. Harvey, A. L. MacKinnon, E. Gatdula, *Liq. Cryst.*, 2009, 37, 37-43.
- [10] A. Sengupta, *Topological microfluidics: nematic liquid crystals and nematic colloids in microfluidic environment*, Springer Science & Business Media, 2013.
- [11] L. Gattermann, A. Ritschke, *Ber. Dtsch. Chem. Ges.*, 1890, 23, 1738-1750.
- [12] H. Kelker, B. Scheurle, *Ang. Chem. Int. Edit.*, 1969, 8, 884-885.
- [13] G. W. Gray, K. J. Harrison, J. Nash, *Electron. Lett.*, 1973, 9, 130-131.
- [14] D. B. Heimoponnath, *Schematic representation of cholesteric phase*, <https://commons.wikimedia.org/wiki/File:Cholesterinisch.png>, accessed: September, 2015.
- [15] D.-K. Yang, *Fundamentals of liquid crystal devices*, John Wiley & Sons, 2014.
- [16] P. J. Collings, M. Hird, *Introduction to liquid crystals: chemistry and physics*, Taylor & Francis, 1997.
- [17] J. L. Ericksen, *T. Soc. Rheol.*, 1961, 5, 23-34.
- [18] F. M. Leslie, *Arch. Ration. Mech. An.*, 1968, 28, 265-283.
- [19] A. Sengupta, S. Herminghaus, C. Bahr, *Applied Physics Letters*, 2012, 101, 164101.
- [20] M. Miesowicz, *Nature*, 1946, 158, 27.
- [21] D. Nwabunma, T. Kyu, *Macromolecules*, 1999, 32, 664-674.

- [22] H. W. Chiu, T. Kyu, *The Journal of chemical physics*, 1995, 103, 7471-7481.
- [23] P. Flory, M. Volkenstein, *Statistical Mechanics of Chain Molecules*, Wiley Online Library, 1969.
- [24] W. Maier, A. Saupe, *IZ Naturforsch*, 1959, 14, 882-889.
- [25] F. Benmouna, L. Bedjaoui, U. Maschke, X. Coqueret, M. Benmouna, *Macromol. Theory Simul.*, 1998, 7, 599-611.
- [26] K. Dušek, "Phase separation during the formation of three-dimensional polymers", presented at *Journal of Polymer Science Part C: Polymer Symposia*, 1967.
- [27] K. Dušek, W. Prins, *Structure and elasticity of non-crystalline polymer networks*, Springer, 1969.
- [28] R. Moerkerke, R. Koningsveld, H. Berghmans, K. Dusek, K. Solc, *Macromolecules*, 1995, 28, 1103-1107.
- [29] P. J. Flory, *The Journal of Chemical Physics*, 1950, 18, 108-111.
- [30] J. Doane, N. Vaz, B. G. Wu, S. Žumer, *Appl. Phys. Lett.*, 1986, 48, 269-271.
- [31] M. Mucha, *Prog. Polym. Sci.*, 2003, 28, 837-873.
- [32] R. Baetens, B. P. Jelle, A. Gustavsen, *Sol. Energy Mater. Sol. Cells*, 2010, 94, 87-105.
- [33] S. A. Jewell, S. L. Cornford, F. Yang, P. Cann, J. R. Sambles, *Phys. Rev. E*, 2009, 80, 041706.
- [34] A. Sengupta, S. Herminghaus, C. Bahr, *Appl. Phys. Lett.*, 2012, 101, 164101.
- [35] J. Cuennet, A. E. Vasdekis, D. Psaltis, *Lab. Chip.*, 2013, 13, 2721-2726.
- [36] M. Khan, S.-Y. Park, *Sensor. Actuat. B-Chem.*, 2014, 202, 516-522.
- [37] X. Zeng, H. Jiang, *J. Phys. D: Appl. Phys.*, 2013, 46, 323001.
- [38] G. J. Woodgate, J. Harrold, *SID Int. Symp. Dig. Tec.*, 2005, 36, 378-381.
- [39] Y. Choi, JH. Park, JH. Kim, SD. Lee, *Opt. Mater.*, 2002, 21, 643-646.

II. Optofluidic Birefringent Lens

2.1. Introduction

Optofluidic devices are implemented by combining fluidics with microphotronics.^[1] In comparison with solid material-based systems, they can offer unique properties: tunable optical feature of the device by simply changing a liquid, optically smooth interfaces between two immiscible fluids, and optically gradient property based on the diffusion phenomenon of miscible fluids.^[2] In this respect, a number of applications have been demonstrated, such as photo-bioreactors,^[3] optofluidic dye lasers,^[4] light filter controllers,^[5-7] and optical components using dynamic liquid-liquid (L^2) interfaces.^[8] In particular, L^2 lenses have widely been investigated for on-chip integration.^[9] Tang *et al.* firstly introduced a dynamically reconfigurable microfluidic lens in a rectangular chamber using a laminar flow of three streams.^[10] They demonstrated various types of L^2 lens such as meniscus, plano-convex, and biconvex by adjusting flow rates of core and cladding streams, and proposed a correlation between flow rates and focal distances. Chao *et al.* introduced a microfluidic chip embedding an in-plane biconvex microlens and an in-plane microprism.^[11] Mao *et al.* reported a hydrodynamically tunable cylindrical lens prepared by using a centrifugal effect of a curved channel.^[12,13]

In this part, an optofluidic birefringent lens is demonstrated in combination with the NLC and an isotropic fluid. While most studies on L^2 lenses have been carried out using an isotropic system, *i.e.*, a single focal point exists regardless of the polarization direction of incident light, we constructed a plano-convex lens with help of streams of the NLC and the isotropic fluid under an electric field. Fig. 2.1 shows the concept of birefringent L^2 lens in this study. A positive birefringent NLC was used as the main fluid, and an isotropic fluid was adopted for the sub-fluid of which refractive index (n_i) was lower than that of the NLC. Transparent electrodes were employed to apply the electric field to the birefringent L^2 lens and control the orientation of NLC. They were positioned on the top and bottom surfaces of the microchannel, so that the electric field could be applied in

perpendicular to flow direction. When the NLCs are aligned along the direction of the electric field (z-direction in Fig. 2.1), the L^2 lens can act as a birefringent lens. If an incident light is p-polarized (p-mode), the effective refractive index (n_{eff}) in the phase of NLCs is equal to n_{\perp} as shown in the schematic index ellipsoid of NLCs in Fig. 2.2a. When an s-polarized light (s-mode) is applied as shown in Fig. 2.1b, n_{eff} is equivalent to n_{\parallel} (Fig. 2.2b). The difference between the effective refractive index in the NLC phase and the isotropic refractive index ($n_{eff} - n_i$) of the s-mode is larger than that of the p-mode because n_{\parallel} is larger than n_{\perp} . As a result, the focal length in the s-mode is shorter than that in the p-mode. In this sense, the optofluidic chip introduced in this study can provide two different ways to control the focal length, *i.e.*, by changing the curvature of L^2 interface and the polarized direction of incident light.

Hydrodynamic behaviors of NLCs have been described by the Ericksen-Leslie (E-L) equations based on the continuum theory.^[14-16] Directors, which imply the local direction of the average molecular alignment in LCs,^[17] are aligned in the direction of the applied electric field at static state if they have a positive dielectric anisotropy. On the other hand, they can be oriented parallel to flow direction at dynamic state if $\alpha_2\alpha_3$ (α_2 and α_3 are the second and third Leslie viscosities) is positive.^[17] In this study, the electric field induced orientation of NLCs were employed rather than the flow induced orientation. To decide appropriate flow rates and an electric field, a numerical simulation was carried out using the Ericksen-Leslie (E-L) equations and dimensionless analysis. Also, the L^2 interfaces and the focal lengths were numerically calculated and compared with experimental results.

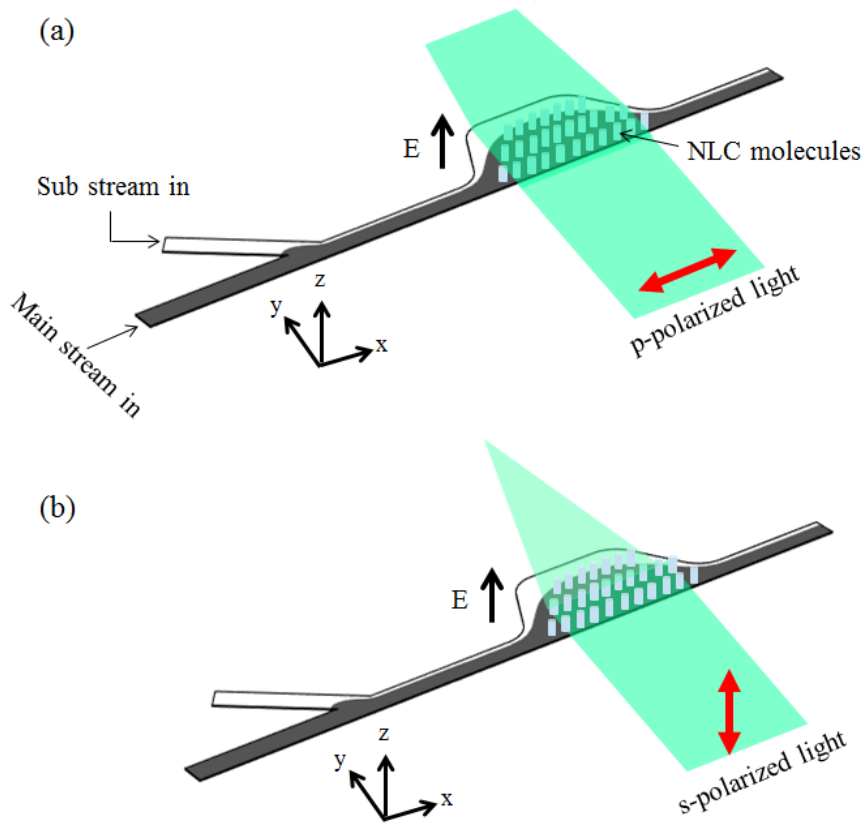


Figure 2.1 Concept of the birefringent L^2 lens for (a) p-polarized and (b) s-polarized incident light. The red arrows represent the polarization direction of light.

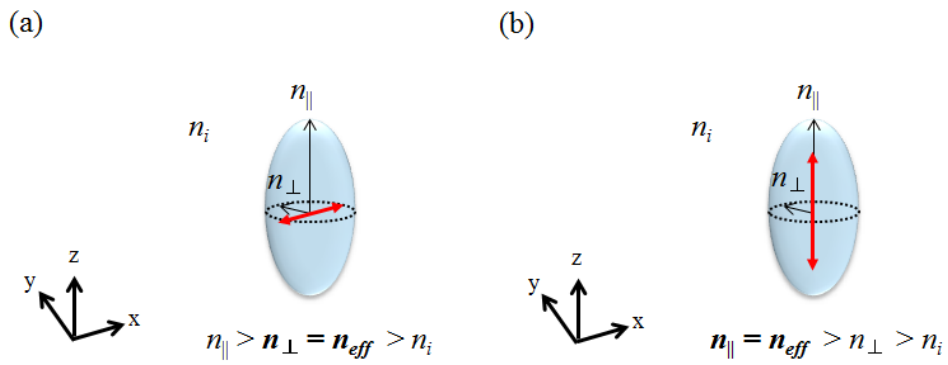


Figure 2.2 Index ellipsoids for (a) p-polarized and (b) s-polarized light. The red arrows represent the polarization direction of light.

2.2. Experimental

2.2.1. Design of optofluidic chip

Fig. 2.3 shows the configuration of optofluidic chip prepared in this study. The NLC and the isotropic fluid flowed through the main channel and the sub-channel, respectively. The merged stream in the expansion chamber led to the formation of a plano-convex L^2 lens. The incident light was collimated toward the expansion chamber as shown in Fig. 2.3. The aperture channels were prepared by filling an uncured black epoxy resin. The light passing through the expansion chamber was focused in the ray-tracing chamber filled with a fluorescent dye solution. The width and height of the channels were $200\ \mu\text{m}$ and $25\ \mu\text{m}$, respectively. The detailed dimensions of the optofluidic chip are depicted in Fig. 2.4.

2.2.2. Fabrication of optofluidic chip

The mold was fabricated by a conventional photo-lithography process. A negative photoresist (SU-8) was spin-coated on a silicon wafer with a thickness of $25\ \mu\text{m}$, and patterned using a photomask based on ultra-violet (UV) exposure process. The fabrication procedure of the optofluidic chip is illustrated in Fig. 2.5. A mixture of polydimethylsiloxane (PDMS) prepolymer and curing agent (Sylgard 184, Dow Corning) with 10:1 weight ratio was degassed and poured over the mold. The ITO coated glass ($1\ \text{mm}$ thick, $10\ \Omega\ \text{sq}^{-1}$ surface resistance) was treated by a corona discharger to enhance the adhesion strength with PDMS, and placed on the uncured PDMS. A weight of $4.34\ \text{kN}$ was placed on the ITO glass to minimize a thickness of residual PDMS layer (d in Step III of Fig. 2.5) because the applied electric field was weakened as d increased. After curing at $70\ ^\circ\text{C}$ for 2 h, the mold was detached from the cured PDMS replica, and d was measured to be $10\ \mu\text{m}$ by employing a micrometer. SiO_2 layer with a $500\ \text{nm}$ thickness

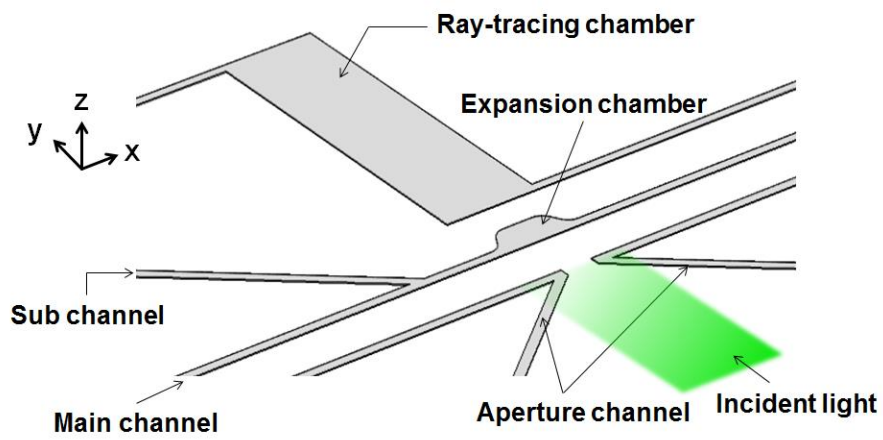


Figure 2.3 Configuration of the optofluidic chip used in this study.

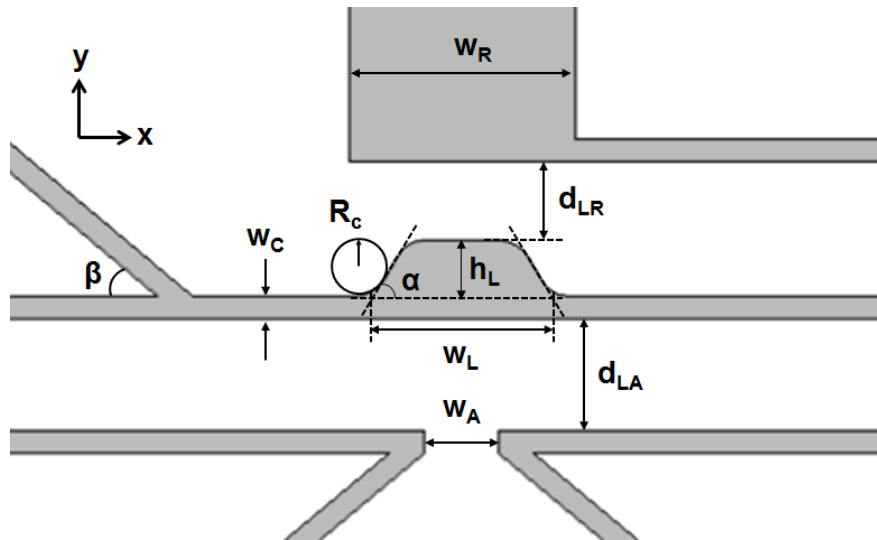


Figure 2.4 Dimension of the optofluidic chip. The inclination angle of chamber wall (α) is 60° , the angle between the main channel and the sub-channel (β) is 40° , the channel width (w_c) is $200 \mu\text{m}$, the width of the expansion chamber (w_L) and the aperture (w_A) are $1,800 \mu\text{m}$ and $662.5 \mu\text{m}$ respectively, the height of expansion chamber (h_L) is $700 \mu\text{m}$, d_{LA} is $1,000 \mu\text{m}$, and d_{LR} is $500 \mu\text{m}$. The radius of curvature of the expansion chamber (R_c) is $300 \mu\text{m}$.

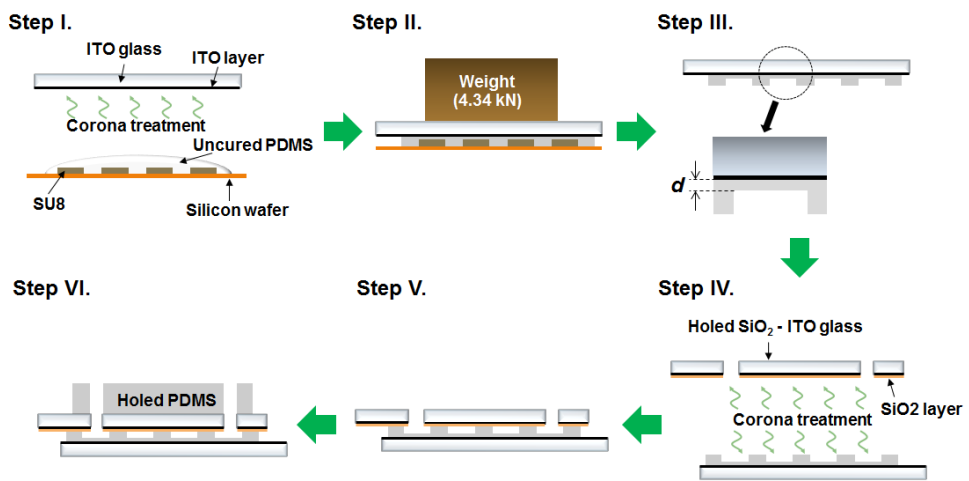


Figure 2.5 Schematic fabrication procedure of the optofluidic chip.

was deposited by e-beam deposition on the ITO coated glass with holes of 2 mm diameter to prevent an electrical short. The holes were positioned at the reservoirs in the cured PDMS replica. The prepared PDMS replica was bonded with the SiO₂-ITO coated glass through the corona treatment. The bonded sample was annealed at 110 °C for 2 h. A PDMS block with holes of 1 mm diameter for the connection of tubes and reservoirs was attached on the sample, and additionally annealed at 110 °C for 2 h.

2.2.3. Materials

4-cyano-4'-pentyl-1,1'-biphenyl (5CB, Tokyo Chemical Industry) was used as the main fluid. 5CB has n_{\perp} of 1.5442, n_{\parallel} of 1.7360,^[18] and a density (ρ_m) of 1.020 g cm⁻³.^[17] 2,2,2-trifluoroethanol ($n_D^{20} = 1.291$, $\mu = 1.73$ mPa s, $\rho = 1.370$ g cm⁻³, Sigma-Aldrich) is favourable as the sub-fluid because a large distinction of refractive indices between the main stream and the sub-stream could be achieved due to its low refractive index. However, its low viscosity and high density brought about unstable L² interfaces. Thereby, a mixture of 2,2,2-trifluoroethanol and cyclohexanol ($n_D^{20} = 1.464$, $\mu = 41.1$ mPa s, $\rho = 0.962$ g cm⁻³, Samchun Chemical) with an equivalent volume ratio was used for the sub-fluid. The refractive index (n_i) and the density (ρ_s) of the sub-fluid were 1.378 and 1.166 g cm⁻³, respectively. The viscosity of the sub-fluid (μ_s) was measured to be 4.7 mPa s by using a rheometer (Anton Paar, MCR302). 3 μ mol L⁻¹ of Rhodamine B (Sigma-Aldrich) was dissolved in 2,2,2-trifluoroethanol. It was used as a fluorescent dye solution to be filled in the ray-tracing chamber. The aperture channels were filled with an uncured black epoxy (MG Chemicals).

2.2.4. Experimental set-up for observation

Fig. 2.6 describes a schematic set-up for optical observation of the NLC orientation, L² interfaces, and ray paths. A square wave provided by a function generator

(Stanford Research Systems, Model DS335) was amplified with a high speed power amplifier (NF Electronics Instruments, 4010), and supplied to the top and bottom ITO electrodes of the optofluidic chip. The flow rates of the main stream and the sub-stream were manipulated using a N₂ gas pressure pump, which enabled us to provide a sufficiently small amount of fluid in a stable manner. Two syringes with an inner diameter of 9.5 mm were partially filled with the main fluid and the sub-fluid, and directly connected with the plastic tubes (10 mm outer diameter) which were linked with precision regulators (ControlAir Inc., 100LR). To identify exact pressure values, digital pressure gauges (OMEGA, DPG8001-60) were attached on the regulators. The syringes were connected to the optofluidic chip by polytetrafluoroethylene (PTFE) tubes (1 mm inner diameter and 1.6 mm outer diameter). The light source was a semiconductor laser (CNI Optoelectronics Technology CO., Ltd., PGL-FS-532) with a 532 nm wavelength. The laser, attached on a XYZ stage for beam alignment, was directly irradiated into the optofluidic chip. A dichroic linear polarizer was located between the laser and the optofluidic chip to control the polarization direction of incident light. The optofluidic chip was positioned in between a crossed linear polarizer pair. The NLC orientation, L² interfaces, and ray paths were observed by a CCD-equipped microscope.

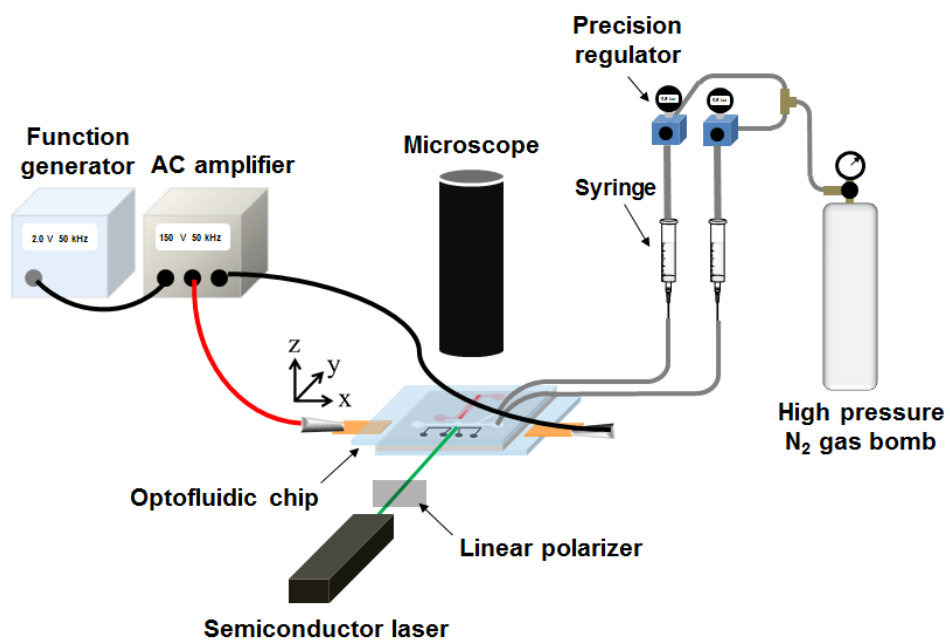


Figure 2.6 Experimental set-up for optical observation.

2.3. Numerical analyses

2.3.1. Orientation of directors in Poiseuille flow under strong electric field

Using the E-L equations, a numerical analysis based on the finite element method was carried out to check whether the director could be aligned in the direction of electric field in resistance to the viscous stress or not. However, the E-L equations reviewed in the section 1.2.2. are not suitable for the simulation because they include the Lagrange multiplier (λ) in the right side of Eq. (1-12). Therefore, the E-L equations of easy-to-handle forms were used in this study. λ can be eliminated by taking the scalar product of Eq. (1-12) with \tilde{n} and setting \tilde{n} as follows.^[17,19]

$$\tilde{n} = (\cos \theta_1 \cos \theta_2, \cos \theta_1 \sin \theta_2, \sin \theta_1), \quad \theta_1 = \theta(\tilde{x}, t), \quad \theta_2 = \phi(\tilde{x}, t), \quad (2-1)$$

where θ_1 and θ_2 are the inclination angle and the azimuthal angle with respect to the x -axis. Then, the constraint for the director in Eq. (1-9) is automatically satisfied. Other equations can be written by

$$u_{i,i} = 0, \quad (2-2)$$

$$\rho \dot{u}_i = -\tilde{p}_{,i} + \tilde{g}_j n_{j,i} + \tilde{t}_{ij,j}, \quad (2-3)$$

$$\left(\frac{\partial \hat{w}_F}{\partial \theta_{\alpha,i}} \right)_{,i} - \frac{\partial \hat{w}_F}{\partial \theta_\alpha} - \frac{\partial \hat{D}}{\partial \theta_\alpha} + \frac{\partial \hat{\Psi}}{\partial \theta_\alpha} = 0, \quad (2-4)$$

where

$$\tilde{p} = p + w_F - \Psi, \quad (2-5)$$

$$w_F = \hat{w}_F = \frac{1}{2} K n_{i,j} n_{i,j}, \quad (2-6)$$

$$\Psi = \hat{\Psi} = -\rho \Psi_g + \Psi_e, \quad (2-7)$$

$$\Psi_e = \frac{1}{2} \varepsilon_o \varepsilon_a (n_i E_i)^2, \quad (2-8)$$

$$\tilde{t}_{ij} = \alpha_1 n_k A_{kp} n_p n_i n_j + \alpha_2 N_i n_j + \alpha_3 n_i N_j + \alpha_4 A_{ij} + \alpha_5 n_j A_{ik} n_k + \alpha_6 n_i A_{jk} n_k, \quad (2-9)$$

$$D = 2\hat{D} = \alpha_1 (n_i A_{ij} n_j)^2 + 2\gamma_2 N_i A_{ij} n_j + \alpha_4 A_{ij} A_{ij} + (\alpha_5 + \alpha_6) n_i A_{ij} A_{jk} n_k + \gamma_1 N_i N_i, \quad (2-10)$$

$$\tilde{g}_i = -\gamma_1 N_i - \gamma_2 A_{ip} n_p, \quad (2-11)$$

$$N_i = \dot{n}_i - W_{ij} n_j, \quad (2-12)$$

$$\gamma_1 = \alpha_3 - \alpha_2, \quad \gamma_2 = \alpha_3 + \alpha_2, \quad (2-13)$$

$$A_{ij} = \frac{1}{2} (u_{i,j} + u_{j,i}), \quad (2-14)$$

$$W_{ij} = \frac{1}{2} (u_{i,j} - u_{j,i}). \quad (2-15)$$

The meaning and definition of each term in Eqs. (2-2) - (2-15) is identical to those reviewed in the section 1.2.2.

In this simulation, the modified linear momentum equation in Eq. (2-3) including the continuity equation in Eq. (2-2) and the modified angular momentum equation in Eq. (2-4) were fully coupled, and the gravitational force was neglected. Due to complexity of the E-L equations, two-dimensional numerical simulation was carried out. The geometry for the simulation is depicted in Fig. 2.7, which shows a side view of the optofluidic chip. The symmetric condition was applied at the channel center ($z = 12.5 \mu\text{m}$). The no slip condition was applied as the boundary condition for the velocity field (\tilde{u}) at the channel wall ($z = 0$). In order to determine the boundary condition for the director field (\tilde{n}), a microchannel was filled with 5CB, and was observed between the crossed polarizers by the microscope. Fig. 2.8 represents the director orientation at static state in a microchannel with a channel depth of $25 \mu\text{m}$. Both of Figs. 2.8a and 2.8b show the dark images in the biconvex-shaped expansion chamber. This result means that the homeotropic orientation ($\theta = 90^\circ$) was formed on the upper and bottom surfaces of microchannel. Therefore, $\theta = 90^\circ$ was applied as the boundary condition for the director field at $z = 0$ in Fig. 2.7, and it was assumed that such condition was maintained during flowing (*i.e.*, a strong anchoring condition was also applied here.).

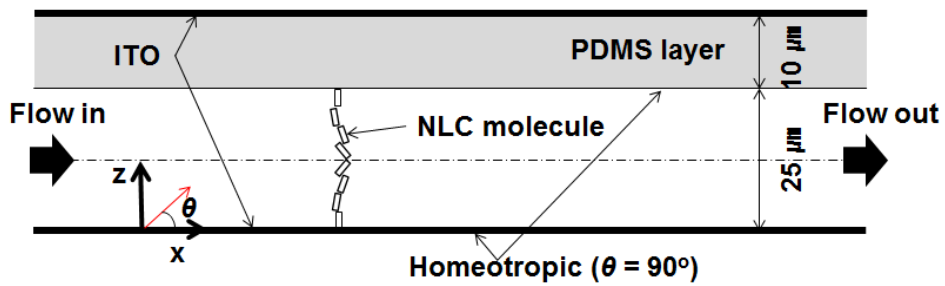


Figure 2.7 Geometry for the simulation of the flow-induced orientation of the director under a strong electric field.

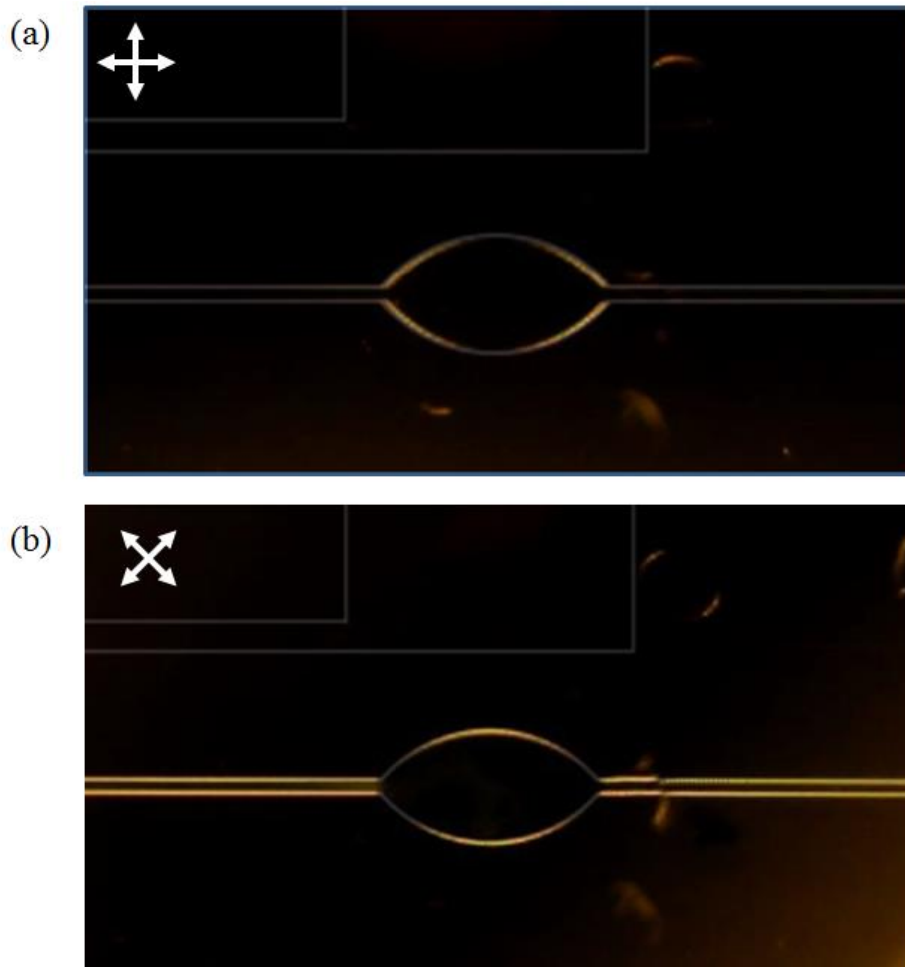


Figure 2.8 Microscopic images of the microchannels filled with 5CB at static state. The microchannels were positioned between the crossed polarizers with a rotation angle of (a) 0° and (b) 45° . The white arrows represent the transmission axes of the crossed polarizers.

2.3.2. Simulation of two-phase interfaces

For the three-dimensional simulation of the interfaces between the main stream and the sub-stream in the expansion chamber, it was assumed that the gravitational force was neglected, and a sufficiently strong electric field was applied to the NLCs, so that the directors were aligned in the direction of electric field during the flow of NLCs. Thus, \tilde{n} was equivalent to (0, 0, 1) at everywhere, and thereby gradient of the director ($n_{i,j}$) vanished. This means that the elastic free energy density (\hat{w}_F) in Eq. (2-6) is equal to zero, so that the term of $\tilde{g}_j n_{j,i}$ in Eq. (2-3) and the angular momentum equation in Eq. (2-4) can be neglected.^[19] Thus, the linear momentum equation of NLC governed by the strong electric field is written by

$$\rho \dot{u}_i = -\tilde{p}_i + \tilde{t}_{ij,j}, \quad (2-16)$$

The volume of fluid (VOF) method was used for the interface tracking. In this method, the fractional volume function (f) is defined as follows.^[20,21]

$$f(\tilde{x}, t) = \begin{cases} 1 & \text{for the region filled with the main fluid} \\ 0 & \text{for the region filled with the sub-fluid} \end{cases}. \quad (2-17)$$

f is governed by a scalar advection equation,^[21]

$$\frac{\partial f}{\partial t} + \tilde{u} \cdot \nabla f = 0. \quad (2-18)$$

If f is between 0 and 1, we define the critical fractional volume factor (f_c), and set f as follows.

$$f(\tilde{x}, t) = \begin{cases} 1 & \text{for } f \geq f_c \\ 0 & \text{for } f < f_c \end{cases}. \quad (2-19)$$

By using f , the density is linearly interpolated as below.

$$\rho = \rho_m f + \rho_s (1 - f), \quad (2-20)$$

where ρ_m and ρ_s are the densities of the main fluid and the sub-fluid, respectively. The linear momentum equations for the main fluid and the sub-fluid can be combined with help of f . Since the sub-fluid is governed by the Navier-Stokes (N-S) equation, the overall governing equation including the linear momentum equation of the modified E-L equation under the strong electric field in Eq. (2-16) can be given by

$$\rho \dot{u}_i = f(-\tilde{p}_i + \tilde{t}_{ij,j}) + (1 - f)(-p_i + \mu_s A_{ij,j}), \quad (2-21)$$

where μ_s is the Newtonian viscosity of the sub-fluid. The material properties for the simulation are presented in Table 2.1. The boundary conditions for \tilde{u} and \tilde{n} were adopted equivalently to those of the section 2.3.1.

Table 2.1 Material properties of the main fluid (5CB) and the sub-fluid (the mixture of 2,2,2-trifluoroethanol and cyclohexanol).

Material	Parameters	
5CB	Leslie viscosities ^[17] / Pa s	$\alpha_1=-0.0060, \alpha_2=-0.0812, \alpha_3=-0.0036,$ $\alpha_4=0.0652, \alpha_5=0.0640, \alpha_6=-0.0208,$
	Miesowicz viscosities ^[17] / Pa s	$\eta_1 = 0.0204, \eta_2 = 0.1052, \eta_3 = 0.0326$
	Frank elastic constants ^[17] / N	$K_1 = 6.2 \times 10^{-12}, K_2 = 3.9 \times 10^{-12},$ $K_3 = 8.2 \times 10^{-12}$
	Dielectric constants ^[17]	$\epsilon_{\parallel} = 18.5, \epsilon_{\perp} = 7, \epsilon_a = \epsilon_{\parallel} - \epsilon_{\perp} = 11.5$
	Density ^[17] / g cm ⁻³	1.02
	Refractive index	$n_{\parallel} = 1.7360, n_{\perp} = 1.5442$
Mixture of 2,2,2-trifluoroethanol and cyclohexanol	Density ^{a)} / g cm ⁻³	1.166
	Viscosity / Pa s	0.0047
	Refractive index ^{a)}	1.378

^{a)}calculated by the rule of mixture from the volume fraction of mixture.

2.4. Results and discussion

2.4.1. Dimensionless analysis for electric field dominant conditions

When the NLC flows in a microchannel under the electric field, three forces such as an elastic force, a viscous shear force, and an electric field force compete with each other. However the elastic force is neglected in this study because the directors keep the homeotropic orientation at static without the electric field as shown in Fig. 2.8. In other words, the directors are initially oriented along the same direction with the electric field in this study. This means that the elastic force don't disturb the electric field force here. Therefore, the viscous shear force and the electric force are mainly considered.

The dimensionless number for the estimation between the elastic force and the viscous shear force was already known as the Ericksen number (Er) in Eq. (1-26). To estimate a contribution between the viscous shear stress and the electric field force, a new dimensionless number ($E\nu$) is defined. In the modified linear momentum equation of E-L equations in Eq. (2-3), the terms related to the electric force and the viscous shear stress are $\Psi_{,i}$ and $\tilde{\tau}_{ij,j}$, respectively. Accordingly, the ratio of $\Psi_{,i}$ and $\tilde{\tau}_{ij,j}$ is given by the scaling analysis as follows.

$$E\nu \sim \frac{\text{Electric field force}}{\text{Viscous shear force}} \sim \frac{\nabla\Psi}{\mu\tilde{N}^2\tilde{u}} \sim \frac{\Psi/L}{\mu U/L^2} \sim \frac{\Psi L}{\mu U} \sim \frac{\varepsilon\left(\frac{V}{L}\right)^2 L}{\mu U} \sim \frac{\varepsilon V^2}{\mu UL}, \quad (2-22)$$

where $\tilde{\tau}_{ij,j}$ is expressed as the form of Newtonian fluid, so that μ is considered as the second Miesowicz viscosity (η_2) of 5CB representing a maximum viscosity listed in Table 3.1. In Eq. (2-22), U is the average velocity of NLC, and ε is the permittivity of NLC equal to $\varepsilon_o\varepsilon_r$. In NLCs, ε_r is an anisotropic value, so that it is considered as the average of $\varepsilon_{||}$ and ε_{\perp} . V is the applied voltage, and L is the characteristic length for rectangular channel given as $2ab / (a + b)$ where a and b correspond to the width and height of the microchannel, respectively.

As mentioned in Introduction, it is assumed that the directors are fixed along the direction of electric field perpendicular to the flow direction when the strong electric field is applied for the L^2 lens to act as a birefringent lens. For validation of this assumption, the numerical analyses according to Ev were carried out in the two-dimensional microchannel as explained in the section 2.3.1.

Fig 2.9 shows the simulation results for orientation angles of the directors subjected to the fixed voltage ($V = 5$ V) at various average velocities with COMSOL® 4.3. At high velocity, the directors are aligned in the flow direction as shown in Fig. 2.9a, but are vertically oriented along the direction of electric field as shown in Fig. 2.9f as the velocity decreased. These results are plotted in Fig. 2.10. At high velocity, the viscous shear force is dominant compared to the electric field force, so that Ev is low, and the directors are aligned toward flow direction. However, the directors are almost vertically oriented over at $Ev = 500$ as shown in Fig. 2.10b where the maximum tilt angle is only about 1 degrees. Fig. 2.11 exhibits the simulation results for orientation angles of the directors at constant velocity ($U = 100 \mu\text{m s}^{-1}$) under various applied voltages. Similarly, the directors rotate along the flow direction at low applied voltage as shown in Fig. 2.11a, but are aligned perpendicular to the flow direction as shown in Fig. 2.11f as increasing the applied voltage. Fig. 2.12 shows plots for the orientation angle of the directors at same conditions with Fig. 2.11. At low applied voltage corresponding to low Ev , the viscous shear force is stronger than the electric field force, so that the orientation of directors is tilted to the flow direction. However, the tilted angles of directors are below 2 degrees over at $Ev = 500$ as shown in Fig. 2.12b in common with the results in Fig. 2.10b.

The effective refractive index (n_{eff}) in the NLC medium at the s-mode varies with the orientation angle (θ) of director. It can be calculated as follows.

$$n_{eff} = \frac{n_{\perp} n_{\parallel}}{\sqrt{n_{\parallel}^2 \cos^2 \theta + n_{\perp}^2 \sin^2 \theta}}. \quad (2-23)$$

Using Eq. (2-23) and the orientation angles obtained at Figs. (2-10) and (2-12), the effective refractive indices were calculated, and they were converted to the normalized effective refractive indices (N_{eff}) defined by

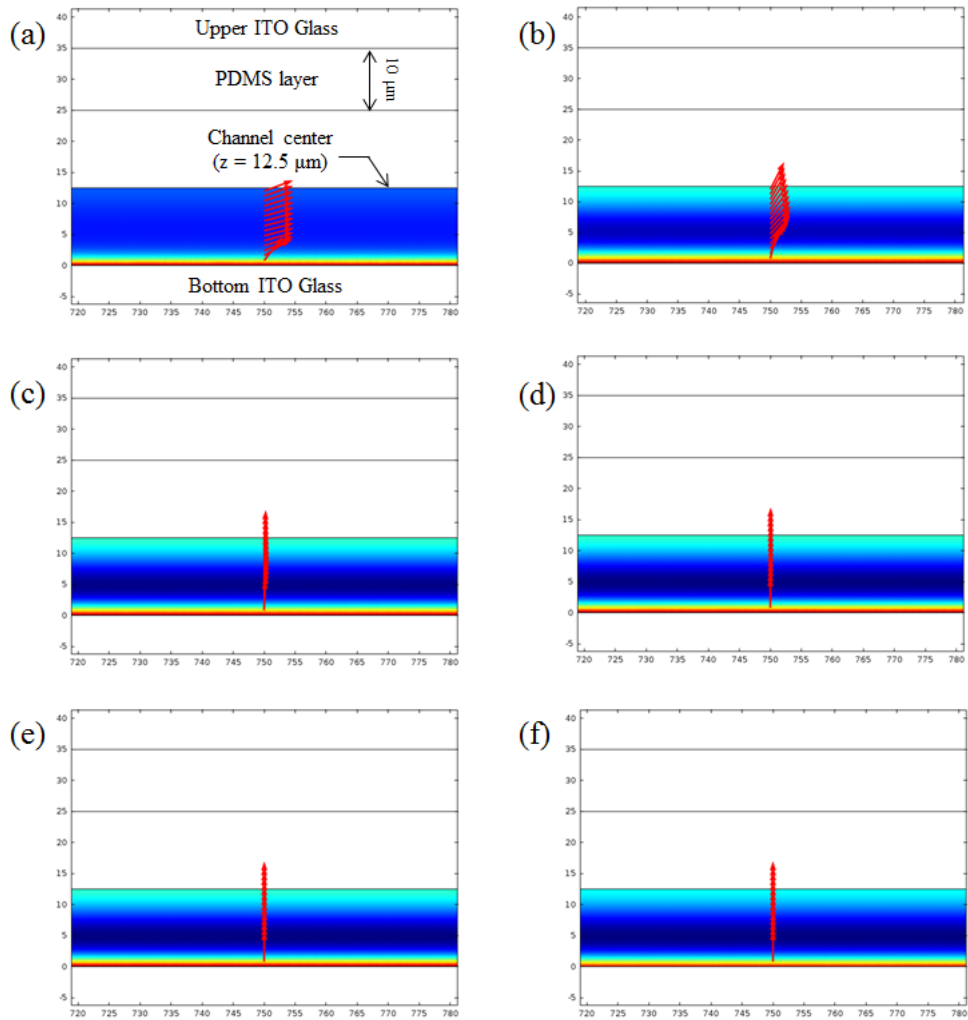


Figure 2.9 Orientation angles of the directors at $U =$ (a) 604, (b) 60.4, (c) 6.04, (d) 1.21, (e) 0.604, and (f) 0.121 $\mu\text{m s}^{-1}$, respectively. The applied voltage was fixed at 5 V. The flow direction of NLC was from left to right.

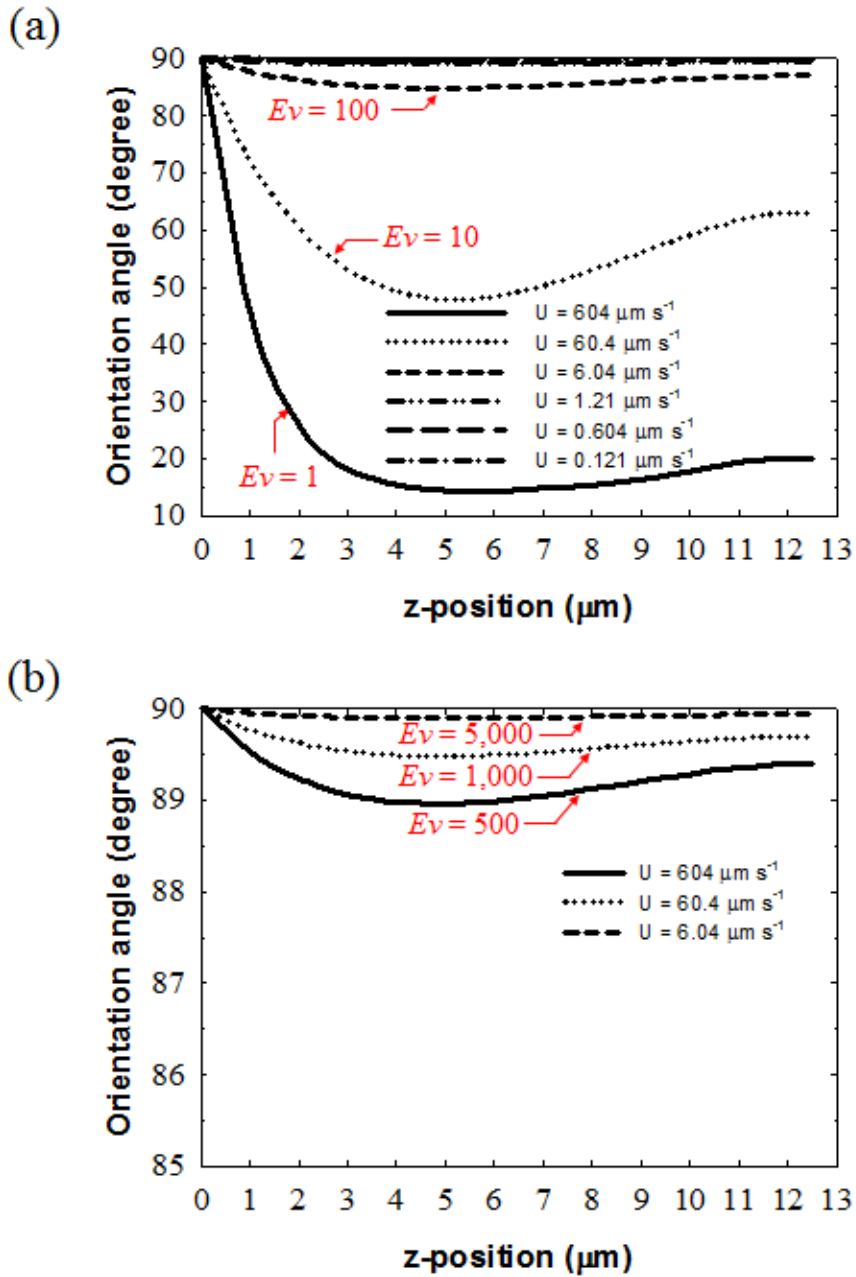


Figure 2.10 Orientation angles of the directors at various average velocities and the fixed voltage ($V = 5$ V) plotted in the range of (a) 10 - 90 degrees and (b) 85 - 90 degrees. The values of Ev are denoted at each corresponding line.

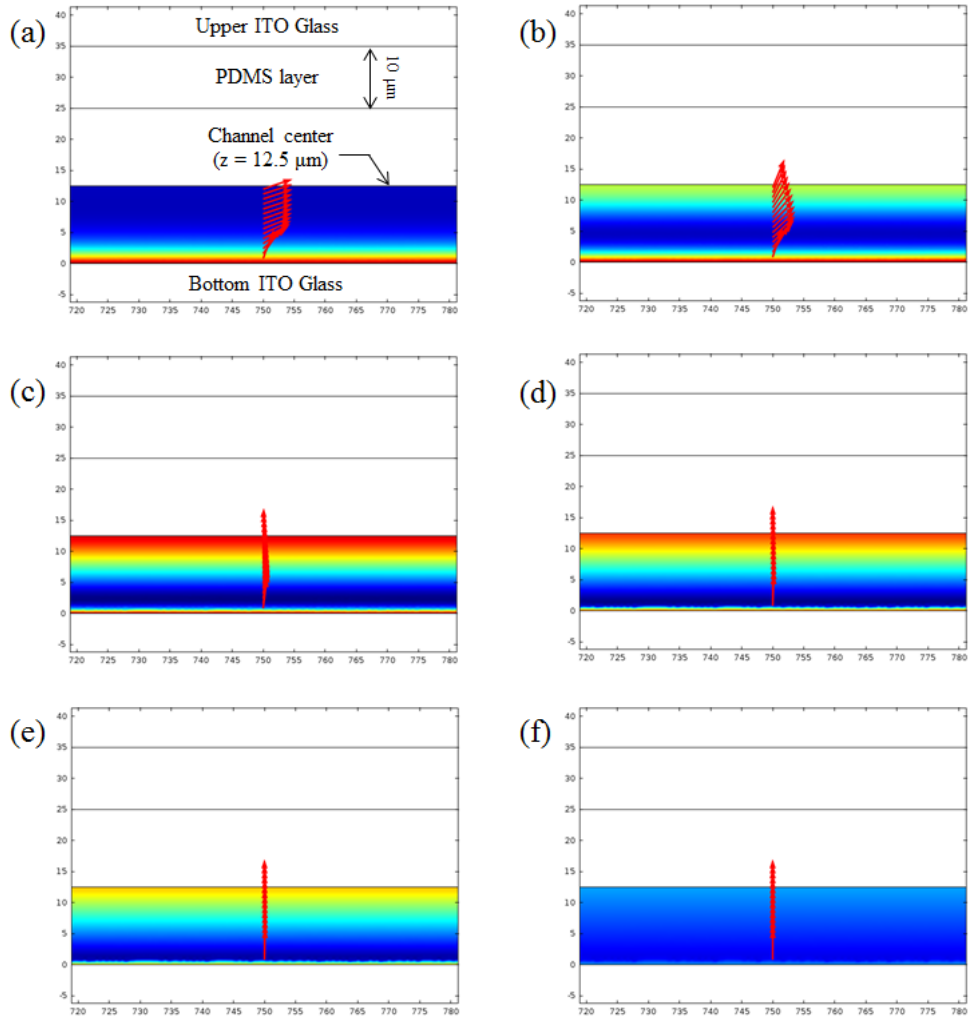


Figure 2.11 Orientation angles of the directors under $V =$ (a) 2.0, (b) 6.4, (c) 20.4, (d) 45.5, (e) 64.6, and (f) 143.9 V, respectively. The average velocity (U) was fixed at $100 \mu\text{m s}^{-1}$. The flow direction of NLC was from left to right.

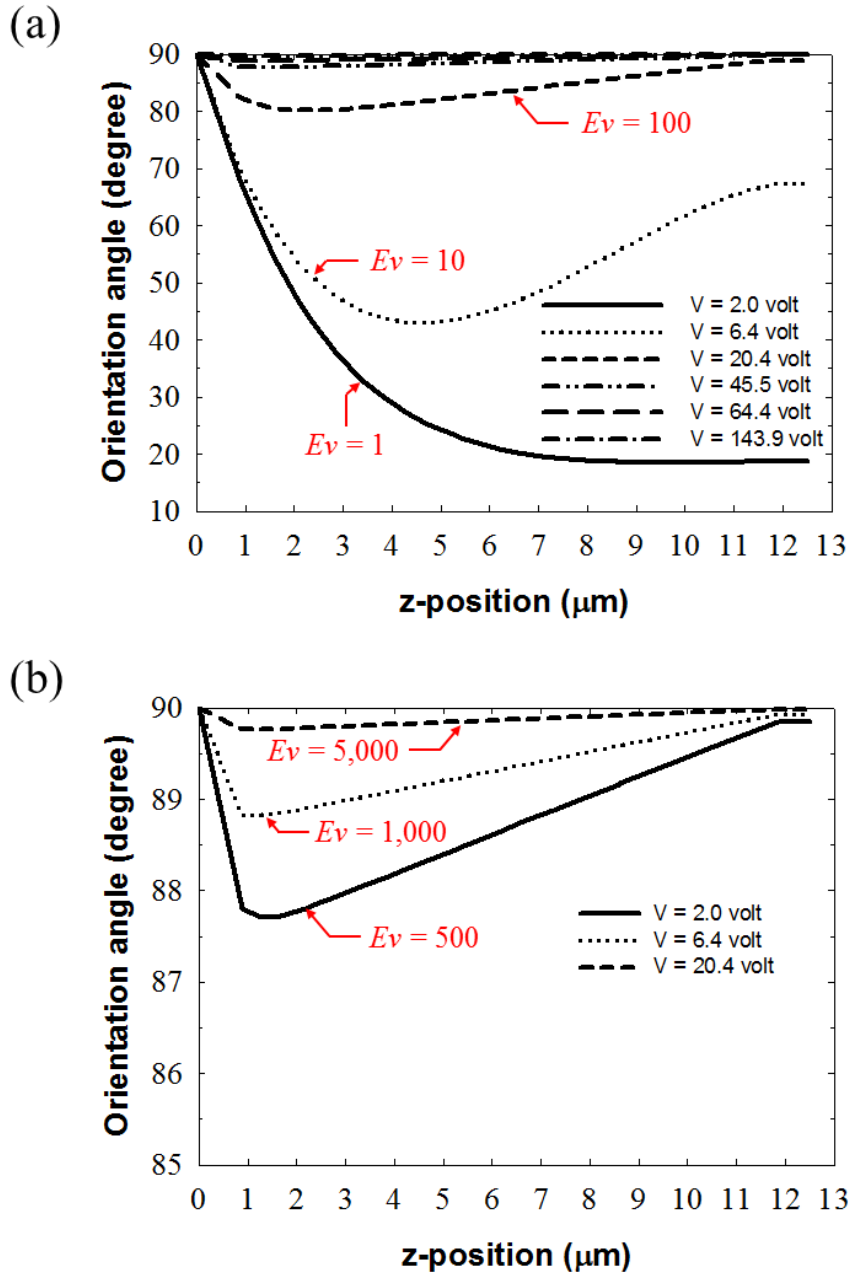


Figure 2.12 Orientation angles of the directors at various applied voltages and constant velocity ($U = 100 \mu\text{m s}^{-1}$) plotted in the range of (a) 10 - 90 degrees and (b) 85 - 90 degrees. The values of Ev are denoted at each corresponding line.

$$N_{eff} = 1 - \frac{n_{||} - n_{eff}}{n_{||} - n_{\perp}}. \quad (2-24)$$

Therefore, n_{eff} is equal to $n_{||}$ if $N_{eff} = 1$, and is equal to n_{\perp} if $N_{eff} = 0$. In this study, $N_{eff} = 1$ ($n_{eff} = n_{||}$) is desirable at the s-mode. Fig. 2.13 and 2.14 show the normalized effective refractive indices at various average velocities and different applied voltages, respectively. Both of them exhibit N_{eff} is almost unity over at $Ev = 100$. In particular, deviations between n_{eff} and $n_{||}$ are within 0.2 % over at $Ev = 500$. At this time, the directors can be regarded as being perfectly oriented to the direction of electric field. As a result, it is concluded that $Ev > 500$ ensures the vertical orientation of the directors along the electric field in the microchannel.

2.4.2. Validation of experimental conditions

In the previous section, we found that the directors were oriented parallel to the direction of electric field at $Ev > 500$. At this condition, the angular momentum equation in Eq. (2-4) can be neglected as mentioned in the section 2.3.2. Before carrying out main experiments, we determined the applied pressure for the main stream and the applied voltage satisfying $Ev > 500$. As a result, it was found that stable interfaces were formed in the expansion chamber when the applied pressure for the sub-channel (P_s) was fixed at 7 kPa, and the pressure for the main channel (P_m) varied from 11 to 14 kPa under an external electric field of 150 V (50 kHz). In addition, the average velocity corresponding to each applied pressure for the main fluid was measured by checking inflow volumes.

Fig. 2.15a shows the average velocity and Ev at each applied pressure under the electric field of 150 V (50 kHz). From this graph, it is concluded that the directors can be aligned parallel to the direction of electric field at $P_m = 11 - 14$ kPa, $P_s = 7$ kPa, and $V = 150$ V due to $Ev > 500$. Fig. 2.15b represents that the ratio of the average velocities between the main stream and the sub-stream linearly increases as the pressure for the main stream increases. Therefore, it is expected that the size of L^2 lens also will increase linearly.

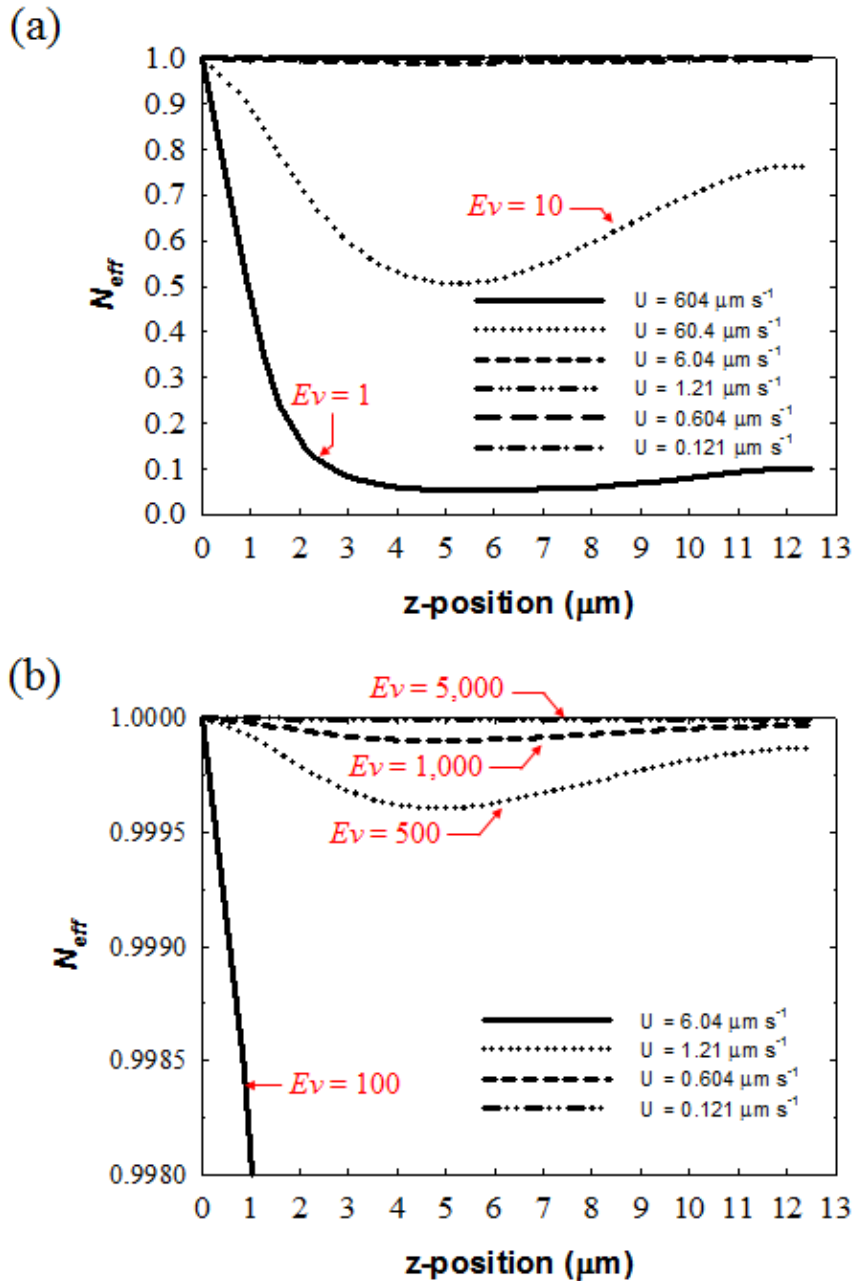


Figure 2.13 Normalized refractive indices at various average velocities and the fixed voltage ($V = 5$ V) plotted in the range of (a) 0.0 – 1.0 and (b) 0.9980 – 1.0000.

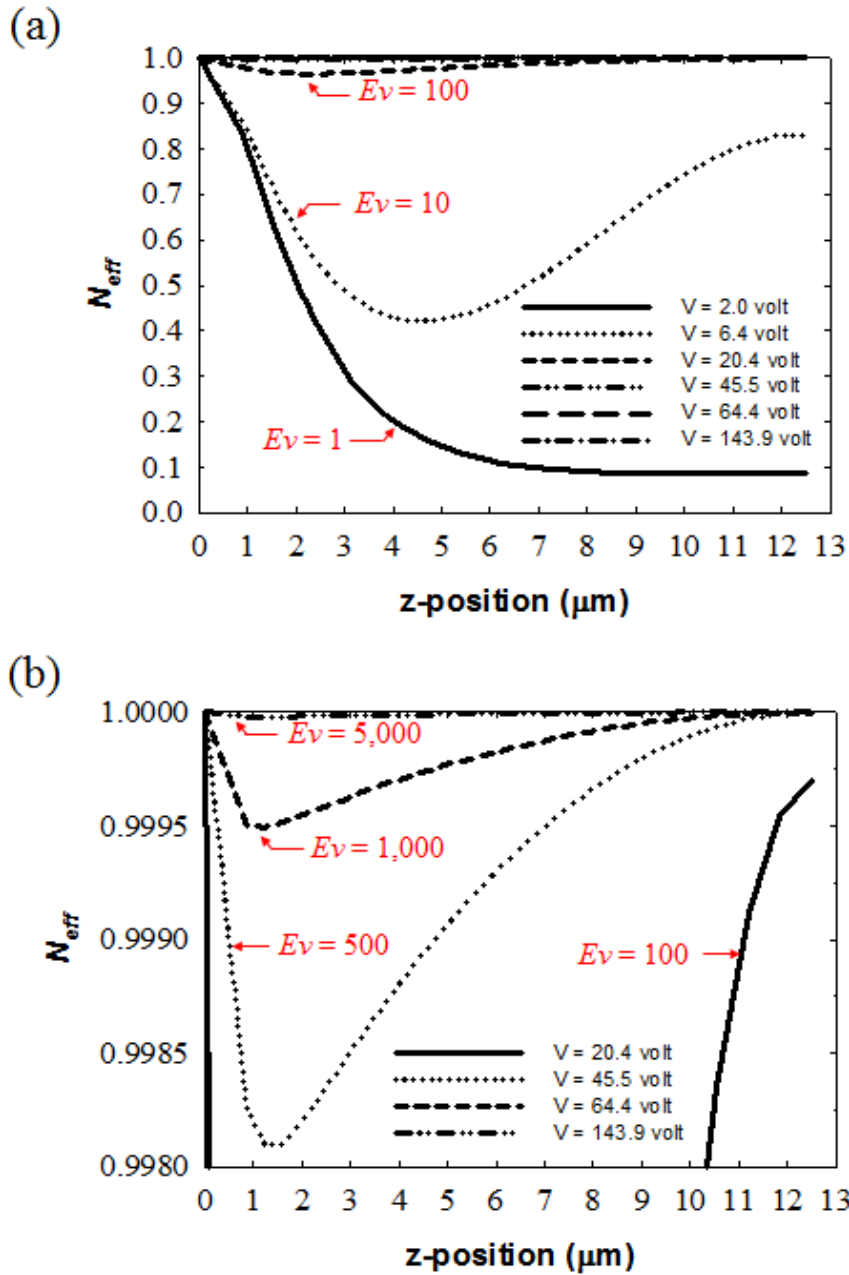


Figure 2.14 Normalized refractive indices at various applied voltages and constant velocity ($U = 100 \mu\text{m s}^{-1}$) plotted in the range of (a) 0.0 – 1.0 and (b) 0.9980 – 1.0000.

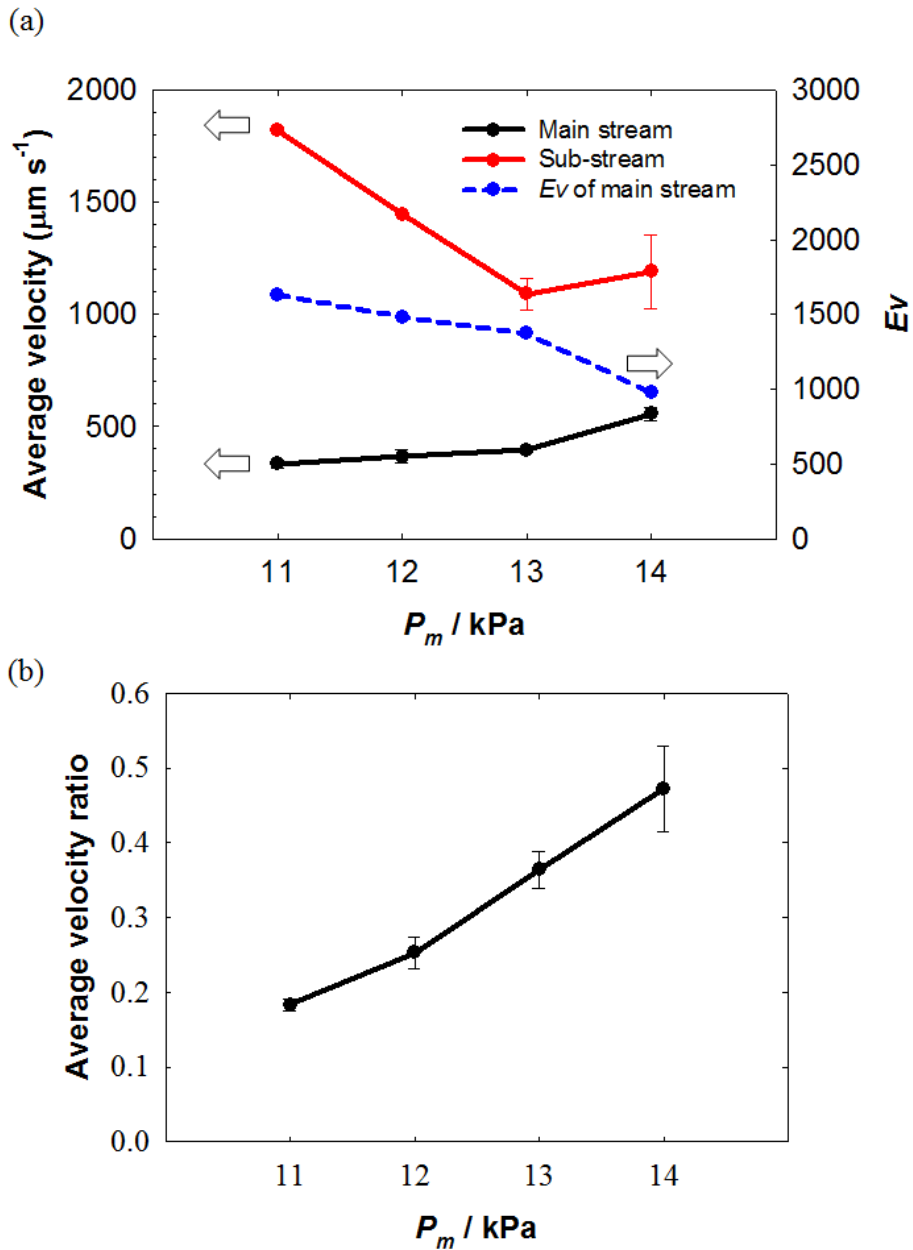


Figure 2.15 (a) Average velocity and $E\nu$, and (b) average velocity ratio of the main flow and sub-flow according to pressure for the main stream when the strong electric field (150 V, 50 kHz) was applied. The applied pressure for the sub-stream was fixed at 7 kPa.

2.4.3. NLC orientation and L^2 interface

Using the conditions for experiments determined in the previous section ($P_s = 7$ kPa, $P_m = 11 - 14$ kPa, and 150 V with 50 kHz), the NLC orientation was observed in the expansion chamber when the optofluidic chip was located between the crossed linear polarizers as shown in Fig. 2.16a. The uniform dark images obtained with rotation angles of 0° (Fig. 2.16a (i)) and 45° (Fig. 2.16a (ii)) between the crossed polarizers indicate that the directors were oriented perpendicular to the flow direction as expected. In addition, the stable L^2 interfaces were formed in the expansion chamber as shown in Fig. 2.16a (iii). As P_m increased, the NLC phases expanded, and the interface curvatures increased. In this case, it was expected that the NLCs had a high viscosity similar to the second Miesowicz viscosity ($\eta_2 = 105.2$ mPa s),^[17] because the director orientations in the microchannel were orthogonal to the flow direction and parallel to the velocity gradient ($\nabla \tilde{u}$).

Fig. 2.16b shows the L^2 interfaces and the NLC orientations obtained without applying the electric field. From the partially dark (Fig. 2.16b (iv)) and bright (Fig. 2.16b (v)) images of the lens, it is inferred that the NLCs were aligned mainly along the flow direction. Also, the applied pressures for the main stream were lower than those under the electric field. Because the directors were oriented in the flow direction, the viscosity of the main fluid was similar to the first Miesowicz viscosity ($\eta_1 = 20.4$ mPa s).^[17] Such decrease in the viscosity led to lowering P_m compared with those under the electric field.

2.4.4. Ray path

When the polarized light was irradiated through the optofluidic chip, the light was focused by the L^2 interface. Fig. 2.17 shows the fluorescent images of the ray-tracing chamber. When the electric field was not applied to the device, a significant difference in the focal lengths was not observed according to the polarization mode of the incident light even under different pressures as shown in Fig. 2.17a. In addition, the focal points were not clear because of the non-uniform orientation of the directors as observed in Fig. 2.16b. This means that the effective refractive

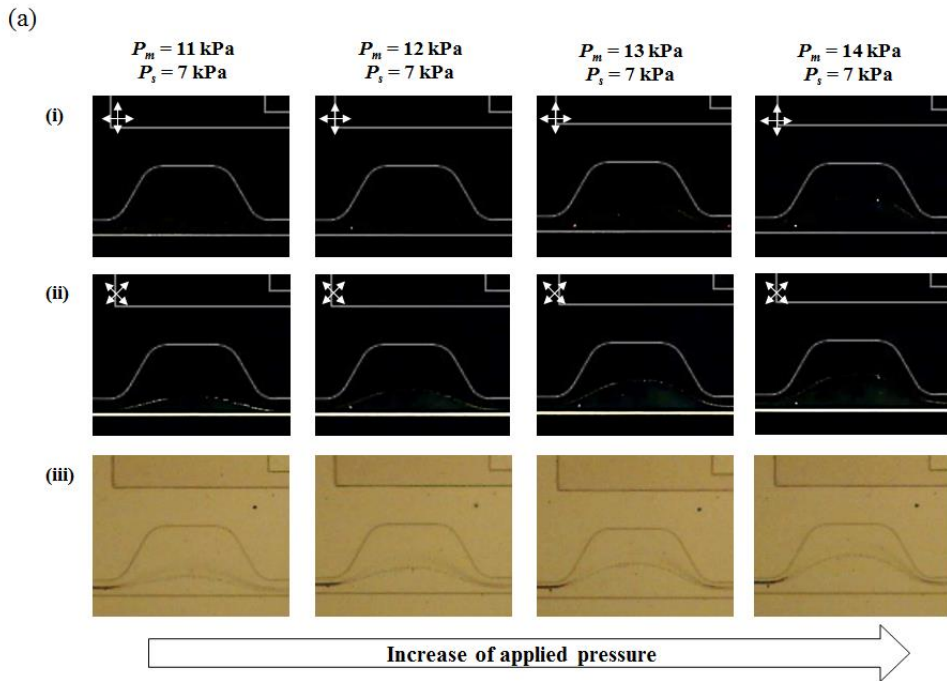


Figure 2.16 Microscopic images of the expansion chambers (a) with and (b) without the electric field. The optofluidic chip was positioned between the crossed polarizers: (i) and (iv) with an angle of 0° and (ii) and (v) with an angle of 45° . (iii) and (iv) were unfiltered images. The white arrows represent the transmission axis of each polarizer. The denoted pressure values were applied for the main stream and the sub-stream (P_m and P_s , respectively).

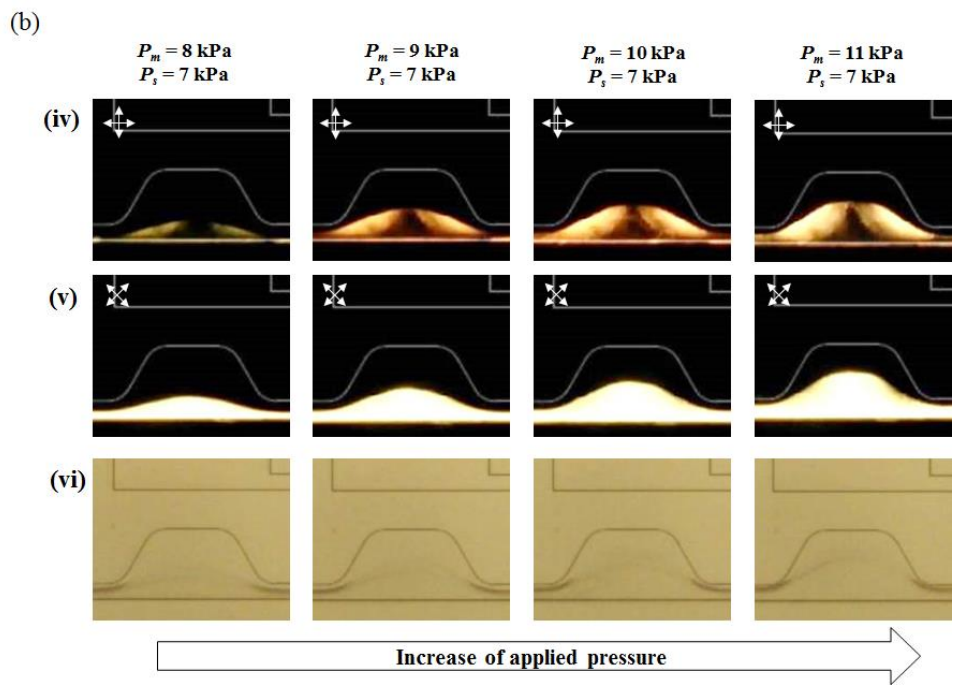


Figure 2.16 (continued)

indices (n_{eff}) in the p- and s-mode are similar because the orientation of directors continuously varies at from the surface ($z = 0$) to the center of the microchannel ($z = 12.5 \mu\text{m}$) as shown in Fig. 2.9a or 2.11a, so that the NLC phase act as an isotropic medium.

On the other hand, birefringent phenomena were obviously observed when the electric field (150 V, 50 kHz) was applied to the optofluidic chip as shown in Fig. 2.17b. The homeotropic orientations of NLCs ($\theta = 90^\circ$) were induced by the strong electric field. Therefore they yielded a large distinction of refractive indices between n_{eff} ($= n_{||}$) for the main stream and n_i for the sub-stream at the s-mode. In the p-mode, n_{eff} for the main stream is equal to n_{\perp} as mentioned in Introduction. Thus, the contrast of refractive indices ($n_{eff} - n_i$) at the s-mode is larger than that at the p-mode. As a result, the shorter focal lengths could be observed in the s-mode than in the p-mode. Also, the focal length decreased with increasing P_m due to increase of the L^2 interface curvature, which will be quantitatively analysed in the next section.

2.4.5. Comparison between numerical and experimental results

The L^2 interfaces under the strong electric field in Fig. 2.16a (iii) were too unclear to be compared with the simulation results. For precise comparison, more distinguishable L^2 interfaces could be observed through an indirect irradiation of laser with a wavelength of 532 nm using a light scattering feature of NLCs.^[22] Fig. 2.18 shows the L^2 interfaces re-measured using the light scattering under the strong electric field.

From Fig. 2.16a, we observed that the homeotropic orientation of the directors was maintained under the strong electric field while gradually increasing the pressure. Therefore, we can set $\tilde{n} = (0, 0, 1)$. This assumption enables us to neglect the angular momentum equation during carrying out the simulation as mentioned in the section 2.3.2. By using Eq. (2-21) as the governing equation, the L^2 interfaces under the strong electric field were simulated with COMSOL[®] 4.3 according to the values of f_c in Eq. (2-19). Fig. 2.19 shows the simulation results of

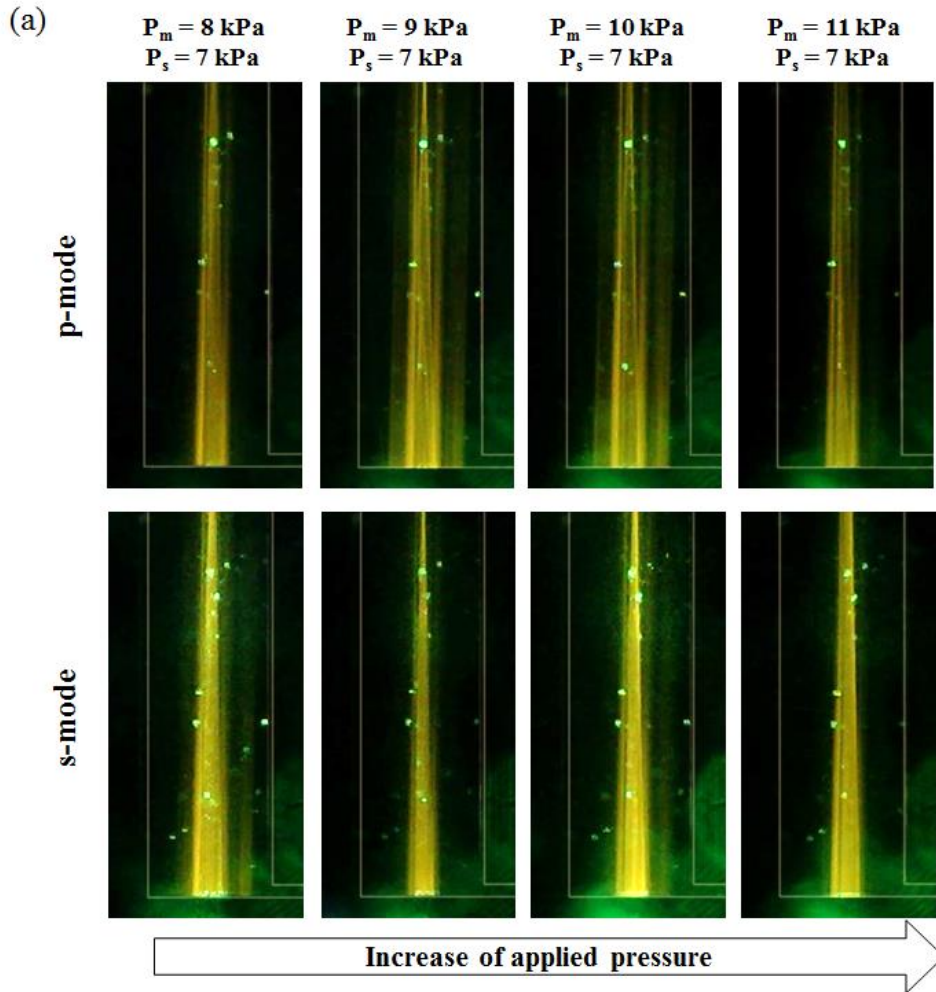


Figure 2.17 Fluorescent images exhibiting ray paths in the ray-tracing chamber (a) without and (b) with the electric fields. The upper and lower rows indicate p- and s-mode which imply the incidence of the p-polarized and s-polarized light, respectively.

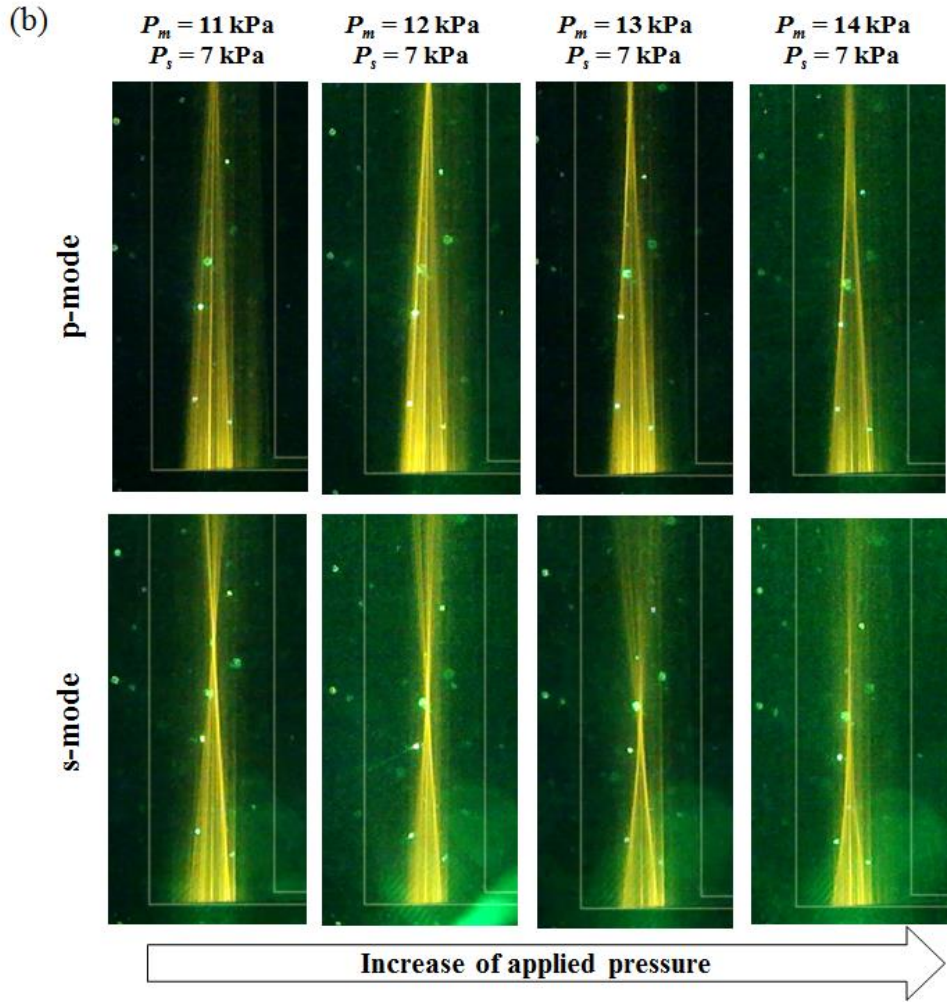


Figure 2.17 (continued)

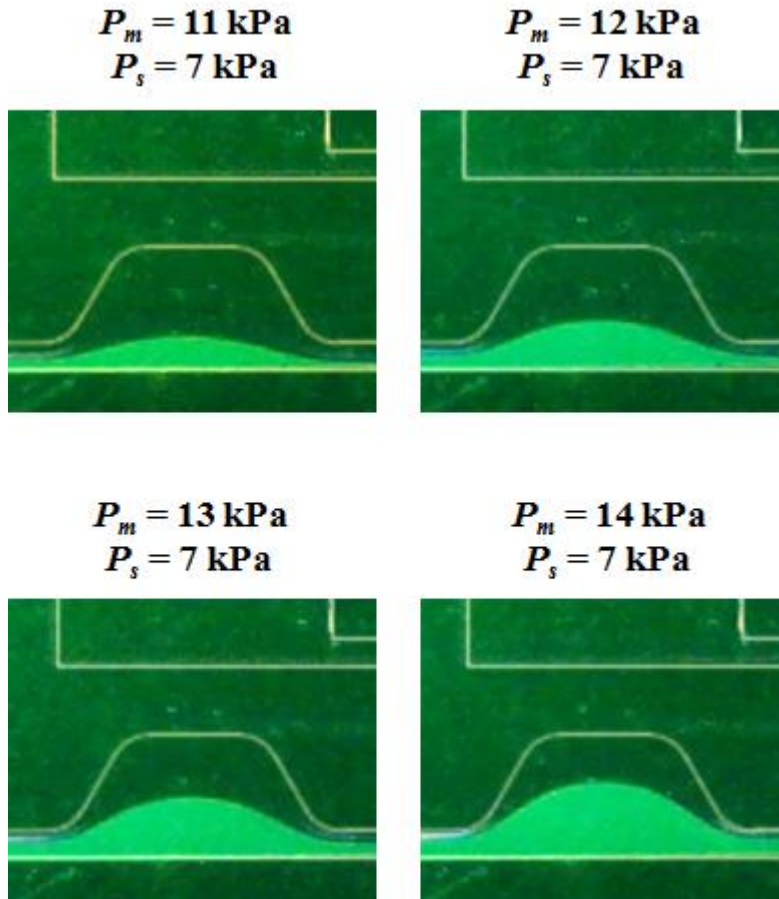


Figure 2.18 L^2 interfaces under the strong electric field observed by the light scattering.

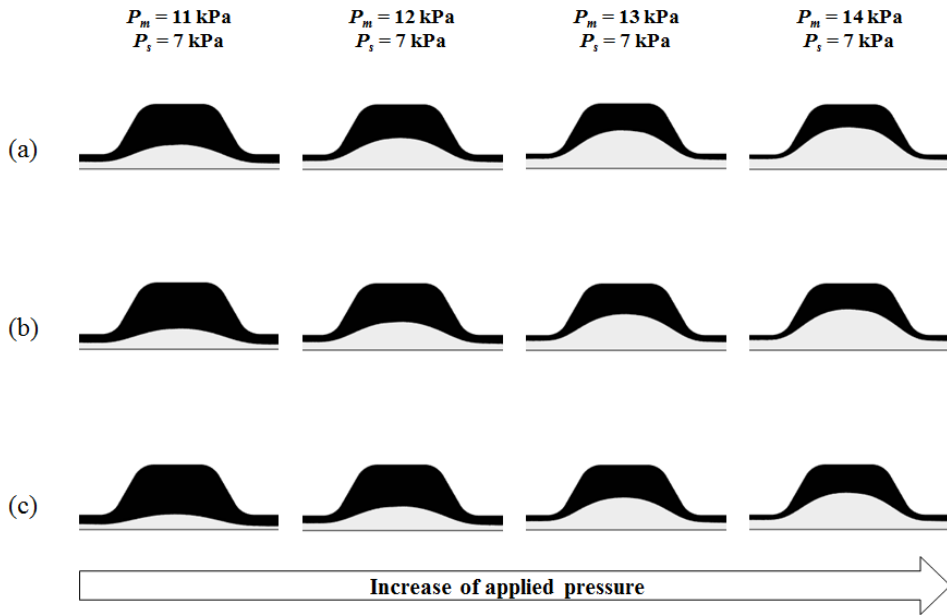


Figure 2.19 Simulation results of the L^2 interfaces under the strong electric field at $f_c =$ (a) 0.5, (b) 0.6, and (c) 0.7.

the L^2 interfaces. For comparison, the images in Fig. 2.19 were overlaid on the experimentally observed images (Fig. 2.18). Fig. 2.20 represents the comparison between the simulation and the experimental results. At $f_c = 0.6$, the simulation results are in good agreement with the experimental results.

For a quantitative comparison, the curvature and the lens thickness (t_L), which was a thickness at the edge of aperture as shown in Fig. 2.21, extracted from the simulation results were compared with those of the experimental results as shown in Fig. 2.22. The radiuses of curvature of the simulation results were obtained by fitting circles to the L^2 interfaces.^[10] The curvature had a maximum value at $P_m = 13$ kPa and decreased at $P_m = 14$ kPa because the interface approached the wall of the expansion chamber.^[10] However, the lens thickness (t_L) linearly increases with increasing P_m as expected in the result of average velocity ratio in Fig. 2.15b.

From the simulation results regarding the curvature and the lens thickness, we calculated the focal lengths using a ray-tracing code based on MATLAB[®]. Tang *et al.*^[10] reported that the effect of the lens thickness on the focal length was insignificant. In this study, the lens thickness was, however, considered in the calculation of the focal lengths because the lens thickness was comparable to the focal length (about 10 % of the focal length). The results of the ray-tracing were depicted in Fig. 2.23. Fig. 2.24 shows the comparison between the simulation and the experimental results for the focal length in the s-mode. The overall tendencies of the simulation and the experimental results are similar, but the focal lengths of the experimental results are lower than those of the simulation results below at $P_m = 13$ kPa. This difference might be caused by the diffusion region near the L^2 interfaces as shown in Fig. 2.16a (iii). In the diffusion region, the refractive index is continuously changed, which offers a possibility for the graded refractive index (GRIN) lens.^[13]

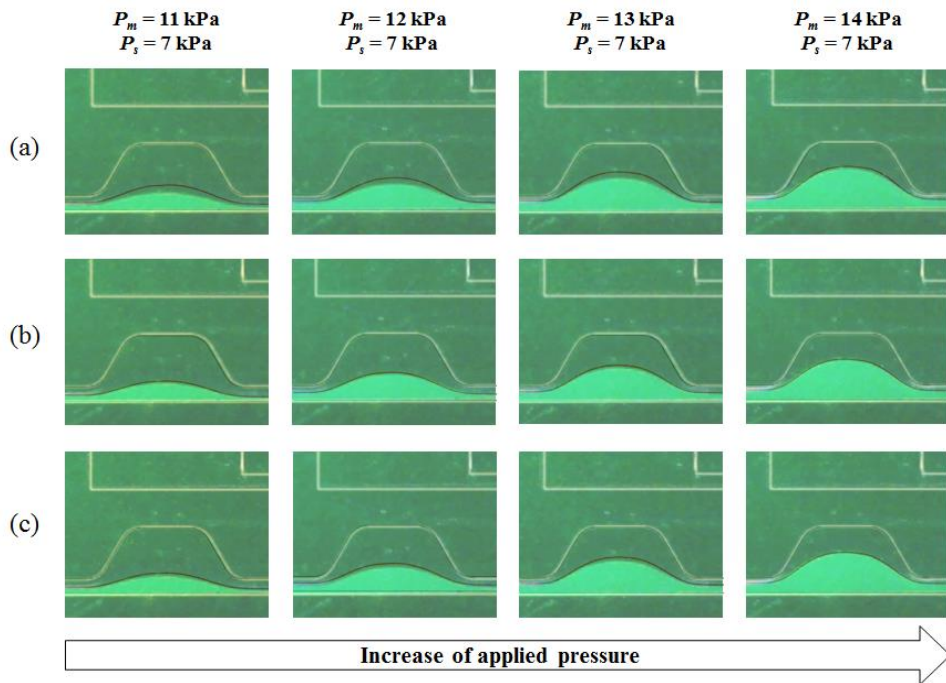


Figure 2.20 Comparison of the L^2 interfaces between the simulation and the experimental results at $f_c =$ (a) 0.5, (b) 0.6, and (c) 0.7. Red lines represent the L^2 interfaces confirmed from the simulation results.

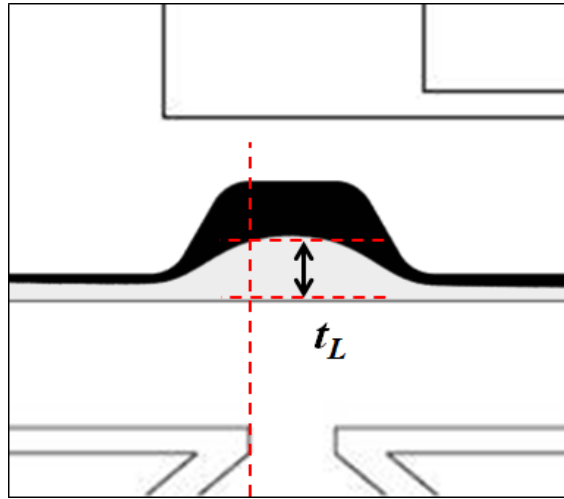


Figure 2.21 Illustration for the definition of the lens thickness (t_L) which indicates the thickness of the main stream at the edge of aperture.

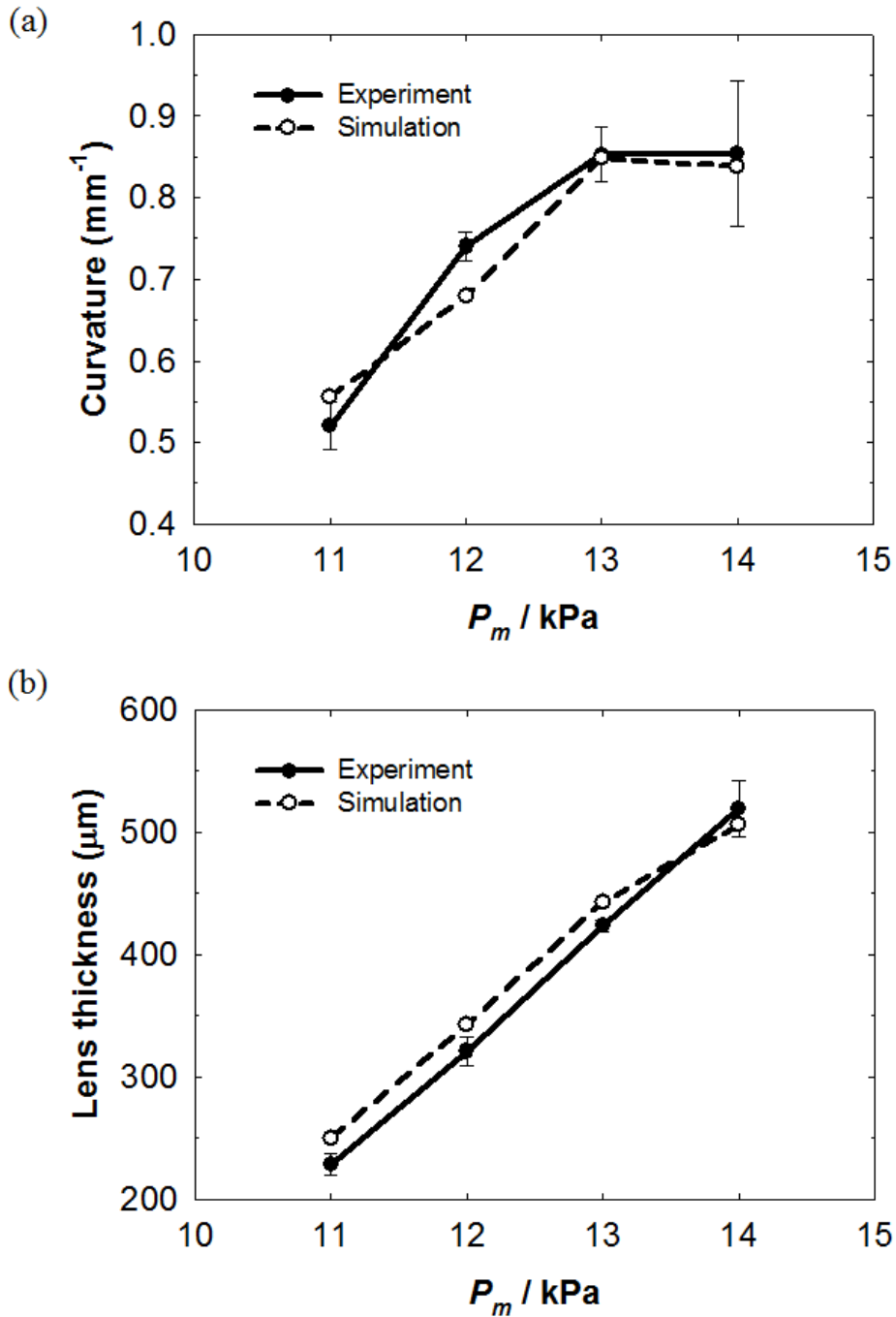


Figure 2.22 Comparison between the experimental and the simulation results: (a) curvature and (b) lens thickness.

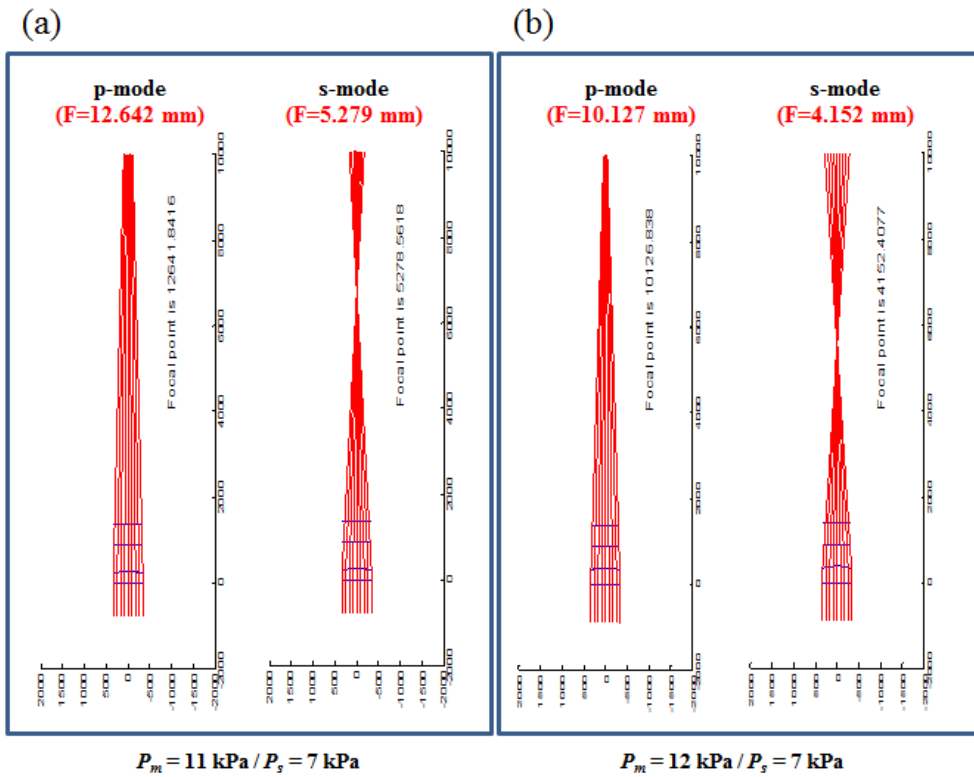


Figure 2.23 Focal length (F) calculated by using MATLAB at (a) $P_m = 11$ kPa / $P_s = 7$ kPa, (b) $P_m = 12$ kPa / $P_s = 7$ kPa, (c) $P_m = 13$ kPa / $P_s = 7$ kPa, and (d) $P_m = 14$ kPa / $P_s = 7$ kPa.

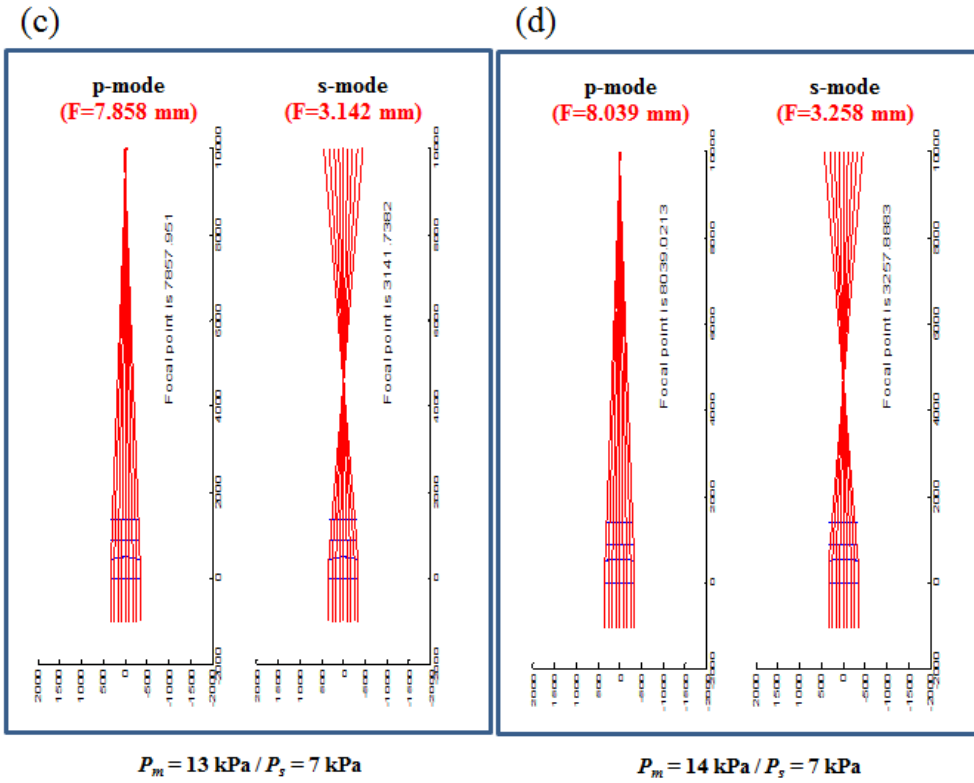


Figure 2.23 (continued)

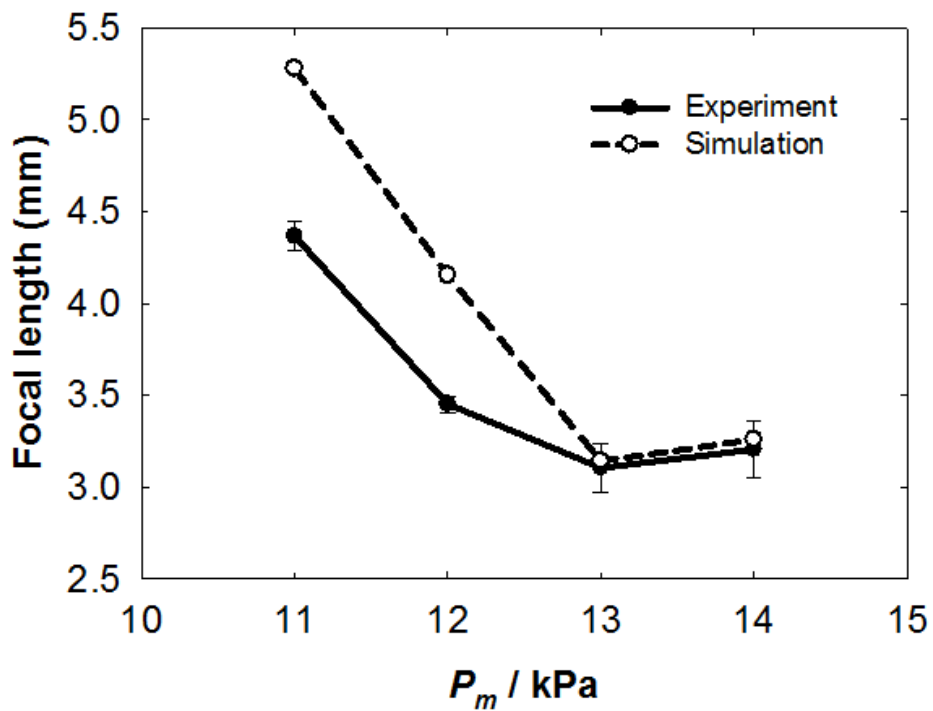


Figure 2.24 Comparison between the experimental and the simulation results for focal lengths in s-mode according to the applied pressure of the main stream (P_m).

2.5. Summary

The optofluidic birefringent L^2 lens was demonstrated in this study. The focal length of the lens was controlled by manipulating the L^2 interface hydrodynamically or changing the polarization of incident light with help of the field-induced orientation of NLCs. In addition, an efficient and powerful simulation platform for the L^2 interfaces and the focal lengths was provided. We anticipate that the optofluidic chip introduced in this study could be readily modified and employed in other applications. For example, a wider tunable focal length can be achieved by using three streams: one core flow and two sheath flows. Also, the birefringent optofluidic chip can provide characteristics of a conventional isotropic lens by heating NLCs because NLCs show isotropic properties over a nematic-to-isotropic transition temperature (T_{NI}). T_{NI} of 5CB used in this study is known to be about 35 °C.^[23] The thermal energy for the phase transition of NLCs can be simply supplied by using Joule heating, *i.e.*, by applying a DC voltage to the bottom ITO glass of the optofluidic chip. We expect that the optofluidic birefringent L^2 lens could be applied to various integrated microfluidic systems such as optical tweezer for capturing nano-sized particles, microlens array for three dimensional autostereoscopic displays, and so on.

2.6. References

- [1] V. R. Horowitz, D. D. Awschalom, S. Pennathur, *Lab. Chip*, 2008, 8, 1856-1863.
- [2] D. Psaltis, S. R. Quake, C. Yang, *Nature*, 2006, 442, 381-386.
- [3] D. Erickson, D. Sinton, D. Psaltis, *Nat. Photonics*, 2011, 5, 583-590.
- [4] B. Helbo, A. Kristensen, A. Menon, *J. Micromech. Microeng.*, 2003, 13, 307-311.
- [5] S. Mandal, D. Erickson, *Opt. Express*, 2008, 16, 1623-1631.
- [6] C. L. Smith, U. Bog, S. Tomljenovic-Hanic, M. W. Lee, D. K. Wu, L. O'Faolain, C. Monat, C. Grillet, T. F. Krauss, C. Karnutsch, *Opt. Express*, 2008, 16, 15887-15896.
- [7] P. Measor, B. S. Phillips, A. Chen, A. R. Hawkins, H. Schmidt, *Lab. Chip*, 2011, 11, 899-904.
- [8] Y. Fainman, L. Lee, D. Psaltis, C. Yang, *Optofluidics: fundamentals, devices, and applications*, McGraw-Hill, Inc., 2009.
- [9] C. Song, N.-T. Nguyen, S.-H. Tan, A. K. Asundi, *J. Micromech. Microeng.*, 2009, 19, 085012.
- [10] S. K. Tang, C. A. Stan, G. M. Whitesides, *Lab. Chip*, 2008, 8, 395-401.
- [11] K.-S. Chao, M.-S. Lin, R.-J. Yang, *Lab. Chip*, 2013, 13, 3886-3892.
- [12] X. Mao, J. R. Waldeisen, B. K. Juluri, T. J. Huang, *Lab. Chip*, 2007, 7, 1303-1308.
- [13] X. Mao, S.-C. S. Lin, M. I. Lapsley, J. Shi, B. K. Juluri, T. J. Huang, *Lab. Chip*, 2009, 9, 2050-2058.
- [14] J. L. Ericksen, *T. Soc. Rheol.*, 1961, 5, 23-34.
- [15] F. M. Leslie, *Arch. Ration. Mech. An.*, 1968, 28, 265-283.
- [16] F. M. Leslie, *Continuum Mech. Therm.*, 1992, 4, 167-175.
- [17] I. W. Stewart, *The static and dynamic continuum theory of liquid crystals: a mathematical introduction*, Crc Press, 2004.
- [18] C. J. Murphy, N. L. Abbott, Y.-Y. Luk, S. F. Campbell, L.-L. Cheng, C.-H. Jang (Wisconsin Alumni Research Foundation), *US 7951577 B2*, 2011.
- [19] P. A. Cruz, M. F. Tomé, I. W. Stewart, S. McKee, *J. Non-Newton. Fluid.*, 2010, 165, 143-157.

- [20] C. W. Hirt, B. D. Nichols, *J. Comput. Phys.*, 1981, 39, 201-225.
- [21] D. Seo, *Doctoral thesis*, Seoul National University, June, 2004.
- [22] F. Leslie, C. Waters, *Mol. Cryst. Liq. Cryst.*, 1985, 123, 101-117.
- [23] S. He, W. Liang, K.-L. Cheng, J. Fang, S.-T. Wu, *Soft matter*, 2014, 10, 4609-4614.

III. Thermo-sensitive Smart Film

3.1. Introduction

Liquid crystal (LC) embedded polymer films, commonly referred to as polymer dispersed liquid crystals (PDLCs), comprise a continuous polymer matrix and a number of micrometer-sized LC droplets. In general, PDLCs are positioned between two transparent electrodes, and an electric field is used to change the extent of light scattering as a result of a mismatch of refractive indices at the LC droplet boundary.^[1] PDLCs are widely investigated for various applications, such as smart windows, tunable filters, holographic devices, and displays.^[2-5] In addition, it has been studied for applications using thermo-induced changes such as a transmittance bistability at the phase transition temperature (T_{tr}) of LCs.^[6-8] For instance, a PDLC displaying multicolor was introduced by utilizing diffraction properties and wavelength dispersions of the refractive indices in response to temperature.^[9]

PDLCs have been prepared through a phase separation between LCs and polymers (or monomers). There are three different mechanisms for the phase separation of PDLCs: thermal-induced phase separation (TIPS), solvent-induced phase separation (SIPS), and polymerization-induced phase separation (PIPS). In the TIPS, a LC is mixed with a polymer over its melting temperature, and the mixture cools down under the melting temperature with a specific cooling rate. During the progress of solidification, LC domains are formed, and extended until the glass transition temperature of the polymer is achieved. It is known that a LC droplet size is affected by the cooling rate, viscosities and chemical potentials of the LC and the polymer, etc.^[10] In the SIPS, LC domains are separated by evaporating a solvent in which a LC and a polymer are dissolved. The evaporating rate of the solvent is important to decide the droplet size, which decreases as the evaporating rate increases.^[10] The PIPS is useful when a LC and a monomer can be mixed homogeneously. During the polymerization, the solubility of LC in the solidified polymer decreases, and the LC domains are formed until the polymerization is finished. The droplet size and the morphology are determined by

the polymerization rate, the curing temperature, and other factors such as a viscosity of solution, a rate of diffusion, and a solubility of the LC.^[11]

The conventional PDLC film driven by the electric field has several problems such as a high driving voltage, a limitation for enhancement of contrast, and a requirement for highly conductive electrodes as mentioned in Part I. Therefore, we present a novel thermo-sensitive smart film (TSF) that includes a PDLC layer on a silver nanowire (AgNW) coated film to overcome the problems of conventional PDLC film. The optical transmittance of the film is adjusted using the phase transition of PDLCs by thermal energy. AgNWs, a promising material for replacing indium tin oxide (ITO) used as a transparent electrode,^[12] show a low sheet resistance and a high transmittance with a low processing cost.^[13-15] Recently, Khaligh *et al.* reported PDLC smart windows using AgNW transparent electrodes,^[16] which were used for an electric-field-induced orientation of LCs in PDLCs. However, AgNW networks were employed in this study to generate heat via Joule heating and provide the thermal energy to the PDLC layer.

Thermo-optical behaviors of the TSF were investigated by carrying out numerical and experimental analyses. The anomalous diffraction approach (ADA) was adopted as a scattering theory to predict temperature dependent transmittance of the TSF. While most studies using the ADA have focused on the calculation of the electric field driven transmission,^[17-19] this study dealt with the thermal behaviors of the transmittance of PDLCs. Finally, an effective operation method for the TSF is introduced for practical applications.

3.2. Experimental

3.2.1. Preparation of silver nanowire coated film

Fig. 3.1 describes the overall process for the fabrication of AgNW coated films. An aqueous AgNW solution with 0.4 wt% of solid content was provided from Cambrios Technologies Corporation, and was diluted to 0.1 wt% with a mixture of deionized water and isopropyl alcohol (4 : 1 weight ratio). PET films with 100 μm thickness were used as the substrate for AgNW coating. The PET films were pre-treated with a corona discharger before coating to enhance the adhesion strength between the film and the AgNW networks. Then, the PET film was coated with the diluted AgNW solution by using a wire-wound bar (bar no. 44), and dried under an infrared (IR) lamp for 1 h.^[20] The thickness of the coated layer measured by a micrometer was 10 μm . Adhesive copper foils with 100 mm width were attached on both sides of the film to connect the AgNWs to a direct current (DC) voltage supplier. A silver paste (Elcoat, P-100) was painted at the border between the copper foil and the AgNW coated surface to reduce the contact resistance. The dimension of the AgNW coated surface was 30 mm (L) \times 25 mm (W). Fig. 3.2 shows the final product of the AgNW coated film.

3.2.2. Fabrication of TSFs

The TSFs were fabricated by coating PDLCs on the AgNW coated films. Two types of PDLCs were used in this study. The first one was the mixture of NOA65 (Norland UV-curable resin) as the polymer matrix and 4-(4-pentylcyclohexyl)benzointrile (5PCH, Tokyo Chemical Industry) (Fig. 3.3) as the NLC phases. This mixture was mainly used for the demonstration of the TSF, and is denoted as N5P. The second one, which was the mixture of polystyrene (PS, Yakuri Pure Chemicals) with $M_w = 250,000 \text{ g mol}^{-1}$ as the polymer matrix and 5PCH, was used to support the thermo-optical behaviors of the TSF, and is called P5P.

In the TSF with N5P, the nematic-to-isotropic phase transition temperature (T_{NI})

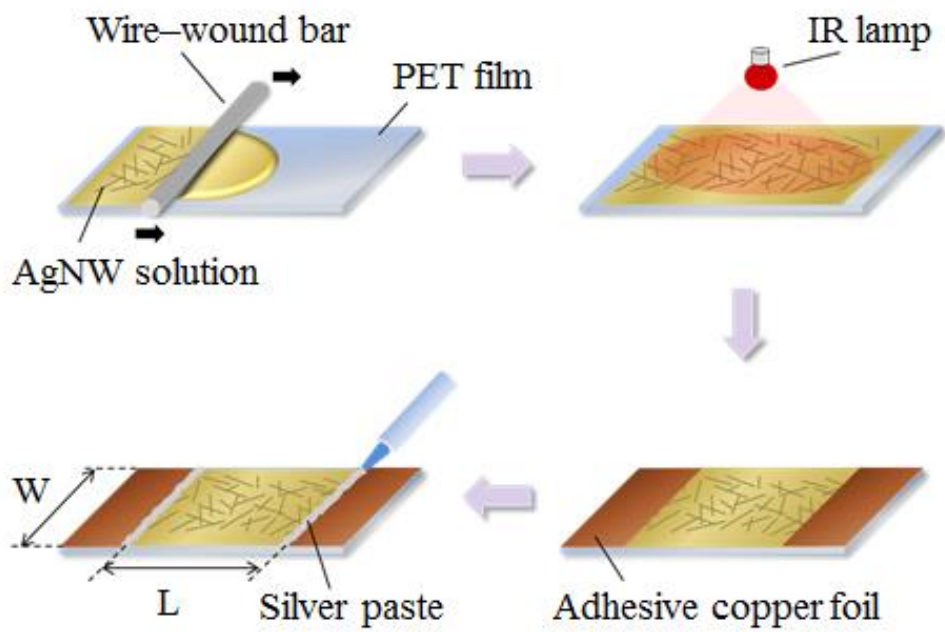


Figure 3.1 Schematic procedure for the fabrication of the AgNW coated film.



Figure 3.2 The transparent AgNW coated film.

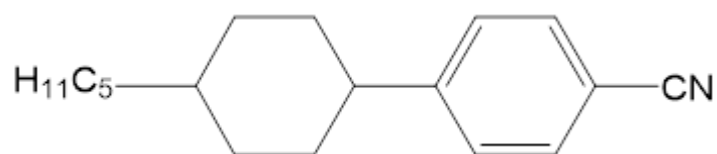


Figure 3.3 Chemical structure of 5PCH.

and the isotropic refractive index (n_i) at T_{NI} of 5PCH were 55 °C and 1.5269 at the wavelength of 546 nm, respectively.^[21,22] For the refractive index matching between the polymer matrix and the NLC droplets over T_{tr} , NOA65 was selected as the polymer matrix in PDLCs. The refractive index of NOA65 (n_p) was 1.5244 at the wavelength of 546 nm at T_{NI} (= 55 °C).^[23] The fabrication procedure of the TSF with N5P was illustrated in Fig. 3.4a. The uncured PDLC solution was prepared by mixing the same weight of 5PCH and NOA65, and was spread on the prepared AgNW coated film. The PET film with 100 μm thick, used as a cover substrate to prevent diffusion of NLCs from the polymer matrix, was placed over the spread PDLC solution, and a slide glass (75 mm \times 25 mm, 1 mm thick) was attached on top of the PET film. Spacers were used for the thickness control of the PDLC layer as depicted in Fig. 3.4a. Then, the coated PDLC solution was cured at the intensity of 1.3 mW cm^{-2} for 40 min using an unfiltered UV lamp (Vilber Lourmat, VL-4.LC), and the slide glass was removed. During curing, the PDLC layer was formed by PIPS. The thickness of the PDLC layer was measured to be 160 μm using the micrometer.

In the TSF with P5P, PS ($n = 1.59$) was selected as the polymer matrix in order to lead to a mismatch of refractive indices between the NLC droplets and the polymer matrix over T_{NI} . Fig. 3.4b represents the fabrication method of the TSF with P5P. The same weight of PS pellets and 5PCH were dissolved in toluene with the concentration of 10 wt% by a vortex mixer at room temperature for 2 h. The solution was poured into a Petri dish on a hot plate, and dried at 150 °C for 2 h. Then, the PDLC film with a several-millimeter thickness was formed by SIPS. A part of the film was cut in the size of 20 mm \times 20 mm, and placed on the prepared AgNW coated film. Similarly with the TSF with N5P, the PET film was used for the upper cover substrate, and also attached on the slide glass. As shown Fig. 3.4b, a weight corresponding to the pressure of 1kPa was placed on the slide glass to control the thickness of the PDLC layer at 70 °C for 1 h. At this time, 5PCH played as a role of a plasticizer for PS, so that the glass transition temperature (T_g) decreased.^[24] This property enabled the P5P layer to be easily compressed at lower temperature (70 °C) than T_g of pure PS (= 105 °C). Finally, the slide glass was taken off, and debris sticking out during the compression process was removed. The thickness of the PDLC layer in the TSF with P5P was measured to be 160 μm .

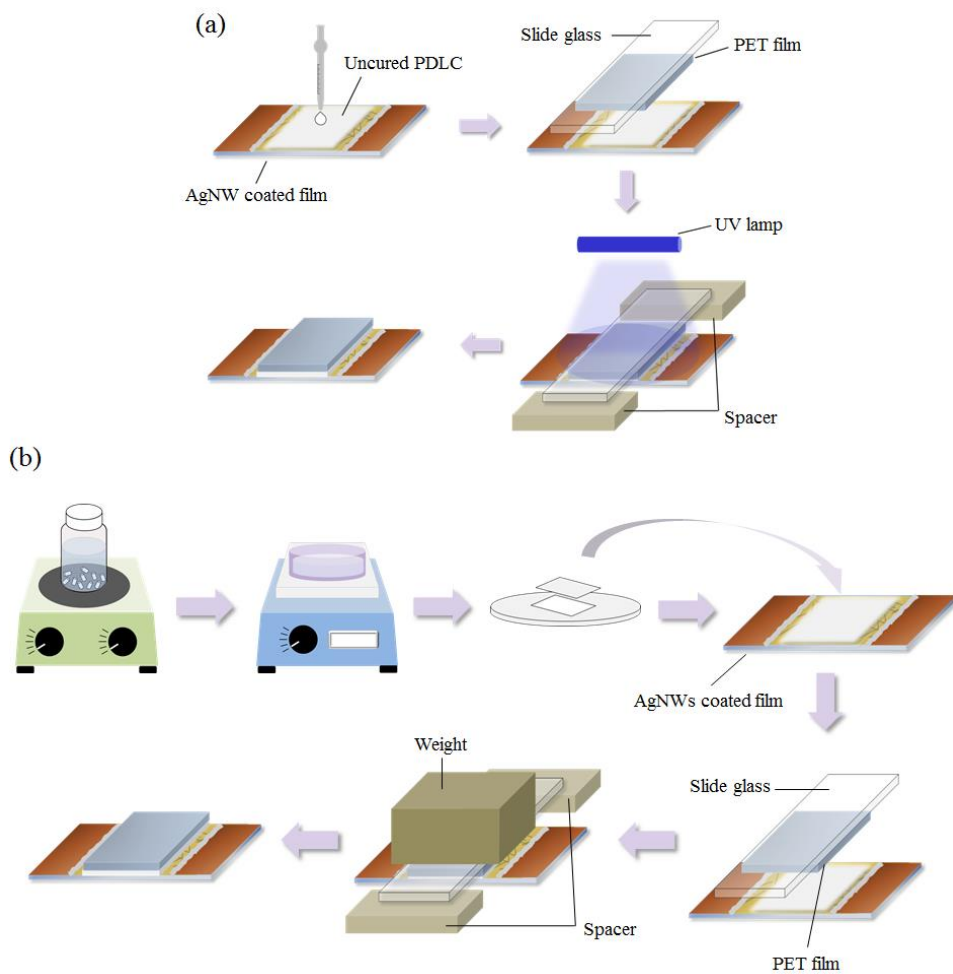


Figure 3.4 Fabrication procedures for the TSFs in the case of (a) N5P (NOA65/5PCH), and (b) P5P (PS/5PCH) as the PDLC layer.

3.2.3. Characterization and measurement

Scanning electron microscope (SEM, JEOL, JSM-7600F) was employed to observe the morphology of AgNW networks and the cross-section of the PDLC layer. Before the SEM observation of the PDLC layer, it was immersed in pentane for 1 day to extract the NLCs from the polymer matrix to distinguish boundaries of NLC droplets. To generate thermal energy via Joule heating, a DC voltage supplier (ATTEN, APS3005S) was connected to copper foils at the both sides of the AgNW coated film. The film temperature was measured by using an IR thermometer (FLUKE, VT02) and recorded every 5 s. The sheet resistance was measured using 4 point probe measurement equipment (CHANG MIN CO., LTD., CMT-SERIES) and the bulk resistance was measured by using a portable multi-meter (DONG HWA, DM-1010). An UV-visible spectrometer (Agilent Technologies, Cary 100) was used for the measurement of the optical transmission spectra of the AgNW coated films. The phase transition temperature (T_{tr}) was identified using a differential scanning calorimetry (DSC, NETZSCH, DSC 200 F3 Maia). The heating rate was $10\text{ }^{\circ}\text{C min}^{-1}$. Fig. 3.5 shows the set-up for the measurements of transmittances of the TSFs. The transmittances of the TSFs were calculated with the ratio of initial and transmitted light intensity by using the light emitted from a semiconductor laser light source (CNI Optoelectronics Technology CO., Ltd., PGL-FS-532) with a 532 nm wavelength. The light intensity was measured using a photodetector and recorded every 5 s. The photodetector was located at 2 mm from the film to minimize the disturbance of convective cooling.

3.2.4. Effective electrical power

The silver paste was used for the reduction of the contact resistance (R_c) between the copper foils and the AgNW networks. However, R_c remained high in comparison with the bulk resistance of the AgNW networks. In order to exclude R_c , we defined the effective electrical power (P_{eff}) which was consumed by the AgNW

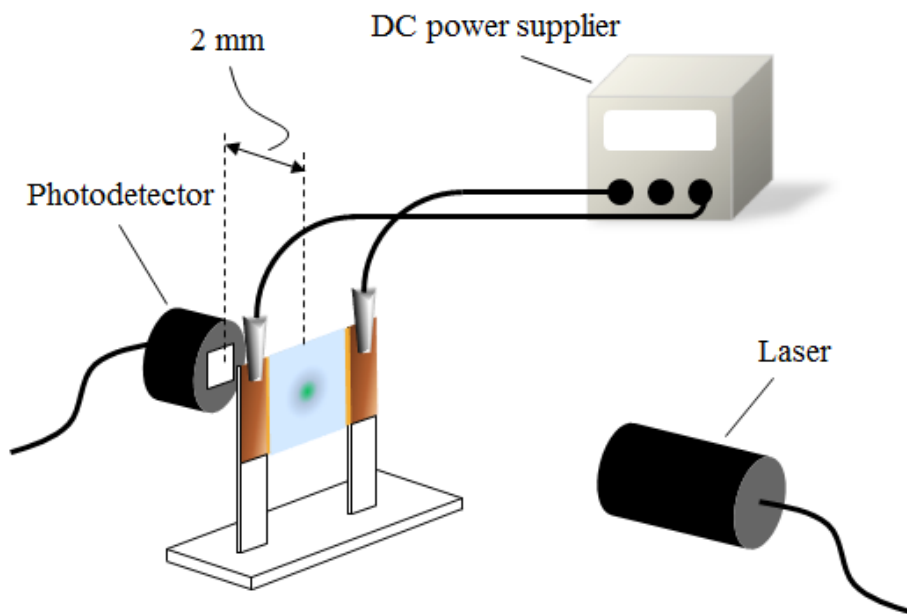


Figure 3.5 Set-up for measurements of transmittances of the TSFs.

networks only. To calculate P_{eff} , it is assumed that resistances are independent of temperature. The overall electric circuit diagram of the AgNW coated film corresponds to the series connection between the contact resistance and the bulk resistance of the AgNW networks. The contact resistance is calculated by the following equation.

$$R_c = R_t - R_{AgNW} = R_t - \rho_{res} \frac{L}{A_{AgNW}} = R_t - \left(\frac{\rho}{H} \right) \frac{L}{W} = R_t - R_s \frac{L}{W}, \quad (3-1)$$

where R_{AgNW} and R_s are the bulk resistance and the sheet resistance of the AgNW networks, respectively. R_t is the total resistance measured between the copper foils on the both sides of the AgNW coated film. ρ_{res} is the resistivity and H is the thickness of the AgNW networks. L , W , and A_{AgNW} are the length, the width, and the cross-sectional area of the AgNW coated region as depicted in Fig. 3.1. Thus, the effective voltage, which is applied only to the AgNW networks, is always lower than the applied input voltages (V_{app}) due to a voltage drop by R_c . The effective voltage (V_{eff}) and the effective electrical power (P_{eff}) applied only to the AgNW networks can be calculated by the Ohm's law as follows.

$$P_{eff} = V_{eff} I_t = (I_t R_{AgNW}) I_t = R_s \frac{L}{W} I_t^2 = R_s \frac{L}{W} \left(\frac{V_{app}}{R_t} \right)^2, \quad (3-2)$$

where I_t is the current. The values of P_{eff} are denoted as the input conditions applied to the experiments instead of the applied input voltage.

3.3. Numerical analyses

3.3.1. Temperature on film surface

If it is assumed that thermal radiation is negligible, the governing equation for the heat transfer simulation is given by

$$\rho C_p \frac{\partial T}{\partial t} = \nabla \cdot (k \nabla T) + Q, \quad (3-3)$$

where ρ is the density, C_p is the specific heat capacity, k is the thermal conductivity, and Q is the heat source supplied from the electric current. ρ , C_p , and k have different values in each layer of the TSF. Q is equal to $P_{eff} / (WL)$ on the domain of heat generation (*i.e.*, the surface of AgNW networks), but zero on the other domains. The following equation is applied as the boundary condition.

$$\tilde{n}_{sur} \cdot (k \nabla T) = h(T_{amb} - T), \quad (3-4)$$

where \tilde{n}_{sur} is the surface normal unit vector, and T_{amb} is the ambient temperature. h is the convection heat transfer coefficient, which was determined by selecting the best fitting h when simulation results were compared with experimental results in this study. The simulation results were hardly affected by the deviation of k and C_p in each layer because of a thin thickness of the TSF (370 μm). Thus, we used k and C_p values of PDLCS made of 4-cyano-4'-pentyl-1,1'-biphenyl (5CB) and polystyrene instead of those made of 5PCH and NOA65.^[25] Also, k and C_p of silver (Ag) were used instead of those of the AgNWs. The heat transfer simulation was conducted on the schematic structure of the TSF with N5P as shown in Fig. 3.6

using a multi-physics simulator (COMSOL® 4.3). All material properties used in this study are listed in Table 3.1.

3.3.2. Transmittance of TSF

A number of micrometer-sized NLC droplets in the polymer matrix work as scattering particles in the PDLC. Therefore, it is important to understand an optical scattering theory of the PDLC. For a medium where scattering particles are homogeneously dispersed, the optical transmittance (τ) is calculated by the Beer's law as follows.

$$\tau = \tau_o \exp(-N_v \sigma_s d), \quad (3-5)$$

where τ_o is the transmission coefficient, N_v is the number of droplets in a unit volume which is equal to $v/[(4/3)\pi r^3]$ where v is the volume fraction of the NLCs in the PDLC, and d is the path length of the non-scattered light in the PDLC (*i.e.*, the thickness of the PDLC). σ_s is called the sample scattering cross-section or the effective cross-section, which corresponds to the scattering shadow as shown in Fig. 3.7. In general, there are three types of models describing the sample scattering cross-section: Mie scattering theory, anomalous diffraction approach (ADA), and Rayleigh-Gans (RG) light scattering theory. The Mie theory is adequate for a medium including large particles with size from several hundred nanometers to a few micro-meters. On the other hand, the RG theory is appropriate for smaller objects than the wavelength of light (λ). The ADA is suitable for particles similar with λ . In this study, the ADA is selected as the light scattering model to calculate the sample scattering cross-sections. The calculation schemes and the terminologies for describing the ADA are referred from Ref. 19. The ADA is valid for the following conditions.

$$kr \gg 1, \quad (3-6)$$

$$n_r - 1 \ll 1, \quad (3-7)$$

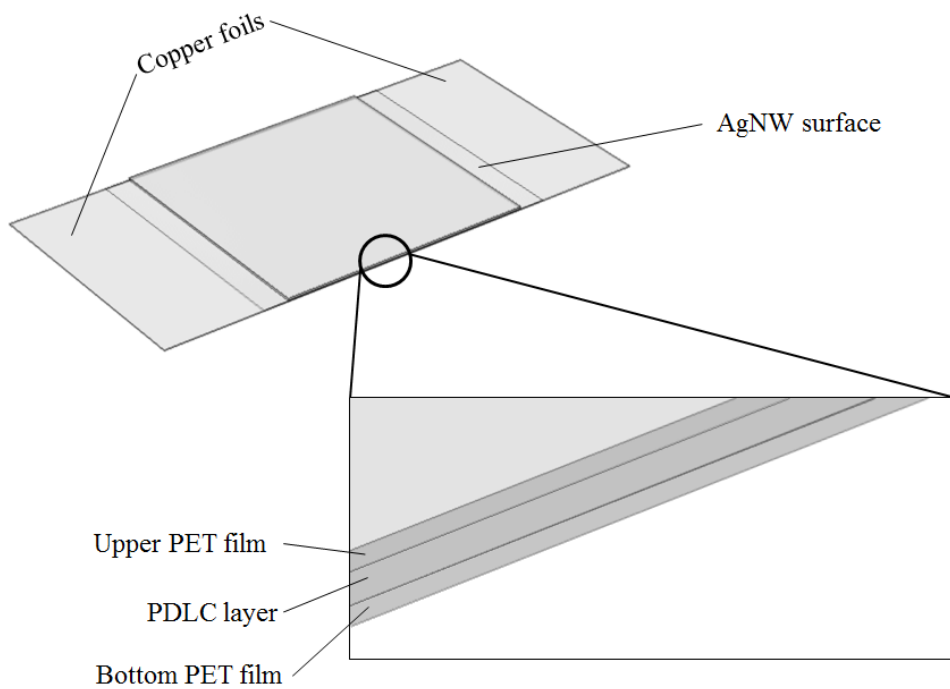


Figure 3.6 Schematic structure of the TSF for the heat transfer simulation.

Table 3.1 Material properties used for heat transfer simulation.

	PET film	AgNW networks	PDLC layer
Density, ρ / kg m^{-3}	1,380	10,500	1,105 ^{a)}
Thermal conductivity, k / $\text{W m}^{-1} \text{K}^{-1}$	0.150	420	0.135 ^[25]
Specific heat capacity, C_p / $\text{J kg}^{-1} \text{K}^{-1}$	1,000	230	1,719 ^[25]
Thickness / μm	100	10	160

^{a)}calculated by the rule of mixture from the volume fraction of 5PCH. (The densities of 5PCH and NOA65 were 1,070 and 1,120 kg m^{-3} , respectively.).

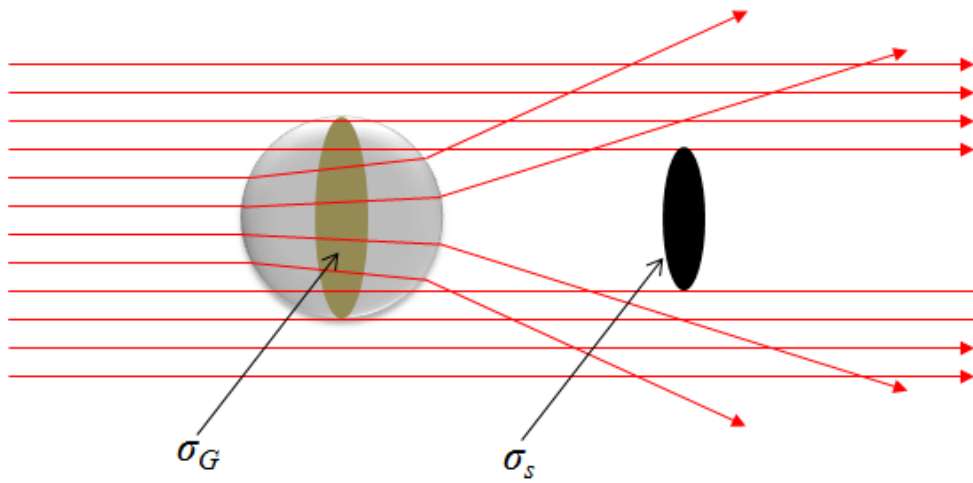


Figure 3.7 Geometrical cross-section (σ_G) and sample cross-section (σ_s). This figure was redrawn from Ref. 27.

where $k (= 2\pi/\lambda)$ is the wavenumber, r is the radius of the NLC droplets in the PDLC, $n_r (= n_d/n_p)$ is the relative refractive index, n_d and n_p are the refractive indices of the NLC droplets and the polymer matrix, respectively. From the condition of Eq. (3-7), we can neglect reflections on external and internal boundaries and the refraction of the ray passing the scattering object.^[26]

Therefore, a scattering object does not alter either the direction of the propagation or the amount of light but only induces a phase shift depending on the direction on the ray in the ADA.^[26] The sample scattering cross-section (σ_s) in the ADA is given by averaging the droplet scattering cross-section (σ_d) over all droplet orientations as follows.

$$\sigma_s = \int_0^{2\pi} d\varphi \int_0^\pi \sigma_d(\theta, \varphi) P_d(\theta, \varphi) \sin\theta d\theta, \quad (3-8)$$

where θ and φ are the inclination angle and the azimuthal angle of the droplet director (\tilde{N}_d), respectively, when the external electric field is applied as shown in Fig. 3.8. $P_d d\Omega$ means the probability that \tilde{N}_d is laid in the solid angle ($d\Omega = \sin\theta d\theta d\varphi$). For a single spherical droplet with radius r , the scattering cross-section (σ_d) is given by^[26]

$$\sigma_d = \frac{1}{2} \sigma_G (2kr)^2 \left[\left(\frac{n_{de}^*}{n_p} - 1 \right)^2 \cos^2 \alpha_d + \left(\frac{n_{do}^*}{n_p} - 1 \right)^2 \sin^2 \alpha_d \right], \quad (3-9)$$

where the droplet geometrical cross-section (σ_G) is equal to πr^2 , α_d is the polarization angle which is defined as the angle between the plane (including the wave vector \tilde{k} and the optical electric field \tilde{E}_{opt}) and the droplet incidence plane (containing the wave vector \tilde{k} and the droplet director \tilde{N}_d).^[19] \tilde{E}_{opt} is equal to the summation of $\tilde{E}_{opt}^{(O)}$ (the optical electric field of the ordinary beam) and $\tilde{E}_{opt}^{(E)}$ (the optical electric field of the extraordinary beam). n_{do}^* and n_{de}^* represent the effective ordinary and extraordinary refractive indices of the droplet, respectively. n_{do}^* is equal to n_{do} (ordinary refractive index of the droplet) but, n_{de}^* depends on

the incidence angle (γ_d) with respect to the droplet director, which is defined as the angle between \tilde{k} and \tilde{N}_d , as follow.

$$n_{de}^* = \frac{n_{do}n_{de}}{\sqrt{n_{do}^2 \sin^2 \gamma_d + n_{de}^2 \cos^2 \gamma_d}}, \quad (3-10)$$

where n_{de} is the extraordinary refractive index of the droplet. From the inner product between $\tilde{k} = (\sin \gamma_p, 0, \cos \gamma_p)$ and $\tilde{N}_d = (\sin \theta \cos \varphi, \sin \theta \sin \varphi, \cos \theta)$, γ_d is easily calculated as

$$\gamma_d = \arccos(\sin \theta \cos \varphi \sin \gamma_p + \cos \theta \cos \gamma_p), \quad (3-11)$$

where γ_p is the incidence angle with respect to the sample. In general, the optical anisotropy of the droplet ($= n_{de} - n_{do}$) is small, so that $(n_{de} - n_{do})/n_{do} \ll 1$. Thus, the Taylor expansion of Eq. (3-10) in terms of $(n_{de} - n_{do})$ is expressed as

$$n_{de}^* \simeq n_{do} + (n_{de} - n_{do}) \sin^2 \gamma_d. \quad (3-12)$$

For the orientation of the directors inside the droplets when the external electric field is applied, the bipolar configuration as shown in Fig. 3.9a is energetically preferred. In the bipolar configuration, the directors are tangentially anchored on the surface of the droplet. For such the configuration, the refractive indices of the droplet (n_{do} and n_{de}) can be expressed as^[19]

$$n_{do} = \frac{2}{\pi} n_o F \left(\frac{\pi}{2}, \frac{1}{n_e} \sqrt{\frac{2}{3} (n_e^2 - n_o^2) (1 - S_d)} \right), \quad (3-13)$$

$$n_{de} = \frac{n_o n_e}{\sqrt{\frac{2}{3} (n_o^2 - n_e^2) S_d + \frac{1}{3} (n_o^2 + 2n_e^2)}}, \quad (3-14)$$

where n_o and n_e are the ordinary and the extraordinary refractive indices of the

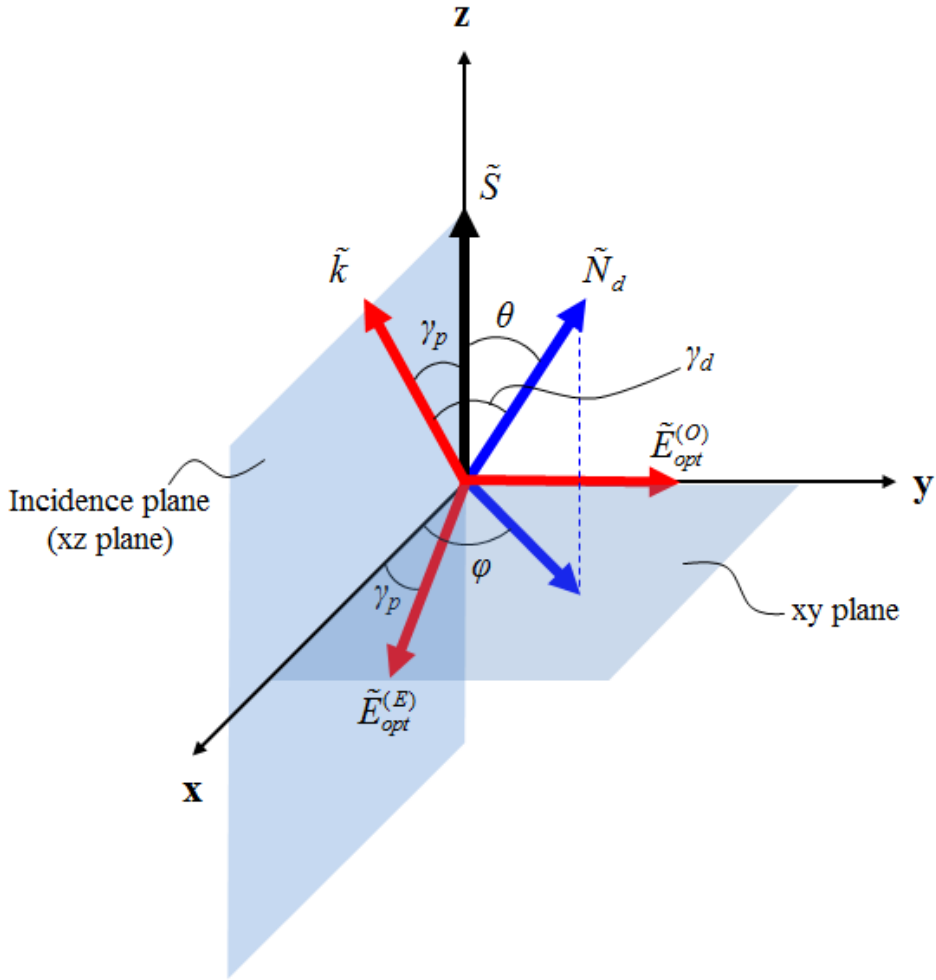


Figure 3.8 Reference frame for ADA.^[19] xz plane corresponds to the incidence plane. \tilde{S} is the unit vector along the direction of sample thickness, and \tilde{k} is the wave vector on the xz plane. $\tilde{E}_{opt}^{(O)}$ and $\tilde{E}_{opt}^{(E)}$ are the optical electric fields for the ordinary and the extraordinary beam, respectively. \tilde{N}_d represents the droplet director, which is inclined with respect to the external electric field at an angle of θ and with respect to the x-axis at an angle of φ .

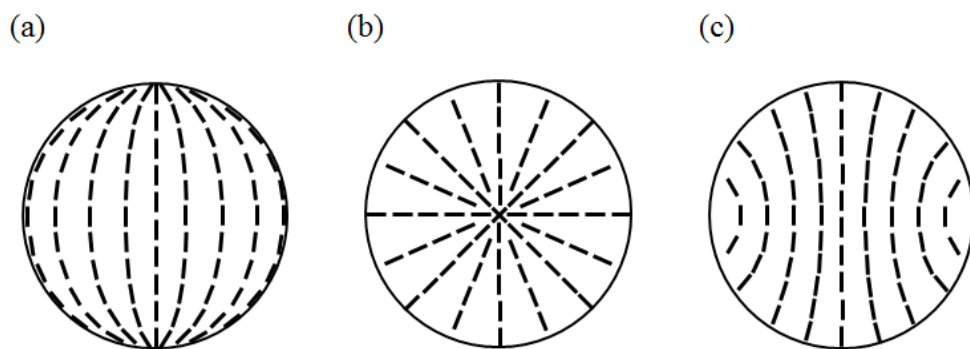


Figure 3.9 Schematic illustrations of the director configurations in the oriented droplets. (a) bipolar, (b) radial, and (c) axial configuration.

NLC. S_d is the order parameter of the droplet, which is defined as

$$S_d = \left\langle P_2 \left(\tilde{N}_d \cdot \tilde{n} \right) \right\rangle_{droplet}, \quad (3-15)$$

where \tilde{n} is the nematic director vector in the droplet, P_2 is the second-order Legendre polynomial, and the angle bracket means the average of the value. $S_d = 1$ means that all local directors of the NLCs in the droplet are aligned parallel to the droplet director. In Eq. (3-13), the function of F means the complete elliptic integral of the first kind as follows.

$$F \left(\frac{\pi}{2}, K \right) \equiv \int_0^{\pi/2} \frac{1}{\sqrt{1 - K^2 \sin^2 \theta}} d\theta, \quad (3-16)$$

Now, we can obtain the following equation by substituting Eq. (3-12) into Eq. (3-9).

$$\sigma_d = \frac{1}{2} \sigma_G (2kr)^2 \left(s_e^2 \cos^2 \alpha_d + s_o^2 \sin^2 \alpha_d \right), \quad (3-17)$$

where

$$s_e = \frac{n_{de} - (n_{de} - n_{do}) \cos^2 \gamma_d}{n_p} - 1, \quad (3-18)$$

$$s_o = \frac{n_{do}}{n_p} - 1. \quad (3-19)$$

Therefore, the sample scattering cross-section in Eq. (3-8) is given by

$$\sigma_s = \frac{1}{2} \sigma_G (2kr)^2 \int_0^{2\pi} d\varphi \int_0^\pi \left(s_e^2 \cos^2 \alpha_d + s_o^2 \sin^2 \alpha_d \right) P_d(\theta, \varphi) \sin \theta d\theta. \quad (3-20)$$

When the external electric field is applied, the probability function (P_d) can be calculated by minimizing the free energy for a droplet in the field. However, we

only consider the thermal-induced transition without the external electric field. As a result, P_d is simply given as $1/4\pi$.^[19] Thus, Eq. (3-20) is written as

$$\sigma_s = \frac{\sigma_G}{8\pi} (2kr)^2 \int_0^{2\pi} d\varphi \int_0^\pi (s_e^2 \cos^2 \alpha_d + s_o^2 \sin^2 \alpha_d) \sin \theta d\theta. \quad (3-21)$$

The polarization angle (α_d) in the absence of the electric field is calculated by

$$\alpha_d = \arcsin \frac{\sin \theta \sin \varphi}{\sqrt{1 - \cos^2 \theta}}. \quad (3-22)$$

In order to calculate the temperature dependent transmittance, S_d , n_o , n_e , and n_p should be converted to functions of temperature. If it is assumed that the order parameter of the droplet (S_d) is equal to the order parameter of the NLC in the droplet, S_d can be expressed as the following equation proposed by Haller.^[28,29]

$$S_d = S_o (T_{NI} - T)^\alpha, \quad (3-23)$$

where S_o and α are the fitting parameters. At $T \geq T_{NI}$, S_d is zero. The refractive indices of the NLC (n_o and n_e) are calculated by^[22]

$$n_o = n_{avg} - \frac{1}{3}(\Delta n)_o \left(1 - \frac{T}{T_{NI}}\right)^\beta, \quad (3-24)$$

$$n_e = n_{avg} + \frac{2}{3}(\Delta n)_o \left(1 - \frac{T}{T_{NI}}\right)^\beta, \quad (3-25)$$

where $(\Delta n)_o$ and β are the fitting parameters for n_o and n_e . n_{avg} is the average refractive index of the NLC, which is given as

$$n_{avg} = A - BT, \quad (3-26)$$

where A and B are the fitting parameters for the average refractive index of the

NLC. The refractive index of the polymer (n_p) can be expressed similarly with Eq. (3-26) as follows.^[23]

$$n_p = A' - B'T, \quad (3-27)$$

where A' and B' also represent the fitting parameters for the refractive index of the polymer matrix.

The transmission coefficient (τ_o) in Eq. (3-5) is not decided yet. τ_o means the transmittance when a medium has nothing of scattering particles. If there are no scattering particles in the PDLC layer, and the AgNW layer is neglected, the TSF has four interfaces (air/PET, PET/PDLC, PDLC/PET, and PET/air) as shown in the magnified cross-section in Fig. 3.6. Supposing the transmittance of each interface is denoted as T_1 , T_2 , T_3 , and T_4 , respectively, τ_o is equal to $T_1T_2T_3T_4$ where T_1T_4 can be experimentally determined from the transmittance of the AgNW coated film. T_2 and T_3 can be calculated from the Fresnel equation for normal incidence of unpolarized light as follows.

$$T_2 = T_3 = 1 - \left| \frac{n_{PET} - n_{PDLC}}{n_{PET} + n_{PDLC}} \right|^2, \quad (3-28)$$

where $n_{PET} = 1.58$ is the refractive index of the PET film, and n_{PDLC} is the refractive index of the PDLC layer. n_{PDLC} is calculated using the rule of mixture as follows.

$$n_{PDLC} = \nu n_{avg} + (1 - \nu)n_p, \quad (3-29)$$

where ν is the volume fraction of 5PCH, and n_p is given as expressed in Eq. (3-27). n_{avg} is the average refractive index of the NLC, which is referred from Fig. 3.10 representing temperature dependent refractive indices of 5PCH calculated from Eqs. (3-24) - (3-26). n_{avg} over at $T = T_{NI}$ is equivalent to the isotropic refractive index of 5PCH.

We used the temperatures not in the PDLC layer but on the surface of the upper PET film. Fig. 3.11 shows the temperature profiles calculated by the heat transfer

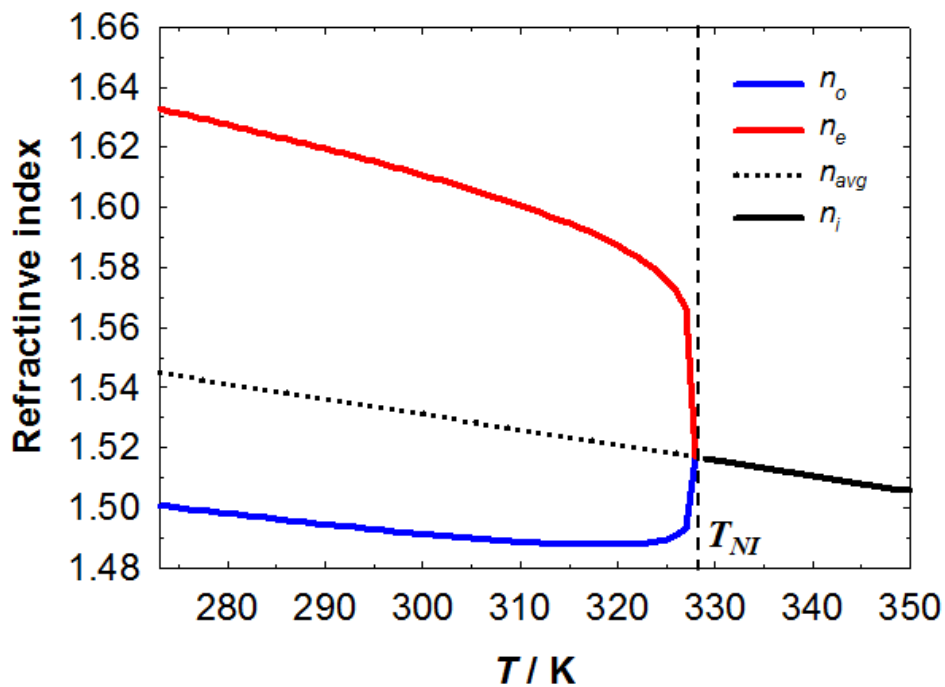


Figure 3.10 Temperature dependent refractive indices of 5PCH. $(\Delta n)_o = 0.1719$, $T_{NI} = 328$ K, $\beta = 0.1473$, $A = 1.6837$, and $B = 5.09 \times 10^{-4} \text{ K}^{-1}$ at the wavelength of 546 nm are used as the fitting parameters.^[22]

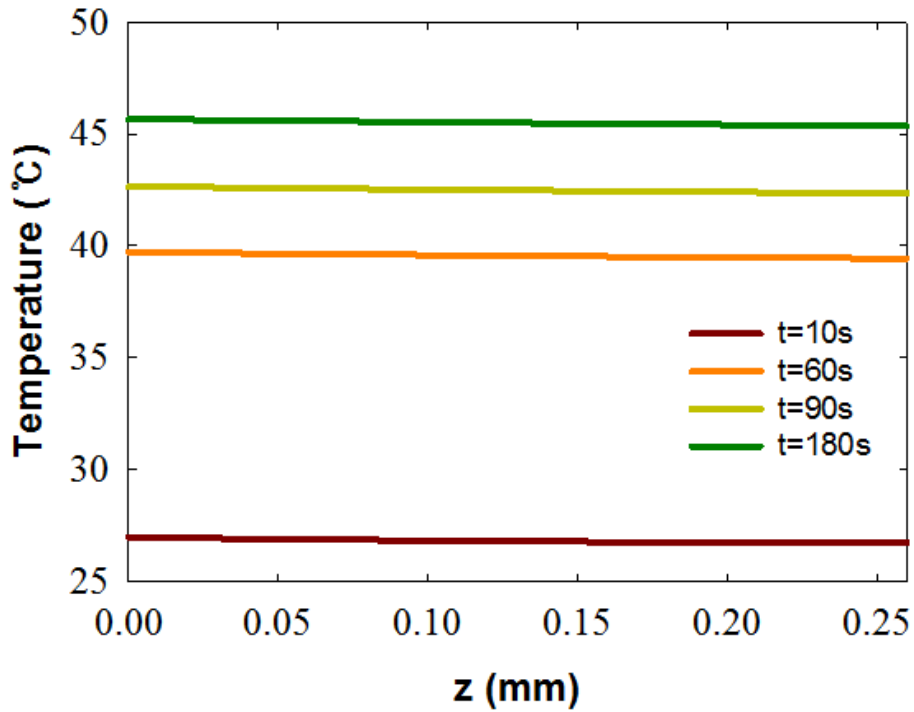


Figure 3.11 Temperature profiles along the direction of thickness obtained from the simulation results of the TSF with N5P operated at $P_{eff} = 0.258$ W.

simulation along the direction of film thickness. At each time step, the temperature differences between $z = 0$ mm (the surface of AgNW networks) and $z = 0.26$ mm (the surface of upper PET film) are within 0.5 °C. Therefore, it is acceptable to use the temperature at the film surface ($z = 0.26$ mm) for the calculation of transmittance. All parameters to calculate the transmittance of the TSF with N5P are listed in Table 3.2. By using these parameter and the related equations such as Eq. (3-5) and Eqs. (3-21) - (3-27), the temperature dependent transmittances are calculated.

Table 3.2 Parameters for the calculation of the transmittances of the TSF with N5P.

S_o	0.384 ^[29]	A	1.6837 ^[22]
α	0.165 ^[29]	B / K^{-1}	5.09×10^{-4} ^[22]
T_{NI} / K	328 ^[21]	A'	1.5828 ^[23]
$(\Delta n)_o$	0.1719 ^[22]	B' / K^{-1}	1.78×10^{-4} ^[23]
β	0.1473 ^[22]	-	-

3.4. Results and discussion

3.4.1. Performance of AgNW coated film

Fig. 3.12 shows the SEM images of the surfaces of the AgNW coated films. The average diameter of AgNWs was 35 nm and the aspect ratio was over 200. The large aspect ratio of AgNWs enables the formation of the percolation networks with a number of inter-nanowire junctions.^[30] Consequently, the sheet resistance (R_s) of the AgNW coated film becomes as low as that of ITO. R_s measured by 4 point probe measurement varied from 9.2 to 10.5 $\Omega \text{ sq}^{-1}$ and the transmittance was measured to be around 85 % as shown in Fig. 3.13. The transmittance fluctuation in Fig. 3.13 is caused by the thin-film interference at the interface between the AgNW networks and the PET film.^[31]

When the AgNW coated film was subjected to the DC voltage, the total currents (I_t) can be calculated from the applied input voltages (V_{app}) and the total resistances (R_t) measured by the multi-meter. Therefore, the effective voltages (V_{eff}) and the effective electrical powers (P_{eff}) can be calculated from Eq. (3-2). The results are given in Table 3.3. At various P_{eff} , time dependent temperature profiles at the center of the surface of the AgNW coated film were measured as shown in Fig. 3.14. The DC voltage supplier was switched on for 180 s and then switched off. The maximum temperature increased as P_{eff} increased. The temperature profiles are determined by the interaction between heat generation by Joule heating and cooling by natural air convection. The simulation results for the temperature evolutions are also plotted in Fig. 3.14 and represented in Fig. 3.15 as temperature contours using $h = 12.0 \text{ W m}^{-2} \text{ K}^{-1}$. The results agree with the experimental results for all cases as shown in Fig. 3.14.

3.4.2. Thermo-optical behaviors of TSFs

Fig. 3.16 exhibits the morphology of the PDLC layer in the TSF with N5P. A number of pores act as scattering particles when the temperature is below T_{tr} . We obtained the average droplet

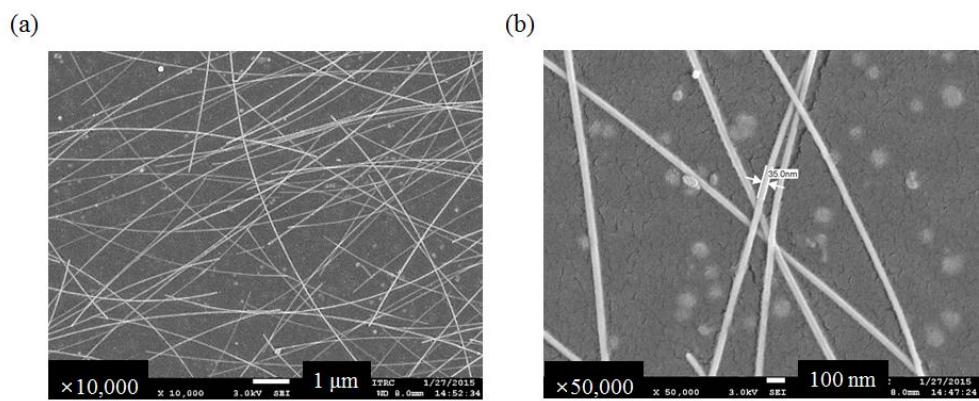


Figure 3.12 SEM images of the surfaces of the AgNW coated film magnified with (a) 10,000 times and (b) 50,000 times.

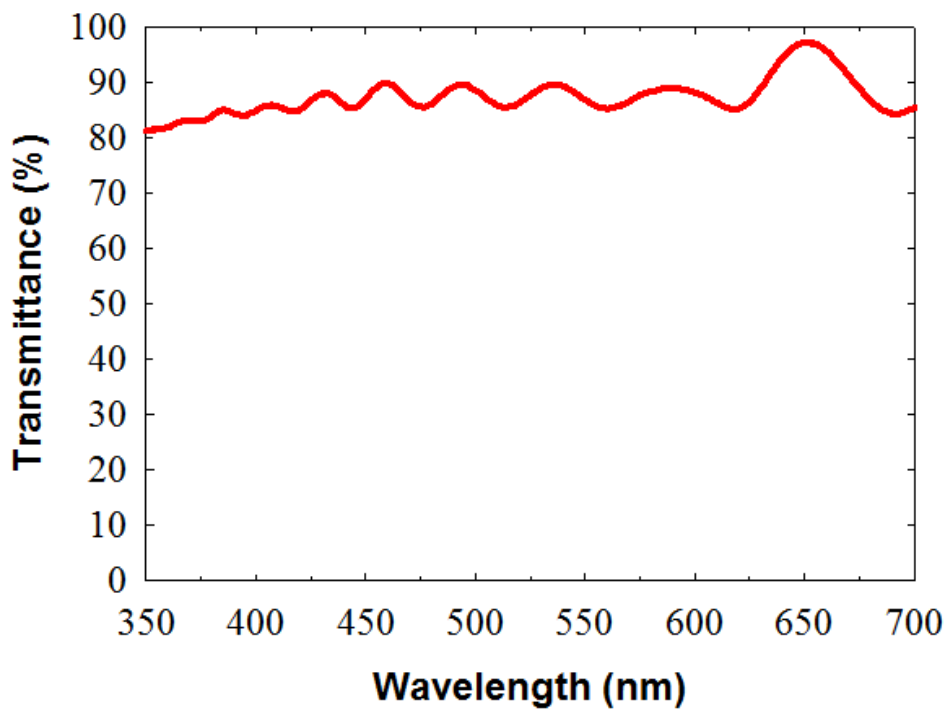


Figure 3.13 Transmittance of the AgNW coated film measured using an UV-visible spectrometer.

Table 3.3 Resistances, effective voltages and powers of the AgNW coated film.

V_{app} / V	R_t / Ω	I_t / A	$R_s / \Omega \text{ sq}^{-1}$	R_{AgNW} / Ω	R_c / Ω	V_{eff} / V	P_{eff} / W
2		0.096				1.194	0.115
3	20.80	0.144	10.35	12.42	8.38	1.791	0.258
4		0.192				2.388	0.459
5		0.240				2.986	0.718

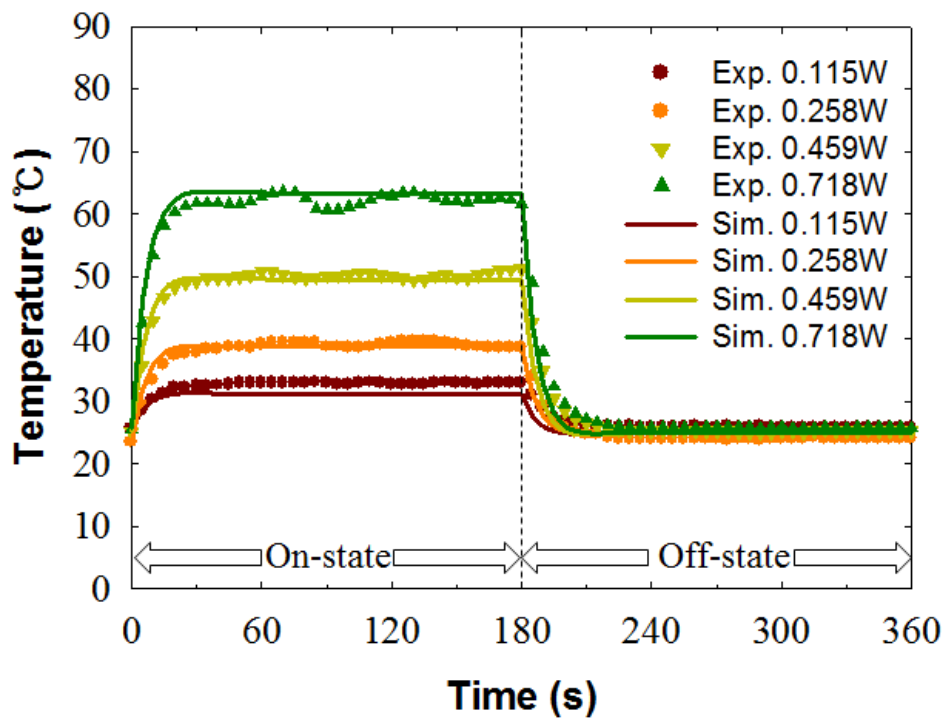


Figure 3.14 Temperature evolutions of the AgNW coated film at various effective electrical powers (dots: experimental results, lines: simulation results).

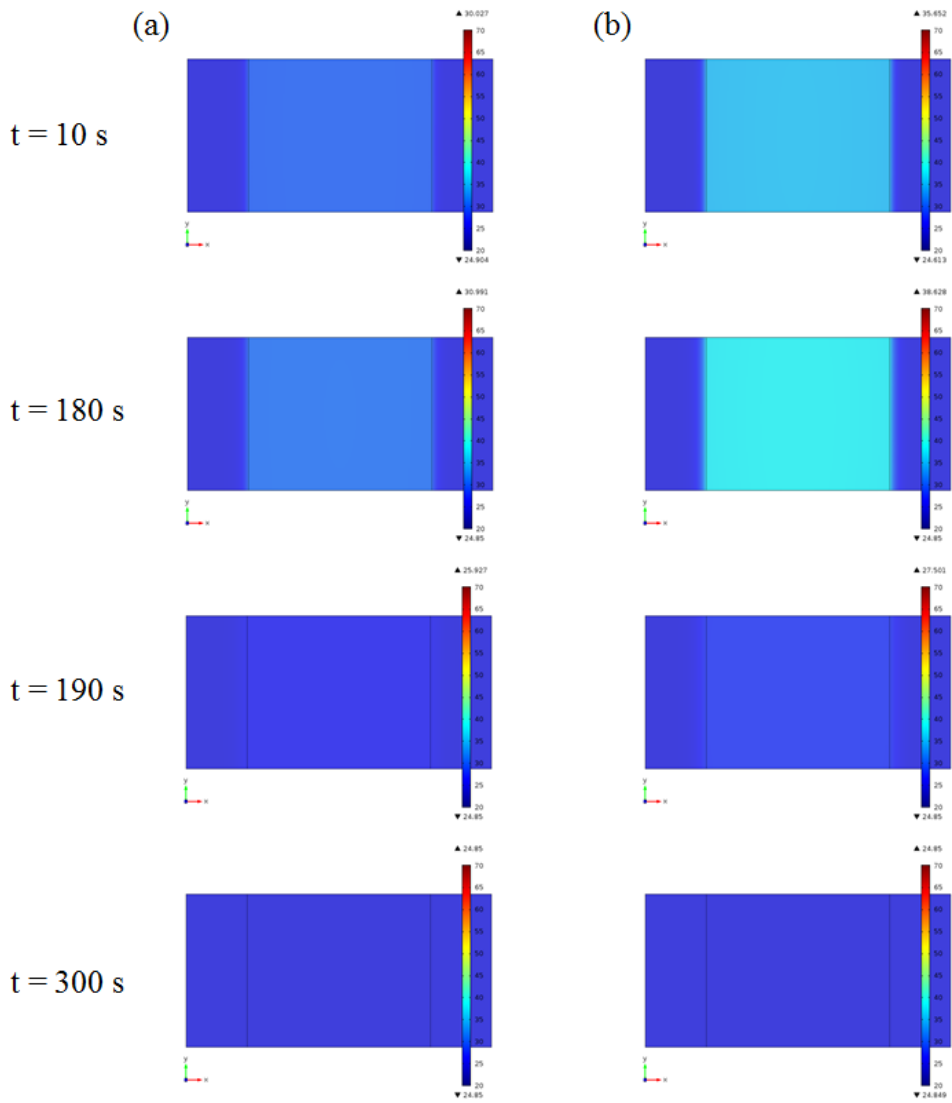


Figure 3.15 Temperature contours of the AgNW coated film acquired from the simulation results at (a) $P_{eff} = 0.115$ W, (b) $P_{eff} = 0.258$ W, (c) $P_{eff} = 0.459$ W, and (d) $P_{eff} = 0.718$ W.

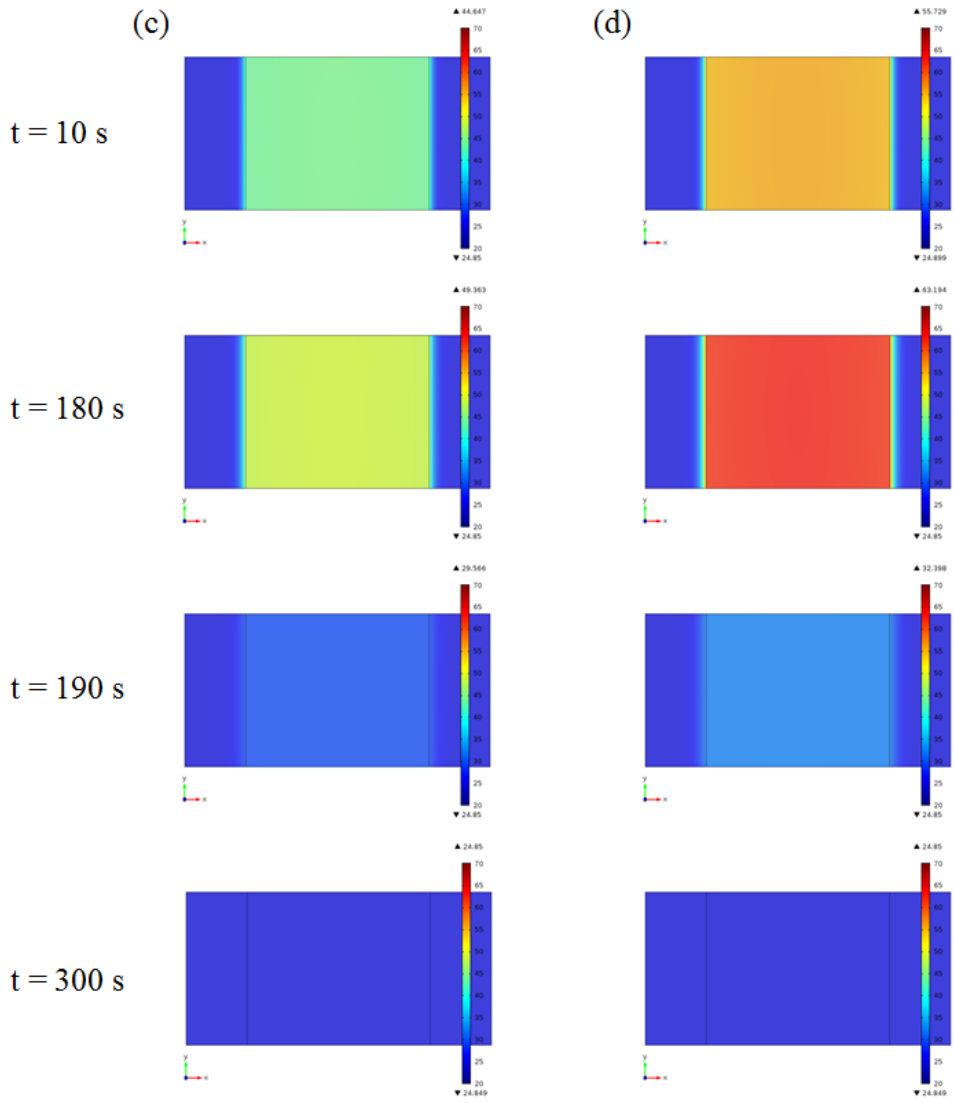


Figure 3.15 (continued)

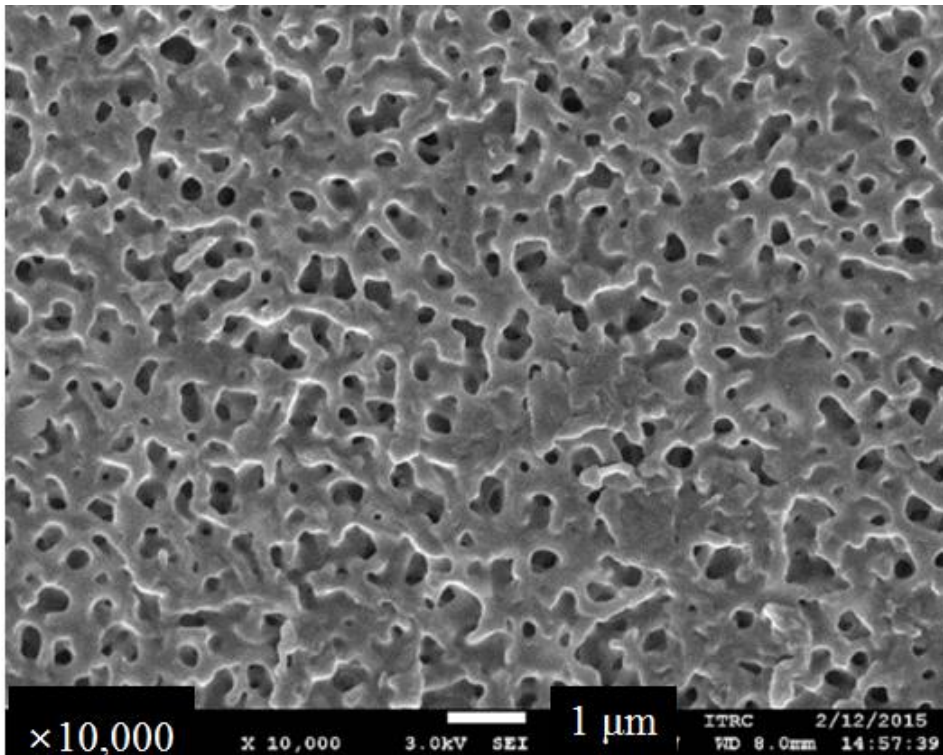


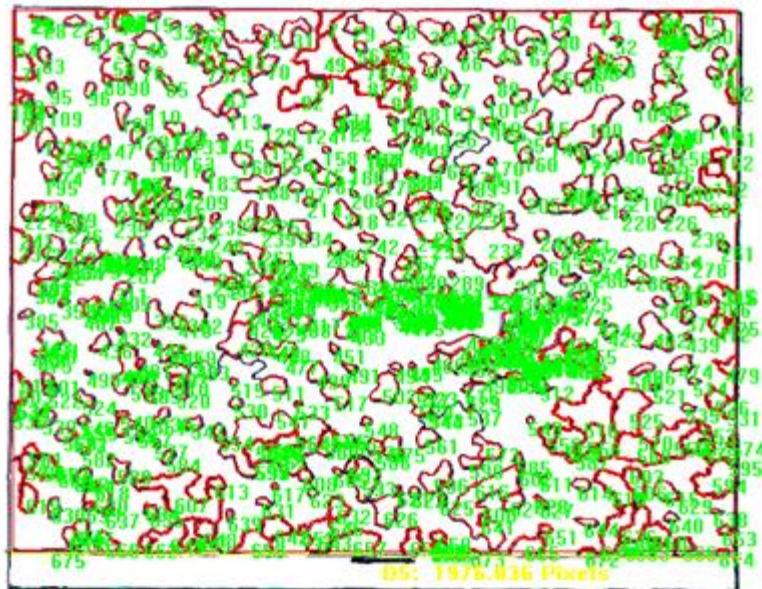
Figure 3.16 SEM image of the cross-section of PDLC layer in the TSF with N5P.

radius (r), which was $4 / \pi$ times the radius calculated from the SEM image, and the volume fraction (v) of droplets, which was similar to the area fraction of droplets determined by the image processing software (Image-Pro Plus 6.0) from the SEM image.^[32] Fig. 3.17 shows the post-processed image of the cross-section of the PDLC layer to calculate the average diameter and the droplet-size distribution. As a result, r was calculated to be $0.328 \mu\text{m}$, and v was 0.298 which was smaller than the volume fraction calculated from the mixing ratio of NOA65 and 5PCH (1 : 1) because a significant fraction of the LCs was dissolved in the polymer matrix for plasticization of the matrix and wasted.^[33]

Fig. 3.18 shows the temperature evolution at the center of the TSF with N5P during heating (0 - 180 s) and cooling (180 - 360 s). The TSF has higher maximum temperature ($47.7 \text{ }^\circ\text{C}$) than that of the AgNW coated film ($39.7 \text{ }^\circ\text{C}$) as shown in Fig. 3.14 at the same P_{eff} of 0.258W . The maximum temperature difference is attributed to the difference in the convection heat transfer coefficient (h) between the two surfaces. We determined the heat transfer coefficients for the AgNW coated film and the TSF through the heat transfer simulation as previously mentioned. The simulation results for the thermal behavior of the TSF are also plotted in Fig. 3.18, and represented as temperature contours in Fig. 3.19 using $h = 7.5 \text{ W m}^{-2} \text{ K}^{-1}$. On the other hand, $h = 12.0 \text{ W m}^{-2} \text{ K}^{-1}$ was used for the AgNW coated film as mentioned in the previous section. The smaller h value of the TSF allows it to have higher saturated temperature than the AgNW coated film at the same condition. The difference between the heat transfer coefficients of the AgNW coated film and the TSF is caused by the difference in the surface area. The temperatures obtained from the simulation were lower than those measured experimentally in the transient regime because we did not consider the changes of material properties of the PDLC layer such as the heat capacity, the thermal conductivity, and the density variations induced by the phase transition of NLCs during heating and cooling.

The time dependent transmittances of the TSF with N5P were plotted in Fig. 3.20. Upon switching on the DC voltage supplier, the transmittances rapidly increased within 30 s for all cases, whereas sudden decreases of the transmittances were observed in about 30 s after switching off. Fig. 3.21 shows the photos of the samples when measuring the transmittance at each time. The overall surfaces of the TSFs became transparent in 30 s at high P_{eff} of 0.387 W

(a)



(b)

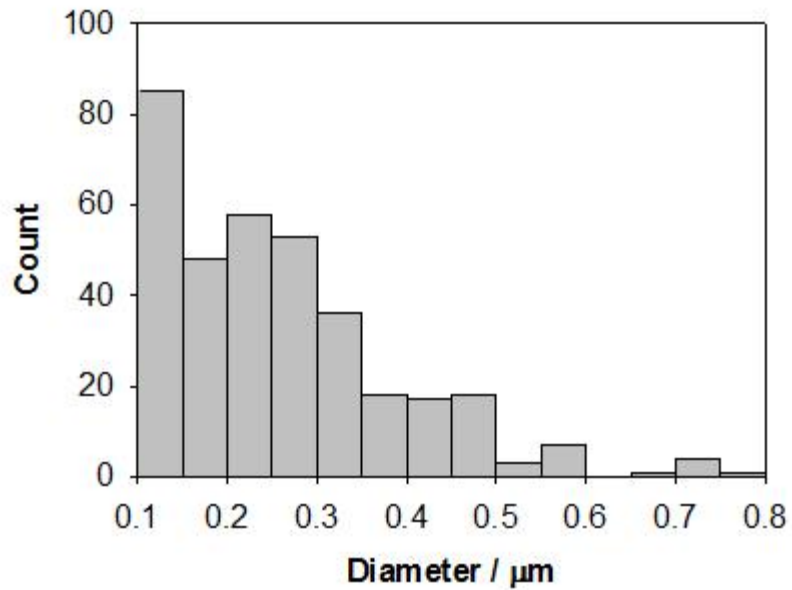


Figure 3.17 (a) Post-processed image to calculate the average diameter. (b) Droplet-size distribution.

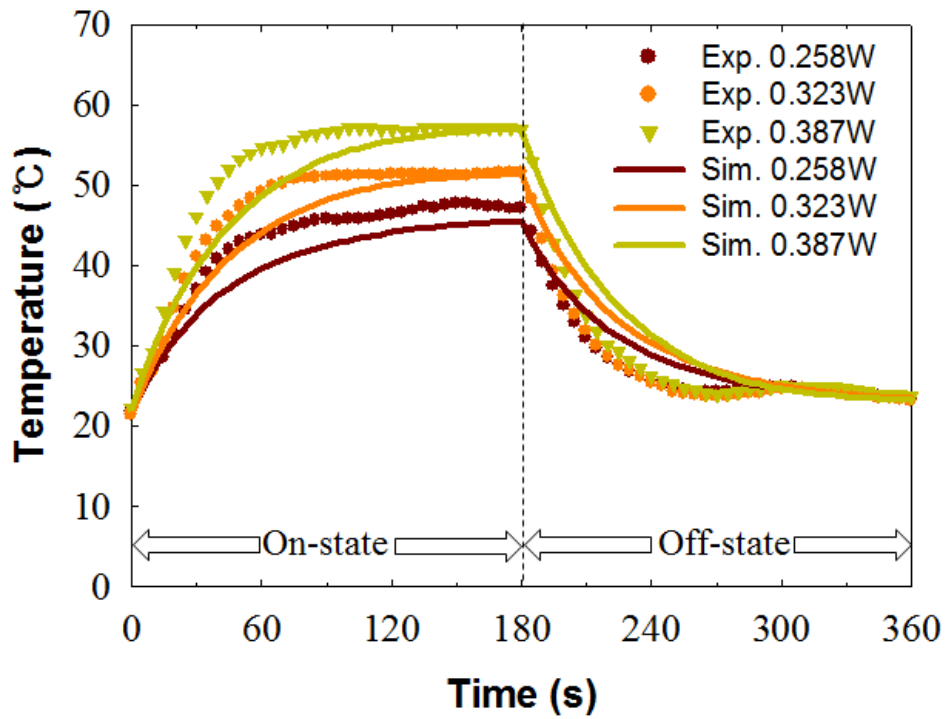


Figure 3.18 Time dependent temperature profiles of the TFS with N5P at different effective electrical powers (dots: Experimental results, lines: simulation results).

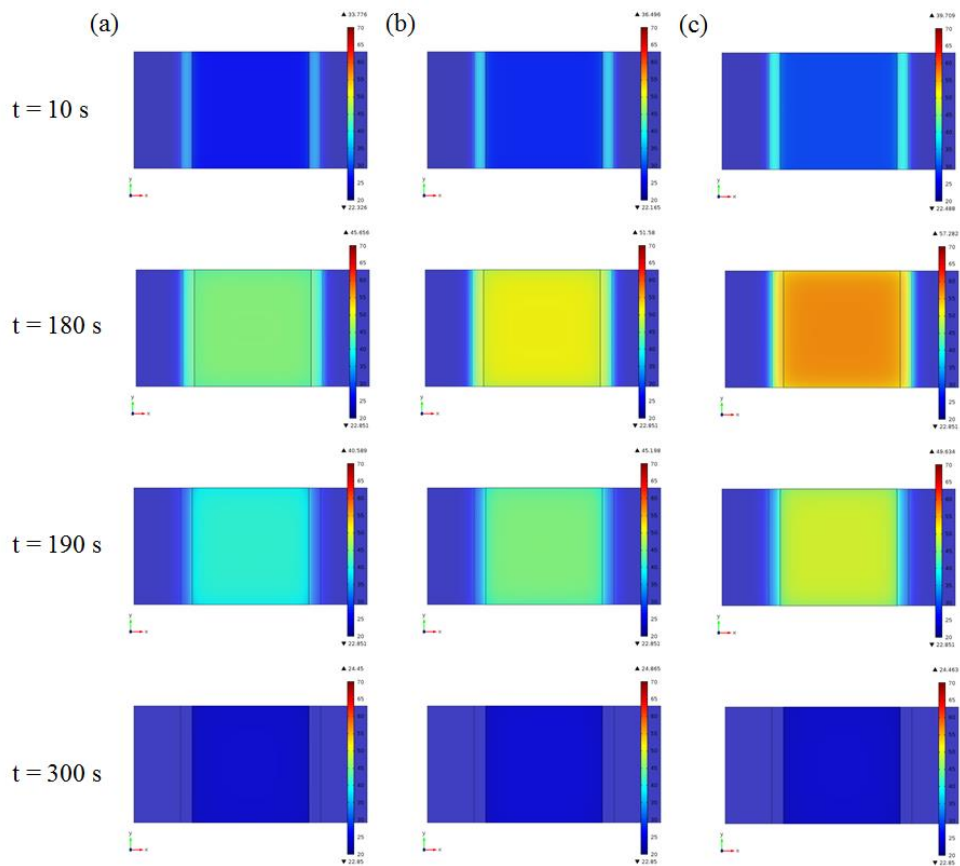


Figure 3.19 Temperature contours of the TSF with N5P acquired from the simulation results at (a) $P_{eff} = 0.258$ W, (b) $P_{eff} = 0.323$ W, and (c) $P_{eff} = 0.387$ W.

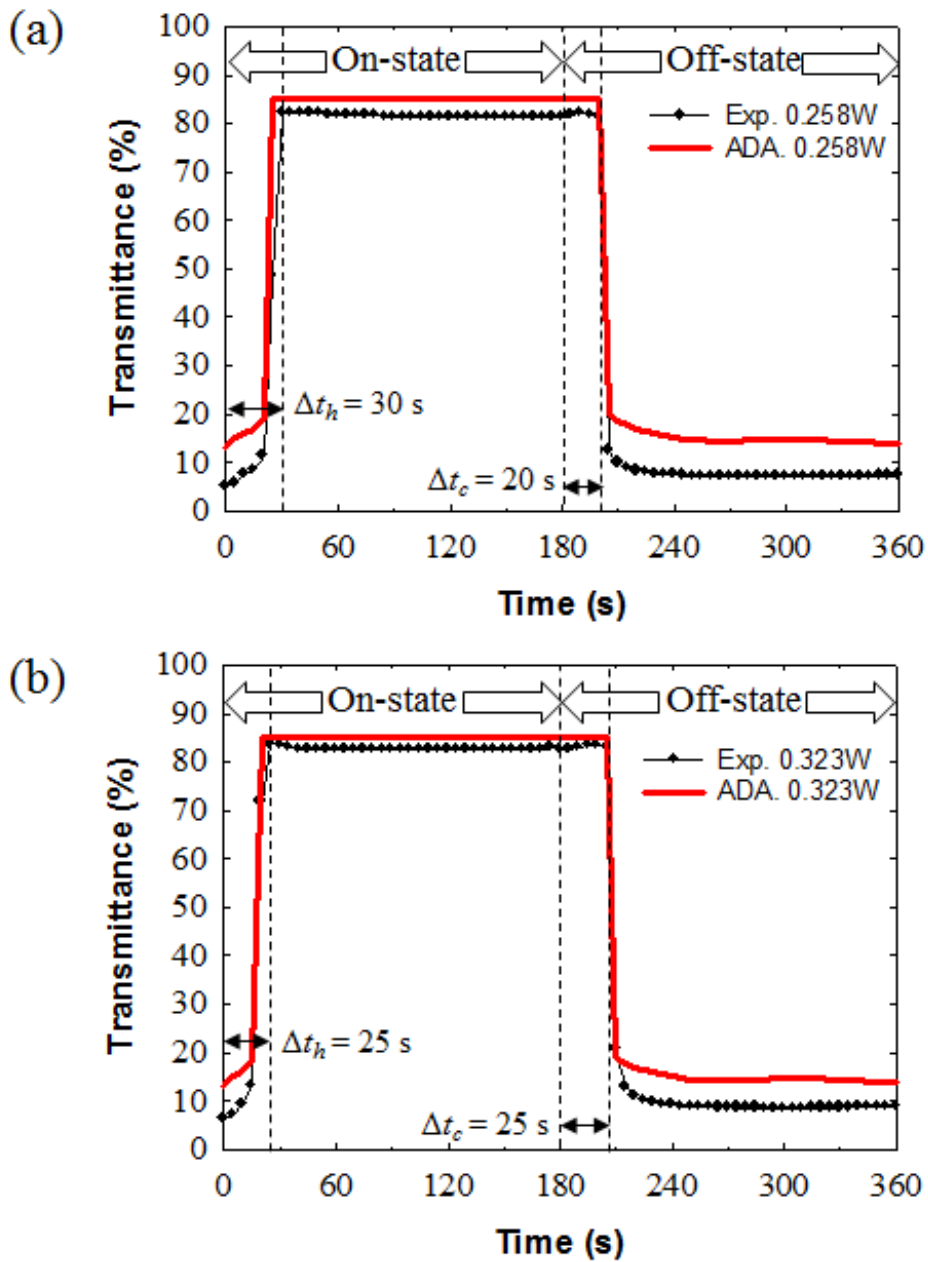


Figure 3.20 Comparison of transmittance evolutions between experimental (black dots and lines) and simulation (red lines) results at effective electrical powers of (a) 0.258 W, (b) 0.323 W, and (c) 0.387 W.

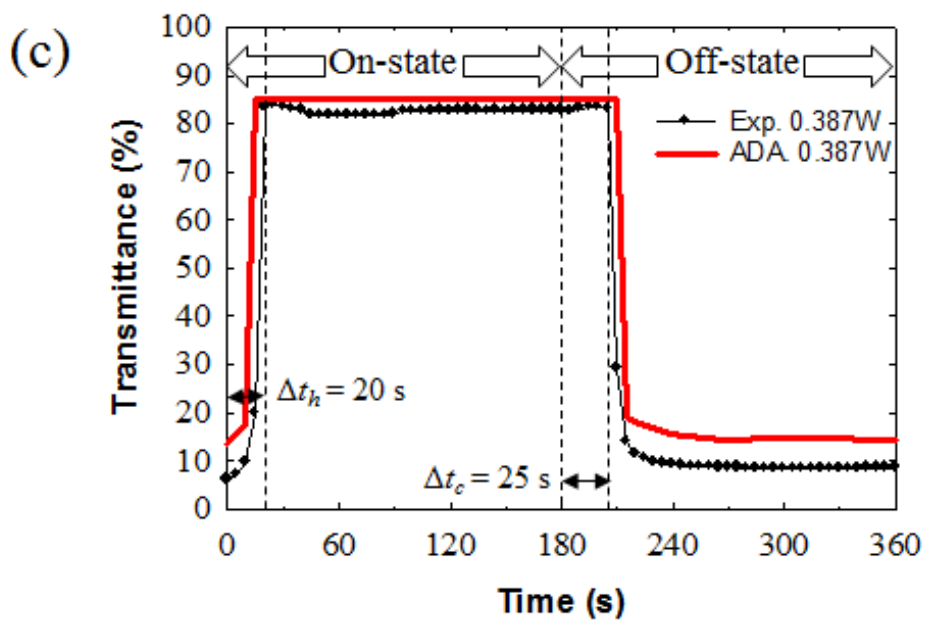


Figure 3.20 (continued)

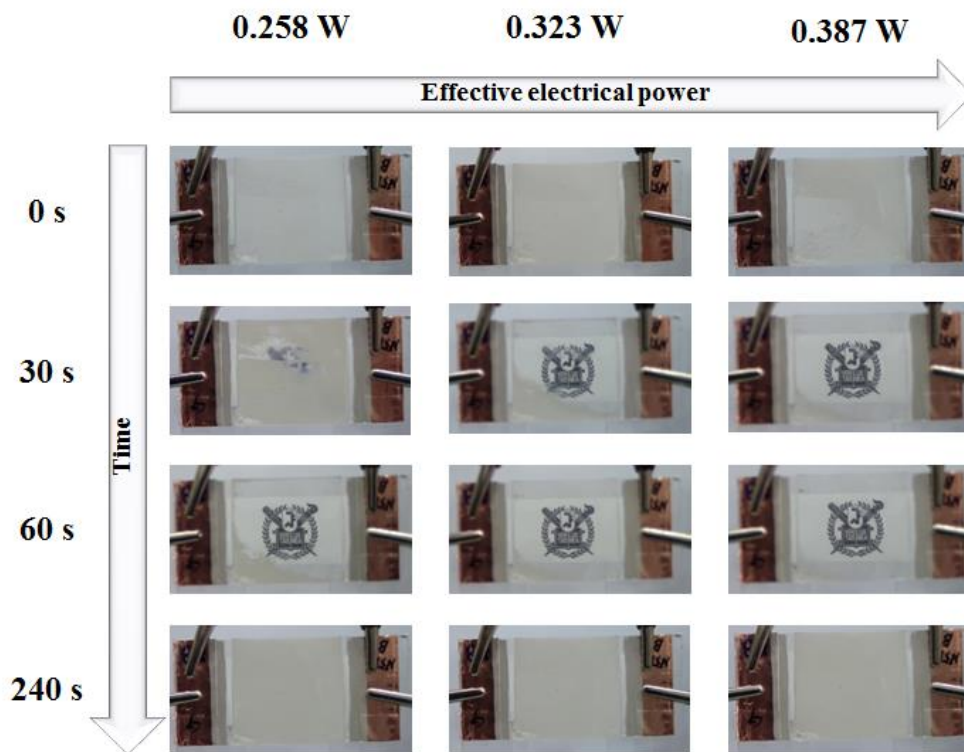


Figure 3.21 Appearance of the TSF with N5P during the transmittance measurements at each time. The logos were located at 10 cm behind the TSF to identify opaque or clear state.

but the film at P_{eff} of 0.258 W was partially clear. In order to evaluate the optical transition time at each P_{eff} , we defined Δt_h (time required to reach the maximum transmittance after switching on) and Δt_c (time required for the transmittance to begin to drop after switching off). It was found that Δt_h was 30 s at 0.258 W, 25 s at 0.323 W, and 20 s at 0.387 W. The higher the electrical power is, the steeper the gradient of temperature is as shown in Fig. 3.18. Therefore, Δt_h decreases as P_{eff} increases. On the other hand, Δt_c increases with increasing P_{eff} because the difference between the maximum temperature and T_{tr} becomes larger as P_{eff} increases. Although the maximum temperatures at $P_{eff} = 0.258$ W and 0.323 W shown in Fig. 3.18 are below 55 °C (*i.e.*, T_{NI} of 5PCH), the TSFs show high transmittance at the same condition as shown in Fig. 3.20a and 3.20b. This means that T_{tr} is lower than T_{NI} (= 55 °C), which is related with phase behaviors in a mixture of NLCs and polymers.

In the next section, we will look into the phase behaviors of the TSF in more details, which will be utilized for estimations of temperature dependent transmittance evolutions of the TSF.

3.4.3. Phase transition of TSFs

To evaluate exact T_{tr} of the TSF with N5P, the transmittances with respect to temperature are plotted as shown in Fig. 3.22 by combining Fig. 3.18 and 3.20. T_{tr} is in the range of 30 to 37 °C. T_{tr} is also confirmed by the DSC thermogram of the PDLC layer in the TSF with N5P as shown in Fig. 3.23, where the transition peak appears at 33.4 °C which corresponds to T_{tr} . The decrease of T_{tr} from 55 °C (= T_{NI}) to 33.4 °C is caused by the mutual solubility between the polymer matrix and the LCs. Some polymer matrix material remains trapped in the NLC droplets.^[33] The conventional phase diagram as shown in Fig. 1.10 depicts well such a decrease of T_{tr} as mentioned in Theoretical background section. The UCST curve represents T_{tr} at each volume fraction of the NLC. In regime of I, the polymer matrix and the NLC undergo swelling and form the isotropic swollen network gel.^[34] If the volume fraction of NLC in the PDLC layer is equal to v_2 , the DSC thermogram will display two peaks at T_{NI} and T_2 , while it will show only one peak at T_1 if the

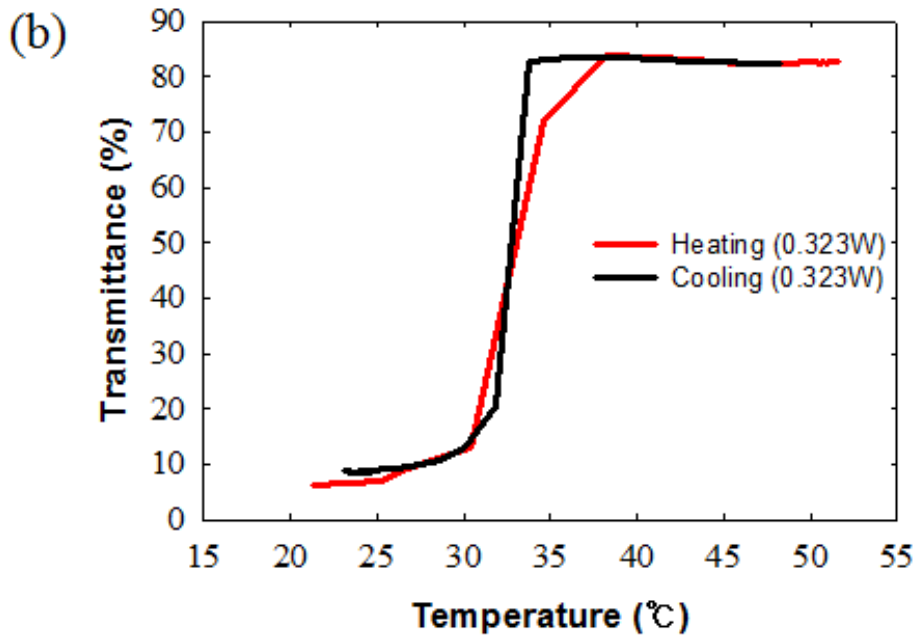
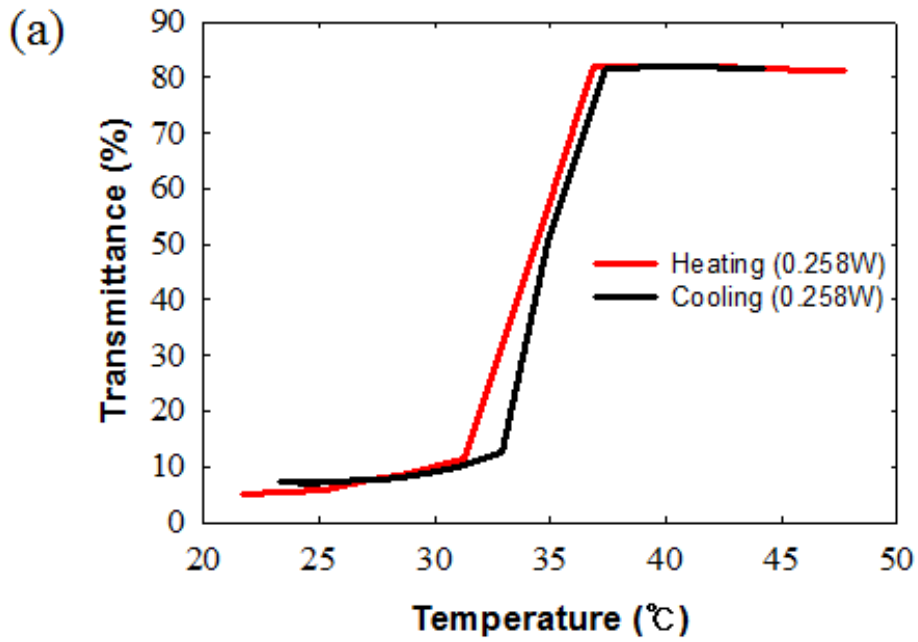


Figure 3.22 Transmittance profiles as a function of temperature at (a) 0.258 W, (b) 0.323 W, and (c) 0.387 W during heating and cooling.

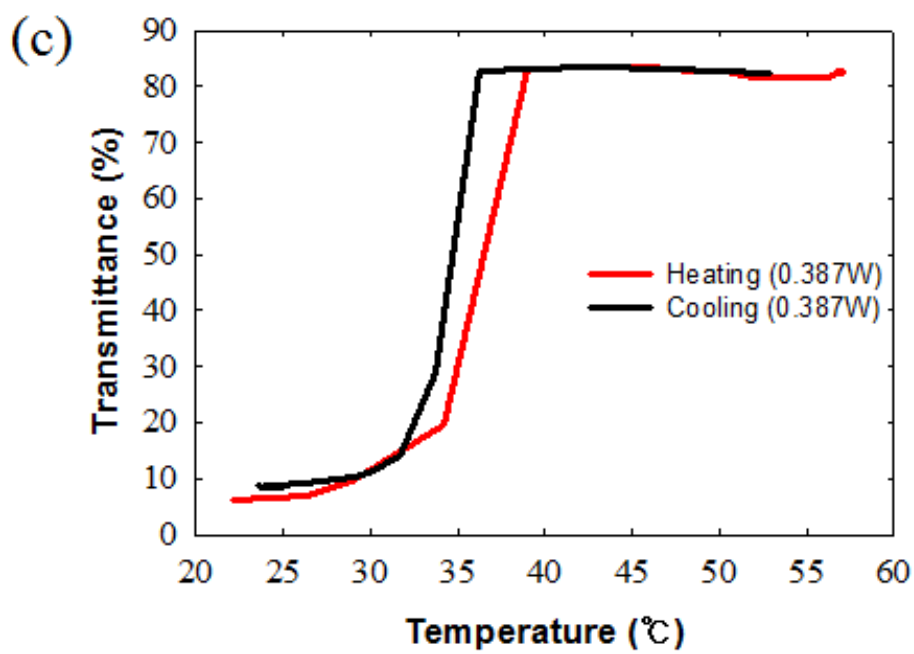


Figure 3.22 (continued)

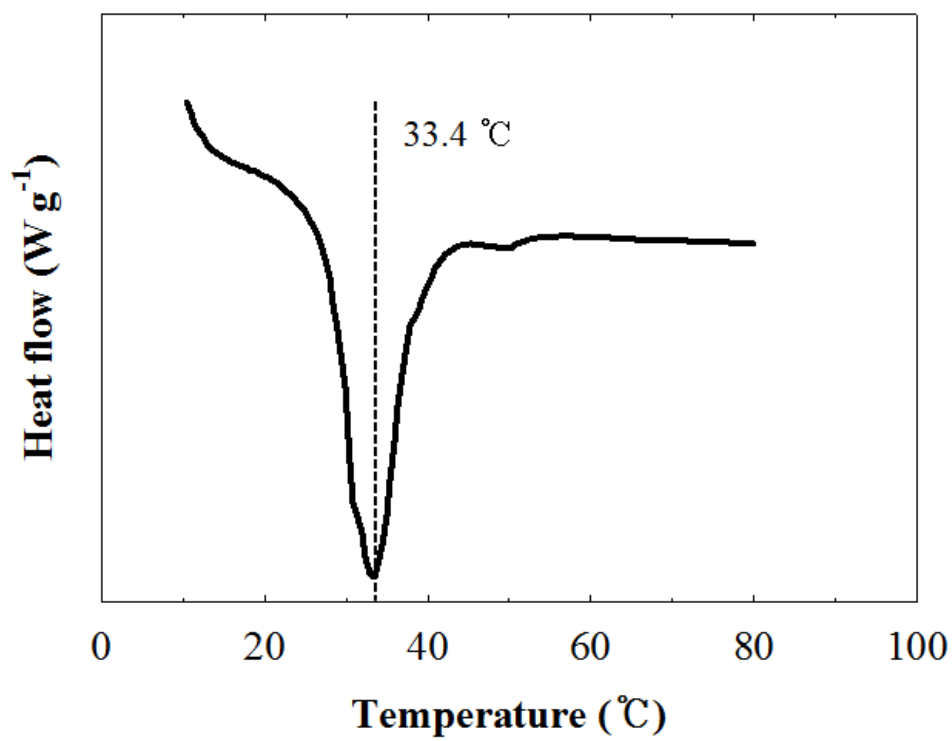


Figure 3.23 DSC thermogram of the PDLC layer in the TSF with N5P.

volume fraction is v_1 . In the TSF, PDLCs during heating follows the phase transition from I + N to I due to the decrease of T_{tr} in comparison with T_{NI} because the DSC thermogram shown in Figure 3.23 shows only one peak. As a result, the refractive indices of the NLC droplet and polymer matrix can be regarded as equivalent in regime of I at $T > T_{tr}$.

The transmittances of the TSFs with N5P were calculated from the characteristics of the phase transition of PDLCs by applying the ADA theory and also plotted in Fig. 3.20. Since the PDLC layer exhibits isotropic single phase at above T_{tr} , interfaces between the NLC droplets and the polymer matrix disappear. This means that σ_s in Eq. (3-21) is equal to zero because s_e and s_o are zero from Eqs. (3-18) and (3-19) due to $n_{de} = n_{do} = n_p = n_{PDLC}$ at $T > T_{tr}$. As a result, the transmittance (τ) is simply equal to τ_o by Eq. (3-5) at $T > T_{tr}$. Therefore, the transmittance of the TSFs does not depend on temperature and is maintained, and remains as constant at $T > T_{tr}$ due to the isotropic single phase of PDLCs. However, in the transient regime at $T < T_{tr}$, the transmittance is suddenly increased or decreased due to the change of the order parameter and the refractive indices of LCs according to temperature. The transmittance of initial and final states has a small deviation between the experimental and simulation results. Such deviation is induced by the existence of the acceptance angle of the photodetector (PD) caused by the distance between the film and the PD. The acceptance angle is calculated to be about $\pm 54^\circ$ from the sensitive area (7.5 mm^2 , square shape) of the PD and the distance (2 mm). The transmitted light was scattered at $T < T_{tr}$ such that the highly scattered light ($> 54^\circ$) could not be totally collected in the PD. Consequently, the experimental results show lower values than those of the calculation.

In the case of the TSF with N5P, the refractive indices of the NLC and the polymer matrix are initially matched at $T = T_{NI}$ (*i.e.*, $n_i \sim n_p$ at $T = T_{NI}$). One might think that such the small distinction of the refractive indices between the NLC and the polymer matrix can lead to the constant transmittance at $T > T_{tr}$. However, the TSF with P5P, which has a large distinction between n_i and n_p , validates that the NLC droplets and the polymer matrix exist as the single phase at $T > T_{tr}$. Figs. 3.24a and 3.24b shows the temperature profiles and the transmittance change of the TSF with P5P during heating at $P_{eff} = 0.258 \text{ W}$ and cooling, respectively. In particular, the maximum transmittance in Fig. 3.24b is similar with that in Fig.

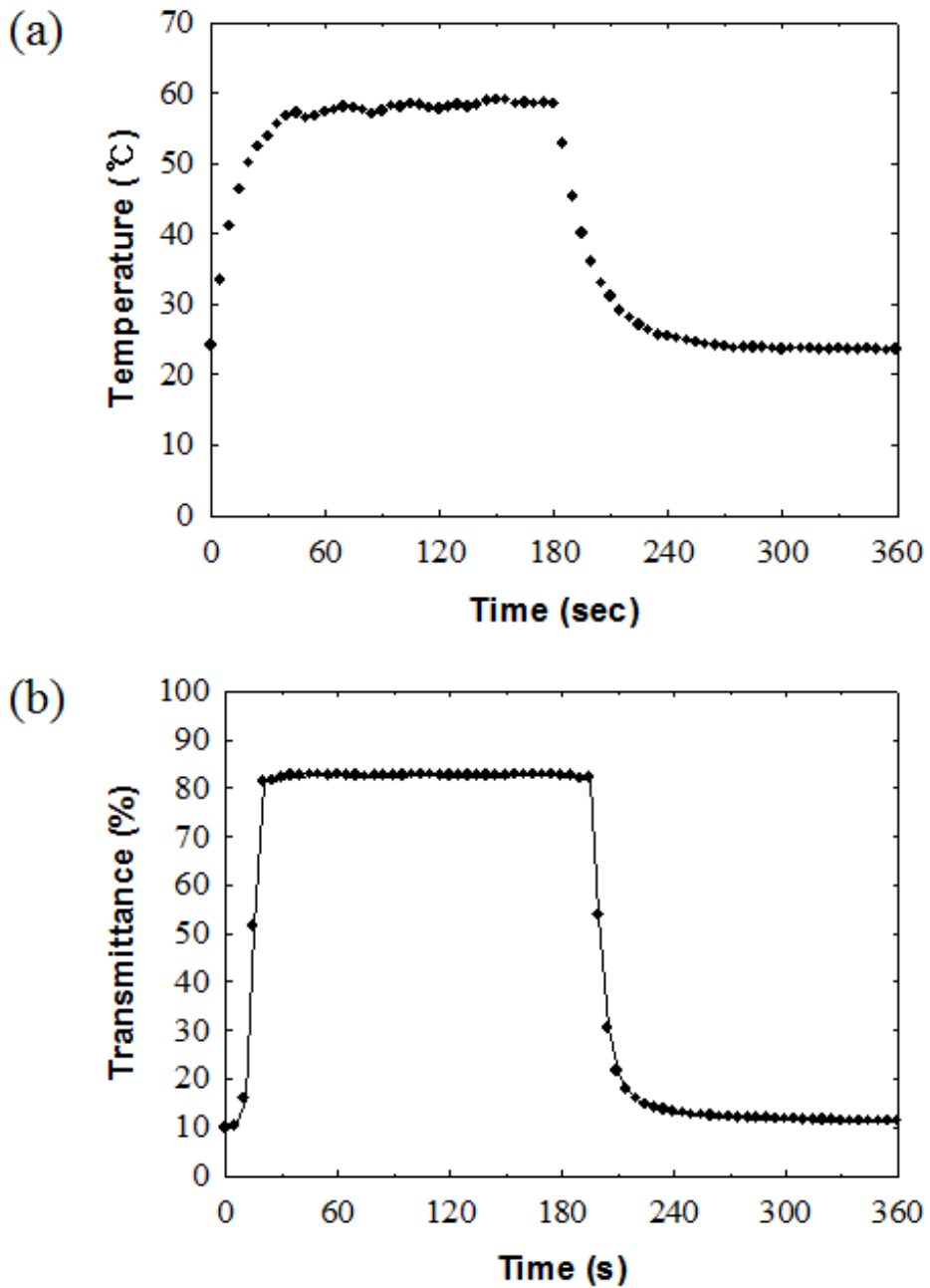


Figure 3.24 (a) Time dependent temperature profile, and (b) transmittance evolution of the TSF with P5P during heating at $P_{eff} = 0.258$ W and cooling.

3.20a, and exhibits a constant value despite a large contrast of n_i and n_p at $T > T_{tr}$.

3.4.4. Dynamic power control

An effective method is proposed to operate the TSF. The high P_{eff} leads to a decrease of Δt_h but an increase of Δt_c . However, both Δt_h and Δt_c can be reduced if P_{eff} is dynamically applied at each time. Fig. 3.25a shows the results when the effective electrical power varied during the heating, maintaining, and cooling regimes for the TSF with N5P. The high P_{eff} of 0.387 W was applied for 30 s, and the low P_{eff} of 0.139 W was maintained for 150 s to reduce Δt_c by maintaining a slightly higher temperature than T_{tr} . Thus, faster response of the transmittance was achieved as shown in Fig. 3.25b. Fig. 3.26 shows the comparison of appearance under the constant power control ($P_{eff} = 0.258$ W) and the dynamic power control ($P_{eff} = 0.387 \rightarrow 0.139$ W) for the TSF with N5P. Most of the surface of the TSF under the dynamic power control turns to be clear within 30 s but, the TSF operated at $P_{eff} = 0.258$ W is partially clear at 30 s.

P_{eff} , Δt_h , Δt_c and the effective consumed energy (E_{eff}) according to their operating methods are calculated and listed in Table 3.4 where E_{eff} is equal to the product of the effective electrical power (P_{eff}) and the applied time. Through the dynamic power control, we are able to reduce not only Δt_h by 77% (from 30 to 7 s) but also E_{eff} by 30% (from 12.9 to 9.0 mW h) compared with the constant power control at $P_{eff} = 0.258$ W.

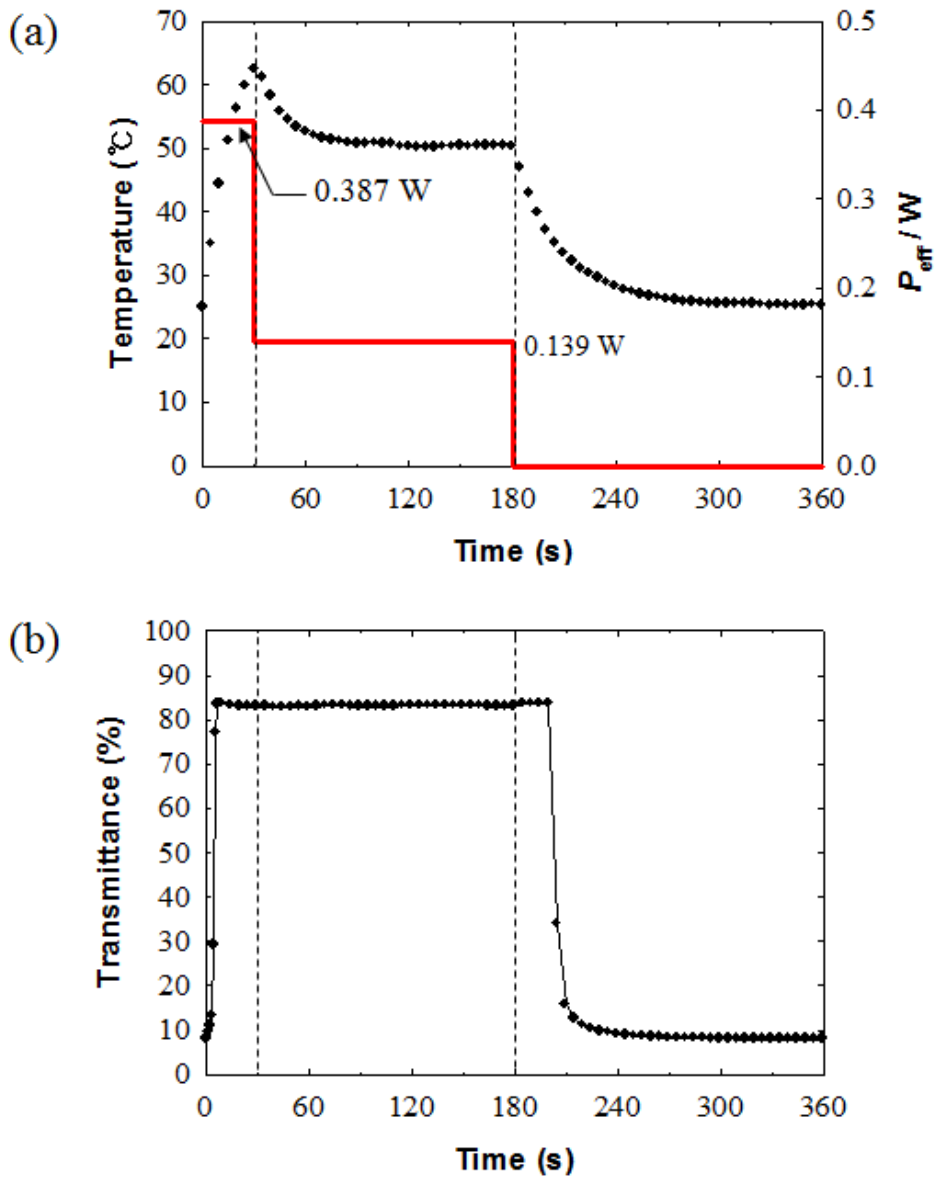


Figure 3.25 (a) Temperature profiles (black dots) of the TSF with N5P driven by the dynamic power control. The red line refers to the effective electrical powers. (b) Result of transmittance measurement in the dynamic power control test. The dashed lines correspond to the turning points of the applied effective electrical powers shown in (a).

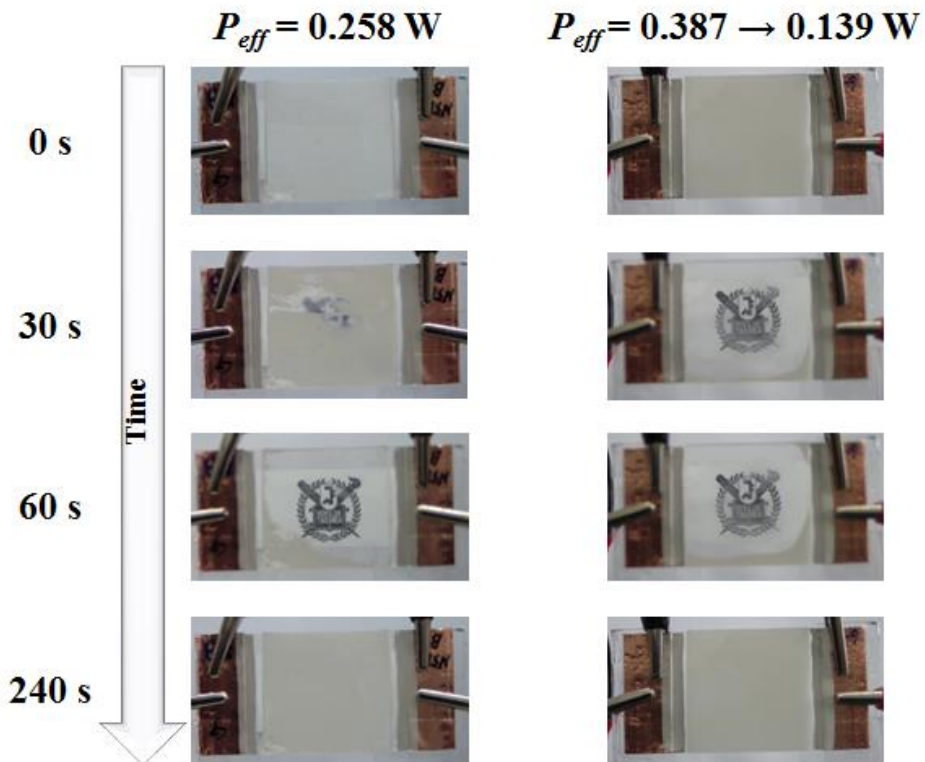


Figure 3.26 Comparison of appearance of the TSF with N5P under the constant power control ($P_{eff} = 0.258 \text{ W}$) and the dynamic power control ($P_{eff} = 0.387 \rightarrow 0.139 \text{ W}$).

Table 3.4 Comparison of P_{eff} , Δt_h , Δt_c , and effective consumed energies (E_{eff}) of the TSF with N5P according to the operating method.

P_{eff} / W	$\Delta t_h / \text{s}$	$\Delta t_c / \text{s}$	$E_{eff} / \text{mW h}$
0.258	30	20	12.9
0.323	25	25	16.2
0.387	20	25	19.4
0.387 \rightarrow 0.139 (Dynamic power control)	7	20	9.0

3.5. Summary

The novel TSF was demonstrated by employing PDLCs which were fabricated on the AgNW coated film via the simple solution coating method. The thermo-optical behavior of the TSF was described successfully through numerical analyses. We also proposed the effective operation method of the TSF to reduce the response time and the consumed energy by adopting the dynamic power control that provides a guideline for practical applications of the TSFs. While we suggested a system based on electric heating, the TSF can be applied without the heater in a circumstance using the environmental temperature. Furthermore, the operation temperature can be tuned because the transition temperature is adjusted by changing the concentration of LCs in PDLCs. It is anticipated that the TSF can be applied in smart windows for solar cells and automobiles, and solve drawbacks of conventional PDLC films such as a high cost for the fabrication of the electrodes and a high driving voltage.

3.6. References

- [1] V. Vorflusev, S. Kumar, *Science*, 1999, 283, 1903-1905.
- [2] R. Baetens, B. P. Jelle, A. Gustavsen, *Sol. Energy Mater. Sol. Cells*, 2010, 94, 87-105.
- [3] S. J. Woltman, G. D. Jay, G. P. Crawford, *Nat. Mater.*, 2007, 6, 929-938.
- [4] J. Qi, L. Li, M. De Sarkar, G. P. Crawford, *J. Appl. Phys.*, 2004, 96, 2443-2450.
- [5] P. Mach, S. Rodriguez, R. Nortrup, P. Wiltzius, J. A. Rogers, *Appl. Phys. Lett.*, 2001, 78, 3592-3594.
- [6] P. Mormile, L. Petti, M. Abbate, P. Musto, G. Ragosta, P. Villano, *Opt. Commun.*, 1998, 147, 269-273.
- [7] C. Hoppe, M. Galante, P. Oyanguren, R. Williams, *Mater. Sci. Eng. C*, 2004, 24, 591-594.
- [8] C. Hoppe, M. Galante, P. Oyanguren, R. Williams, *Macromolecules*, 2004, 37, 5352-5357.
- [9] N. Kumano, T. Seki, M. Ishii, H. Nakamura, T. Umemura, Y. Takeoka, *Adv. Mater.*, 2011, 23, 884-888.
- [10] S. Bronnikov, S. Kostromin, V. Zuev, *J. Macromol. Sci. B*, 2013, 52, 1718-1735.
- [11] L. G. Chen, *Doctoral thesis*, RMIT University, March, 2007.
- [12] X. Y. Zeng, Q. K. Zhang, R. M. Yu, C. Z. Lu, *Adv. Mater.*, 2010, 22, 4484-4488.
- [13] F. Xu, Y. Zhu, *Adv. Mater.*, 2012, 24, 5117-5122.
- [14] D. Langley, G. Giusti, C. Mayousse, C. Celle, D. Bellet, J.-P. Simonato, *Nanotechnology*, 2013, 24, 452001.
- [15] C. J. Emmott, A. Urbina, J. Nelson, *Sol. Energy Mater. Sol. Cells*, 2012, 97, 14-21.
- [16] H. H. Khaligh, K. Liew, Y. Han, N. M. Abukhdeir, I. A. Goldthorpe, *Sol. Energy Mater. Sol. Cells*, 2015, 132, 337-341.
- [17] J. Kelly, P. Palffy-Muhoray, *Mol. Cryst. Liq. Cryst.*, 1994, 243, 11-29.
- [18] J. He, B. Yan, B. Yu, S. Wang, Y. Zeng, Y. Wang, *Eur. Polym. J.*, 2007, 43, 2745-2749.
- [19] F. Bloisi, C. Ruocchio, P. Terrecuso, L. Vicari, *Phys. Rev. E*, 1996, 54, 5242-

5248.

- [20] T. Kim, Y. W. Kim, H. S. Lee, H. Kim, W. S. Yang, K. S. Suh, *Adv. Funct. Mater.*, 2013, 23, 1250-1255.
- [21] S. He, W. Liang, K.-L. Cheng, J. Fang, S.-T. Wu, *Soft matter*, 2014, 10, 4609-4614.
- [22] J. Li, S. Gauza, S.-T. Wu, *J. Appl. Phys.*, 2004, 96, 19-24.
- [23] J. Li, G. Baird, Y. H. Lin, H. Ren, S. T. Wu, *J. Soc. Inf. Display*, 2005, 13, 1017-1026.
- [24] H. Hori, O. Urakawa, K. Adachi, *Polym. J.*, 2003, 35, 721-727.
- [25] A. H. Sahraoui, S. Delenclos, S. Longuemart, D. Dadarlat, *J. Appl. Phys.*, 2011, 110, 033510.
- [26] S. Zumer, *Phys. Rev. A*, 1988, 37, 4006-4015.
- [27] S. L. Jacques, S. A. Prah, *Definition of effective cross-section*, omlc.org/classroom/ece532/class3/musdefinition.html, accessed: September, 2015.
- [28] I. Haller, *Prog. Solid State Chem.*, 1975, 10, 103-118.
- [29] S. Urban, A. Würflinger, B. Gestblom, *PCCP*, 1999, 1, 2787-2791.
- [30] X. He, R. He, X. Chen, Z. Zhao, S. Feng, N. Chen, M. Zhang, *J. Mater. Chem. C*, 2014, 2, 9737-9745.
- [31] N. Ji, W. Ruan, C. Wang, Z. Lu, B. Zhao, *Langmuir*, 2009, 25, 11869-11873.
- [32] G. P. Montgomery Jr, N. A. Vaz, *Phys. Rev. A*, 1989, 40, 6580-6592.
- [33] R. Bhargava, S. -Q. Wang, J. L. Koenig, *Macromolecules*, 1999, 32, 2748-2760.
- [34] D. Nwabunma, T. Kyu, *Macromolecules*, 1999, 32, 664-674.

IV. Concluding Remarks

This study was aimed to present a new microlens system and overcome problems of the conventional PDLC film based on comprehensive understanding for unique features of NLCs such as the phase transition over T_{tr} and the flow- and field-induced orientation in a microchannel. These goals were accomplished by demonstrating the tunable birefringent L^2 lens in a microchannel and the TSF and investigating their characteristics through various experiments and numerical analyses.

The tunable birefringent L^2 lens system was demonstrated using unique hydrodynamic behaviors of the NLCs. When the NLC as the main stream and the isotropic fluid as the sub-stream flowed in a microchannel, the plano-convex lens shape was formed in the expansion chamber. At this time, it was necessary that the directors had to be oriented uniformly to be act as the birefringent lens. Thereby, the strong electric field was applied perpendicular to the flow direction. To determine the appropriate experimental conditions such as the electrical and the hydrodynamic conditions, we introduced the new dimensionless number (Ev) defined as ratio of the electric field force and the viscous shear force. Also, it was found that the directors could be oriented parallel to the direction of electric field at $Ev > 500$ through the numerical analyses using Ericksen-Leslie (E-L) dynamic equations based on the continuum theory. Under such conditions that the electric field force overwhelms the viscos shear force, the optofluidic chip was operated as the birefringent L^2 lens. At the s-mode, a large distinct of the refractive indices between the main stream and the sub-stream induced a short focal length while a long focal length was formed at the p-mode due to a small difference of the refractive indices. In addition, the focal length was controlled by controlling the flow rates for the main stream because the L^2 interface was adjusted according to the ratio of the flow rates between the main stream and the sub-stream. Therefore, the optofluidic chip in this study provided two different ways to control the focal length, *i.e.*, by changing the curvature of L^2 interface and the polarized direction of incident light. To simulate the L^2 interfaces, the simplified E-L equations were derived. Under the strong electric field, the directors were aligned uniformly, so that we could neglect the angular momentum equation in the E-L equations. The

volume of fluid (VOF) method enabled us to combine the simplified E-L equations for the main stream with Navier-Stokes equation for the sub-stream. Using this scheme, we predicted exact L^2 interfaces and calculated the focal lengths via the simple ray-tracing. The optofluidic birefringent L^2 lens in this study has several merits. For examples, it provides a low light-scattering device due to using intrinsically smooth liquid-liquid interface. In addition, there are two different ways to control a focal length of the birefringent L^2 lens by changing the polarized direction of incident light as well as the flow rate. Furthermore, this device enables quick defocusing by converting the incident light from the s-mode to the p-mode. Therefore, it is anticipated that the optofluidic chip demonstrated in this study could be applied in other optofluidic applications such as an optical tweezer, a microlens array, etc.

In the study of the TSF, the film heater was fabricated by the simple wet-coating of the AgNW solution on the PET film. To evaluate the performance of the film heater, we introduced the effective electrical power representing the electric power consumed by AgNWs only. The AgNW coated film generated sufficient thermal energy to raise temperature of the TSF over T_{tr} , and this result was supported by the heat transfer simulation. The uncured PDLC solution, which was a mixture of 5PCH as the NLC phase and NOA65 as the polymer matrix, was coated on the prepared AgNW coated film, and cured by UV light. At this time, the PDLC layer was formed by polymerization induced phase separation (PIPS), which could be described from the Flory-Huggins (F-H) lattice model. Using this model, the phase diagram was depicted by considering the free energy for each phase. From the phase diagram for the PDLC, T_{tr} varied according to the concentration of NLC. This was also confirmed by not only the results of transmittance profiles with respect to temperature but also the DSC thermogram. Also, we found that the difference of the refractive indices between the NLC and the polymer over T_{tr} did not affect the transmittance at the clear state. This was validated from the phase diagram over T_{tr} where the NLC and the polymer phases coexisted as a single isotropic phase, and the experimental results of the TSF with P5P. In a bid to estimate the thermo-optical behaviors of the TSF, we carried out the heat transfer simulation of the TSF, and modified the variables depending on voltage into the variables as functions of temperature in the sample scattering cross-section (σ_s) in

the ADA. As a result, temperature dependent transmittances could be successfully described. When the TSF was compared with the conventional PDLC film driven by an electric field, it had some drawbacks such as a slow response time and high power consumption at large size due to usage of Joule heating. To overcome such demerits, we proposed the dynamic power control. In the dynamic power control, a high power was applied for short time at early stage and then a low power was subjected to the TSF. This brought to a reduced response time and a decrease of the consumed power. We expect that the TSF could be applied in smart windows for solar cells and automobiles using an environmental temperature as well as Joule heating.

We hope that the distinctive features of the NLCs noted here and the powerful simulation platforms for understanding them will help finding new attractive applications of the NLCs besides the TSF and the tunable birefringent L^2 lens system.

Korean Abstract

지금까지 액정의 응용은 주로 전계 내에서 배향 특성을 이용한 표시소자, 반응성 메조겐의 경화를 통한 광학 필름 등에 집중되어 왔다. 예를 들어 액정디스플레이 및 이를 위한 위상차 필름, 콜레스테릭 액정을 이용한 반사형 편광필름, 고분자 분산형 액정필름 등은 모두 위에서 언급한 액정의 고유 특성을 이용한 예라 할 수 있다. 본 연구는 전술한 전기광학적 특성과 더불어 열방성 (Thermotropic) 액정의 고유특성이라 할 수 있는 미세채널 내에서의 유동 특성과 전이온도에서의 상전이 특성에 대해 주목하였다.

2 장에서는 마이크로채널 내에서 등방성 유체와 네마틱 액정 간의 계면을 이용한 가변형 복굴절 렌즈 소자를 다룬다. 네마틱 액정에 전계가 인가되고 동시에 전계의 수직방향으로 네마틱 액정이 흐를 때 점성토크에 의한 유동배향과 전계배향의 경쟁에 의해 네마틱 액정분자의 배향이 결정된다. 본 연구에서는 네마틱 액정의 유동을 설명하기 위하여 에릭슨-레슬리 이론에 기반한 2 차원 유한요소법과 무차원 분석을 이용하여 흐름의 수직방향으로 액정이 배향될 수 있는 전압 및 유동조건을 제시하고, 이를 바탕으로 마이크로채널 내에서 네마틱 액정의 배향, 등방성 유체와 네마틱 액정간의 계면 및 복굴절 특성을 관찰한다. 이 때, 마이크로채널 내에서의 네마틱 액정의 흐름은 미세한 유속 조절을 위해 통상 이용되는 주사기 펌프 대신 질소 가스 압력으로 제어되며, 각 인가압력에서의 유속은 인입유량의 부피를 측정함으로써 확인할 수 있다. 강한 전계에 의하여 네마틱 액정의 배향이 균일한 흐름에서는 간소화된 에릭슨-레슬리 식이 유도될 수 있고 이 식은 VOF (Volume of fluid) 방법을 통해 등방성 유체의 모사를 위한 나비에-스톡스 식과 결합할 수 있다. 이를 통해 등방성 유체와 네마틱 액정 간에 형성된 렌즈 계면을 수치적으로 모사할 수 있으며 이를 바탕으로

광선추적을 통해 계산된 초점거리는 실험결과와 유사한 경향을 보임을 확인할 수 있다.

3 장에서는 열감응형 고분자 분산형 액정필름의 연구에 대해 기술된다. 기존의 고분자 분산형 액정필름은 고분자 매트릭스 상에 액정이 균일하게 분산된 필름을 두 개의 투명전극 사이에 배치하여 전계인가 시 전계 방향으로 액정분자가 배열되어 액정의 유효 굴절율이 고분자상의 굴절율과 일치하여 투명하게 된다. 반대로 전계 비인가 시에는 액정분자의 무질서한 배향으로 빛이 산란하게 되어 불투명한 특성을 보인다. 이 경우 전계 내에서의 액정 배향 특성을 활용하므로 필연적으로 두 개의 투명전극이 필요하며 낮은 구동전압을 위해서는 필름의 두께가 얇아야 되는 제한이 따른다. 또한 투명전극의 경우 높은 전기전도를 위해 주로 ITO (Indium-tin oxide)가 코팅된 유리가 사용되는데 이의 제작을 위해서는 증착 공정을 이용하여야 하므로 대면적 제작 시 비용측면에서 불리하다. 본 연구에서는 이를 극복하기 위해 전계를 이용한 방법이 아닌 열에너지를 이용하여 액정의 상전이를 통해 투과율을 조정하는 새로운 고분자 분산형 액정필름을 제시한다. 열에너지는 필름 모재 위에 은 나노 와이어를 코팅하여 줄 히팅(Joule heating)을 통해 제공되며, 자외선 경화형 수지에 분산된 액정 용액을 다시 한번 코팅함으로써 열감응형 고분자 분산형 액정필름을 제조한다. 이렇게 제조된 필름의 열 및 광학적 특성과 액정의 상전이 특성 분석을 통해 열감응형 고분자 분산형 액정필름의 구동 원리를 규명한다. 이를 토대로 열 수치해석 및 산란모델(Anomalous diffraction approach) 적용을 통해 투과율을 계산함으로써 그 거동을 예측할 수 있다. 아울러 낮은 소비전력과 반응속도 단축을 위해 동적 전력 제어 (Dynamic power control) 방법을 제시한다.

주요어: 고분자 분산형 액정필름, 상전이, 투과율, 변칙회절 산란모델, 줄
히팅, 실버 나노와이어, 네마틱 액정, 옅토플루이딕스, 가변형 복굴절
렌즈, 액체 렌즈, 에릭슨-레슬리 이론

학번: 2012-30164